

High efficiency top-emitting organic light-emitting diodes: Design and fabrication

Dissertation

Zur Erlangung des akademischen Grades

Doctor rerum naturalium
(Dr. rer. nat.)

vorgelegt

der Fakultät Mathematik und Naturwissenschaften

der Technischen Universität Dresden

von

M.Sc. Qiang Huang

geboren am 17.09.1973 in Shannxi, V. R. China

May 2007

Gutachter: Prof. Dr. Karl Leo
Gutachter: Prof. Dr. Thorvald Andersson
Gutachter: Dr. Gunther Haas

Eingereicht am: 05. 2007

Tag der Verteidigung: 24.09.2007

Publications

Articles

1. Qiang Huang, Sebastian Reineke, Karsten Walzer, Martin Pfeiffer, and Karl Leo, “Quantum efficiency enhancement in top-emitting organic light-emitting diodes as result of enhanced intrinsic quantum yield”, *Appl. Phys. Lett.* **89**, 263512 (2006).
2. Qiang Huang, Karsten Walzer, Martin Pfeiffer, Karl Leo, Michael Hofmann, and Thomas Stübinger, “Performance improvement of top-emitting organic light-emitting diodes by an organic capping layer: an experimental study”, *J. Appl. Phys.* **100**, 064507 (2006).
3. Qiang Huang, Karsten Walzer, Martin Pfeiffer, Vadim Lyssenko, Gufeng He, and Karl Leo, “Highly efficient top emitting organic light-emitting diodes with organic outcoupling enhancement layers”, *Appl. Phys. Lett.* **88**, 113515 (2006).
4. Duncan Hill, Karl Leo, Gufeng He, and Qiang Huang, “Analysis of spatial coherence of organic light-emitting devices through investigation of interference effects observed in top-emitting devices”, *Appl. Phys. Lett.* **90**, 101111 (2007).
5. Kristiaan Neyts, Matthias Marescaux, Angel Ullan Nieto, Andreas Elschner, Wilfried Loevenich, Karsten Fehse, Qiang Huang, Karsten Walzer, and Karl Leo, “Inhomogeneous luminance in organic light emitting diodes related to electrode resistivity”, *J. Appl. Phys.* **100**, 114513 (2006).

Conference papers

1. Qiang Huang, Karsten Walzer, Martin Pfeiffer, Gufeng He, Karl Leo, Michael Hofmann, Thomas Stübinger, and Martin Vehse, “High efficiency and low voltage p-i-n top emitting organic light-emitting devices”, *Proceedings of the international Society for Optical Engineering (SPIE)*, **5937**, 159 (2005).
2. Yuto Tomita, Christian May, Michael Torker, Jorg Amelung, Karl Leo, Karsten Walzer, Karsten Fehse, and Qiang Huang, “High efficient p-i-n type OLED on ZnO:Al (ZAO)”, *Proceedings of Organic Electronic Conference 2006*, P020410 (2006).
3. J. Birnstock, M. Hofmann, S. Murano, M. Vehse, J. Blochwitz-Nimoth, Q. Huang, G. F. He, M. Pfeiffer, and Karl Leo, “Late-News Paper: Novel OLEDs for Full Color Displays with Highest Power Efficiencies and Long Lifetime”, 2005 Society for Information Display (SID) International Symposium, *Digest of Technical*

Papers **36**, p. 40 (Boston, MA, USA, 2005).

Patents

1. Karsten Walzer, Roch Teja, Qiang Huang, and Karl Leo
Organische Leuchtdiode und Anordnung mit mehreren organischen Leuchtdioden
(pending).

Contents

1	Introduction and motivation	1
2	Physics of organic semiconductors and organic light-emitting diodes	5
2.1	Basic physics of organic semiconductors.....	5
2.1.1	Energy levels in organic materials.....	5
2.1.2	HOMO and LUMO in organic semiconductors.....	6
2.1.3	Excited states in organic molecules.....	8
2.1.4	Electronic transitions in organic semiconductors.....	9
2.1.4.1	Radiative transitions.....	10
2.1.4.2	Non-radiative transitions.....	10
2.1.5	Excitons.....	11
2.1.6	Transport properties of excited states.....	12
2.1.6.1	Charge carriers in organic solids.....	12
2.1.6.2	Charge carrier transport in amorphous organic thin films.....	12
2.2	Device physics of organic light-emitting diodes.....	14
2.2.1	Device structure.....	14
2.2.2	Electrical processes in the device.....	16
2.2.2.1	Charge carrier injection.....	16
2.2.2.2	Charge carrier transport in organic layers.....	18
2.2.2.3	Exciton formation.....	19
2.2.2.4	Exciton diffusion (energy transfer) and decay.....	20
	I Exciton formation in dye doped emissive layers.....	21
	II Exciton recombination (decay).....	22
2.2.3	Optical processes in OLEDs.....	22
2.2.3.1	Light generation and reabsorption.....	22
2.2.3.2	Light outcoupling.....	22
	I Light outcoupling in conventional bottom-emitting OLEDs.....	23
	II Exciton recombination (decay).....	24
2.3	High efficiency top-emitting OLEDs.....	25
2.3.1	Definition of efficiency.....	25
2.3.1.1	External quantum efficiency.....	25
2.3.1.2	Power and current efficiency.....	26
2.3.2	Basics of a microcavity.....	26
2.3.3	Factors determining the external quantum efficiency of an OLED.....	27
2.3.4	Ways to improve performance of top-emitting OLEDs.....	28
2.3.5	Doping basics.....	29
3	Materials and experiments	32
3.1	Materials and their properties.....	32
3.1.1	Hole conduction materials for hole transport and electron blocking.....	32
3.1.2	Electron conduction materials for electron transport and hole blocking.....	34

3.1.3	Host materials for emissive dopants.....	35
3.1.4	Emitters and emissive dopants.....	37
3.1.5	Electrical dopants.....	40
3.1.6	Purification of organic materials.....	41
3.2	OLED preparation and measurements.....	41
3.3	Experimental methods.....	42
3.3.1	Impedance spectroscopy.....	42
3.3.2	Photoelectron spectroscopy (UPS/XPS).....	46
3.3.3	Efficiency measurements in integrating sphere.....	47
4	Top-emitting OLEDs with non-inverted structure	49
4.1	Introduction.....	49
4.2	Optimization of the device structure.....	50
4.2.1	Influence of electrode materials on the electrical device properties.....	50
4.2.1.1	Different anodes.....	51
4.2.1.2	Different cathodes.....	52
4.2.2	Influence of organic layer thickness on the electrical device properties.....	53
4.2.3	Influence of the reflectivity of the bottom contact on the device efficiency...	54
4.2.4	Influence of organic layer thickness on the device efficiency.....	55
4.3	Highly efficient top-emitting OLEDs.....	57
4.3.1	High efficiency top-emitting OLEDs employing Ag as both bottom and top electrodes.....	57
4.3.2	Efficiency improvement by an organic capping layer.....	59
4.3.2.1	Influence of the capping layer thickness on the performance of top-emitting OLEDs in perpendicular direction.....	61
4.3.2.2	Influence of the capping layer on the overall performance of top-emitting OLEDs.....	64
4.3.3	Highly efficient red, green, and blue top-emitting OLEDs.....	67
4.4	Quantum efficiency enhancement as a result of enhanced intrinsic quantum yield...	69
4.4.1	Experiment.....	69
4.4.2	Results and discussion.....	70
4.5	Conclusions.....	77
5	Top-emitting OLEDs with inverted structure	78
5.1	Introduction.....	78
5.2	Challenges introduced by the inverted structure.....	79
5.2.1	Inverted and non-inverted top-emitting OLEDs.....	79
5.2.2	Inverted top-emitting OLEDs with different electrodes.....	81
5.2.3	Charge carrier injection.....	83
5.2.4	Surface conditions of contacts.....	83
5.3	Metal/organic interface study.....	84
5.3.1	Interfaces of metal on Bphen (ETL) and Bphen on metal.....	85
5.3.2	Interfaces of metal/HTL and HTL/metal.....	90

5.4	High efficiency inverted top-emitting OLEDs.....	95
5.4.1	Inverted devices with electron injection layers.....	95
5.4.2	High efficiency inverted top-emitting OLEDs.....	96
5.5	Conclusions.....	97
6	Stability study of top-emitting OLEDs	98
6.1	Introduction.....	98
6.2	Influence of electrode materials on device lifetime.....	99
6.2.1	Influence of anode materials.....	99
6.2.2	Influence of cathode materials.....	103
6.3	Influence of Ag top contact thickness on device stability.....	104
6.4	Ultra-stable red top-emitting OLEDs.....	105
6.5	Conclusions.....	107
7	Summary and outlook	109
7.1	Summary.....	109
7.2	Outlook.....	110
	Bibliography	112
	List of symbols	120
	List of abbreviations.	121
	List of compounds	122
	Acknowledgements	123

Chapter 1

Introduction and motivation

Investigations on electroluminescence from organic semiconductors with a conjugated π electron system can be traced back for more than forty years. However, only after the first demonstration of an efficient organic light-emitting diode (OLED) by Tang and Van Slyke in 1987, featuring a single heterojunction structure [1], organic electroluminescent devices are able to show their true potential for display and lighting applications. Since this breakthrough, investigations on organic light-emitting diodes (OLEDs) have been intensified and many high efficiency OLEDs have been demonstrated.

OLED technology shows great potential for flat panel displays (FPDs), flexible displays, and solid state lighting because of its technical merits such as being thin and light in weight, fast switching, wide viewing angle, low power consumption, etc. Up to now, OLED technology has already been used for small displays in several commercial products such as mobile phones, MP3 players, digital cameras, etc. Usually, for this kind of small and low resolution displays, passive matrix (PM) driving technology featuring a relatively simple addressing scheme is used. In this case, a conventional bottom-emitting OLED architecture is appropriate. However, to produce high-resolution and high-information content large-area displays, the active matrix (AM) driving mode has to be used, which implements a driving unit underneath each pixel and, hence, requires much more complicated addressing circuits than those of PM displays. Furthermore, to achieve stable and uniform luminance, an even more complicated addressing scheme is needed [2]. This inevitably reduces the aperture ratio (emission area) when a bottom-emitting OLED architecture is chosen (see Fig. 1.1) [3, 4]. As a consequence of this smaller aperture ratio, bottom-emitting OLEDs have to be driven at higher brightness to achieve the same level of brightness than displays having larger aperture ratio, leading to reduced

device lifetime and increased power consumption [5]. The problem of reduced aperture ratio can be overcome by using a top-emitting OLED architecture, as shown in Fig. 1.2. With light outcoupling from the top surface instead of from the back, all electronic devices on the backplane are buried under the diodes so that theoretically, they can emit over the entire pixel area, giving excellent fill factors and a large aperture ratio ($\sim 70\%$) [4], having advantages for high pixel resolution, high information-content active matrix displays [6]. In addition to the large aperture ratio, another advantage of top-emitting OLEDs is their easy integration with opaque substrates, such as silicon wafers and metallic foils, because light is emitted away from the substrate. Therefore, they can be integrated easily with the well-developed silicon thin film technology or be used to make cheap flexible displays or lighting units on metal foil. Because of their structural advantages, top-emitting OLEDs are currently under intensive investigation.

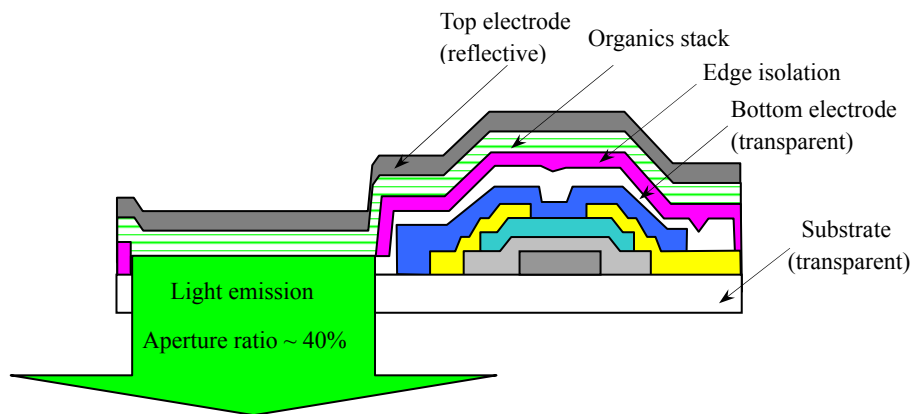


Fig. 1.1. Active-matrix layout with bottom-emitting OLED architecture.

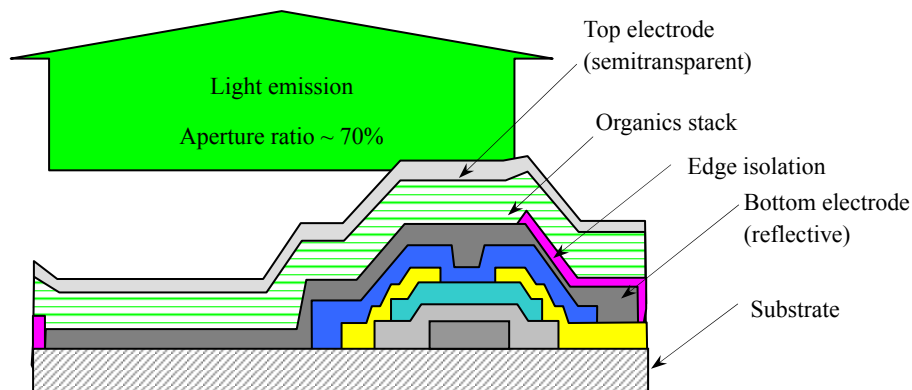


Fig. 1.2. Active-matrix layout with top-emitting OLED architecture.

Normally, top-emitting OLEDs show quite strong microcavity effects because of the reflective anode and the partially reflective cathode used, as well as the overall device thickness being in the order of the emission wavelength. In this case, not only wide-angle, but also multiple-beam interference exist within the device. Optical interference effects in this kind of device are rather strong and thus play a crucial role in the distribution pattern (i.e. dependence of intensity and color on viewing angles) of the emitted light. Consequently, the emission of a top-emitting device depends critically on the optical properties of the electrodes and the constituent organic materials, the thicknesses of the organic layers, the position of the emission zone, etc. As an optoelectronic device, the performance of the devices depends also on the electrical device properties, which are determined by the electrical properties of all constituent layers such as carrier mobility, the thickness of the organic layers and their interfaces, and the energetic situation at the metal/organic interfaces. Therefore, to achieve high efficiency top-emitting OLEDs, the optical and electrical device structures have to be optimized simultaneously. Moreover, for display and lighting applications, the lifetime of the devices is another critical issue, which depends not only on the stability of the constituent organic materials, but also on the situation at the metal/organic and organic/organic interfaces. All these factors make the design and optimization of top-emitting OLEDs complicated and difficult. Therefore, almost all top-emitting OLEDs reported up to now show worse performance than corresponding conventional bottom-emitting OLEDs. The lower device efficiency and shorter lifetime remain as the main obstacles to the practical use of top-emitting OLEDs, despite their structural advantages. To justify the advantages of top-emitting OLEDs over their bottom-emitting counterparts and fully realize the potential of top-emitting OLED technology, high performance top-emitting OLEDs need to be developed.

The research on top-emitting (transparent) OLEDs was initiated in 1996 by the Forrest group at Princeton University [7]. In their devices, sputtered indium tin oxide (ITO) was used as the top electrode. However, mainly due to sputtering damages of the underlying organic layers, all the devices showed much worse performance (external quantum efficiency around 0.1%) than corresponding bottom-emitting OLEDs [8]. Since then, most of the investigations on top-emitting OLEDs were focused on techniques to reduce the sputtering damage by introducing either a buffer layer [8-13] or optimizing the sputtering process [14-16]. As late as 2002, Lu et al. could show a top-emitting OLED with comparable performance to a control bottom-emitting device [17]. However, both devices had a low external quantum efficiency of around 6% at the current density of 10 mA/cm² [17], which was significantly lower than the highest efficiencies reported at that time (> 10%) [18].

Using a thermally evaporated thin metal film as the top contact, Hung et al. showed a top-emitting OLED with comparable electrical properties to corresponding bottom-emitting OLEDs, but still much lower efficiency [19]. Following this strategy, Riel and later other groups demonstrated high efficiency top-emitting OLEDs with much higher current efficiency in the perpendicular direction than corresponding bottom-emitting OLEDs [20]. However, the overall performance of the devices was still not comparable with their bottom-emitting counterparts [19, 20]. In this thesis, high performance red (external quantum efficiency of 15.3%), green (external quantum efficiency of 20.1%), and blue (external quantum efficiency of 5.0%) top-emitting OLEDs will be demonstrated, which show comparable or even better performance than the highest efficiencies reported for corresponding bottom-emitting OLEDs.

This thesis focuses mainly on the techniques to achieve high-performance top-emitting OLEDs, regarding device efficiency and lifetime for both non-inverted and inverted structures. It is thus organized as follows: In Chapter 2, the basic physics of organic semiconductor materials are reviewed, including the electronic properties of organic semiconductor materials, molecular excitations and their electronic transitions etc., which are believed to be critical for understanding of the work. Then, the general device physics of OLEDs are reviewed in detail, which includes almost every important electrical and optical process involved in the device. Finally, techniques and methods used to improve the device performance are summarized, which includes electrical doping of charge carrier transport layers. In Chapter 3, all organic materials, experimental techniques, and characterization methods used in this study are briefly described. In the following Chapter 4, techniques that are used for device optimization of non-inverted top-emitting OLEDs are discussed. Also, the mechanism of light outcoupling enhancement by a capping layer is discussed there. In the last part of Chapter 4, the influence of the optical device structure on the intrinsic quantum yield of the emitters is studied. Chapter 5 is focused on inverted top-emitting OLEDs, which are believed to be better applicable with current mainstream n-type amorphous silicon thin film transistor (TFT) technology [21-23]. In this Chapter, the organic/metal and metal/organic interfaces are investigated in detail and their influence on device performance is discussed. In Chapter 6, the degradation of top-emitting OLEDs is studied, with a focus on the influence of electrode material and electrode thickness on the lifetime of top-emitting devices.

Chapter 2

Physics of organic semiconductors and organic light-emitting diodes

In this Chapter, the basic physics of organic semiconductors and the device physics of organic light-emitting diodes will be reviewed. Being covalently bound solids, electronic properties of inorganic semiconductor materials can be understood based on a well-defined band structure with nearly free charge carriers. However, as a result of much weaker van der Waals bonding in molecular solids, the dynamics of charge carriers and molecular excitations in organic semiconductor materials are much different from their inorganic counterparts.

2.1 Basic physics of organic semiconductors

2.1.1 Energy levels in organic materials

Due to the weak van der Waals bonds in organic materials, the electronic structures and properties of these molecular solids are largely determined by the individual, isolated molecule. From a quantum mechanics point of view, the molecular wavefunctions Ψ^n and the corresponding energy levels E^n of a molecule are solutions of the non-relativistic Schrödinger equation:

$$H\Psi^n = E^n\Psi^n, \quad (2.1)$$

where H is the total Hamiltonian and n is a quantum number of an eigenstate. Based on the so called Born-Oppenheimer approximation where the motion of nuclei and electrons are solved separately, the total wavefunction Ψ_t and the total energy E_t of a molecule can be approximated by:

$$\Psi_t = \Psi_e \Psi_v \Psi_r, \quad (2.2)$$

$$E_t = E_e + E_v + E_r, \quad (2.3)$$

where Ψ_e , Ψ_v , and Ψ_r are the electronic, vibrational and rotational wavefunctions, respectively, while E_e , E_v , and E_r are the corresponding energies. However, if one wants to compute the electronic eigenstates of many-electron molecules, further approximations based on the molecular orbital theory are needed. A method called linear combination of atomic orbitals (LCAO) is frequently used, in which it is assumed that the electronic wavefunctions retain much of their atomic orbital characteristics when atoms combine to form a molecule [24].

For most organic molecules, the interesting optoelectronic properties can be understood mainly on the basis of the highest occupied molecular orbitals (HOMOs) and the lowest unoccupied molecular orbitals (LUMOs). In the simplest approximation, where internal interactions between electrons are neglected, the LUMO describes not only the lowest energetic position of an electron excited from one of the internal occupied energy levels, but also the lowest possible energetic position of an extra electron brought in from outside [25].

2.1.2 HOMO and LUMO in organic semiconductors

Organic semiconductor molecules are usually characterized by a conjugated π -bond network with alternating single (σ) and double/triple (σ and π^a , see Fig. 2.1a) bonds. The π bonds in the molecule interact with each other freely, leading to a delocalized π system with formation of new molecular orbitals. These molecular orbitals are called π orbitals which may extend over the whole molecule, as illustrated in Fig. 2.1b where the delocalized π system of a benzene molecule is shown. Normally, the highest occupied and lowest unoccupied molecular orbitals (HOMO and LUMO, respectively) in organic semiconductor molecules are π orbitals. Therefore, the HOMO corresponds to bonding π and LUMO to anti-bonding π^* orbitals which have higher energy. When forming films, these molecules overlap with their extended π orbitals because π orbitals feature large electron density on both faces of the carbon backbone. As a result of this π orbital overlapping of neighboring molecules, intermolecular electron exchange can happen within HOMO or LUMO. However, because of the slight overlap of π orbitals between molecules due to weak van der Waals bonds, this exchange is so weak that electrons are rather localized at individual

^a In a π bond, the electron density is concentrated above and below the bond axis. Depending on whether p orbitals are oriented in phase or out of phase, a bonding (π) or anti-bonding (π^*) bonds is created.

molecules and, unlike in the case of inorganic semiconductors, there are no really free electrons. Nevertheless, it still can be considered that the HOMO and LUMO levels are to organic semiconductors what valence and conduction bands are to inorganic semiconductors.

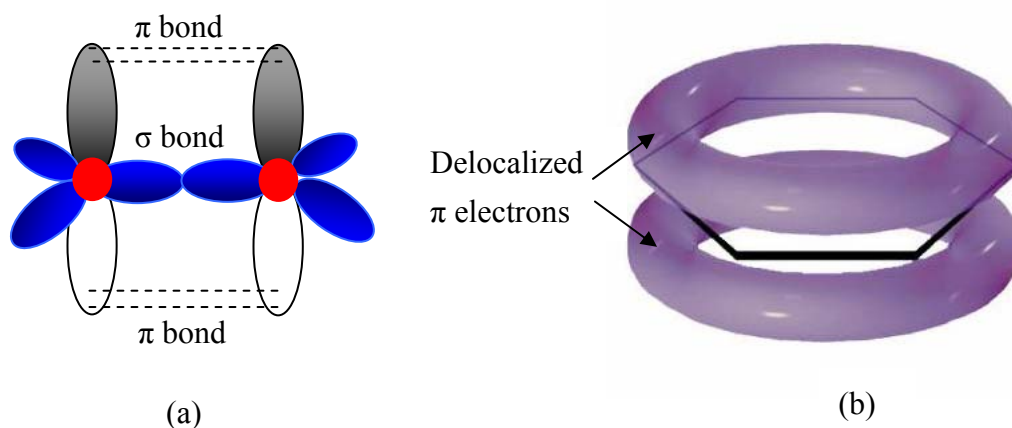


Fig. 2.1. Schemes of (a) a double bond of two sp_2 -hybridised carbon atoms, which consists of an σ and a π bond, and (b) a delocalized π system of a benzene molecule (reprinted from [26]).

Similar to the band splitting in an inorganic semiconductor, intermolecular interactions in molecular solids with conjugated π systems also lead to a splitting of the HOMO and LUMO and to the formation of narrow bands (energetic intervals). The energy difference between the HOMO and LUMO level, which is typically in the range of 1.5-3 eV [24], is regarded as band gap energy, corresponding approximately to the lowest energy required to generate an excited state. The band gap usually decreases with increasing delocalization as the π electron system becomes larger. For example, the HOMO-LUMO gap values of polycyclic compounds decrease with increasing number of benzene rings, as shown in Fig. 2.2, where gap values of benzene, naphthalene, anthracene, tetracene, and pentacene are demonstrated from experiment and calculation using Hückel theory [27].

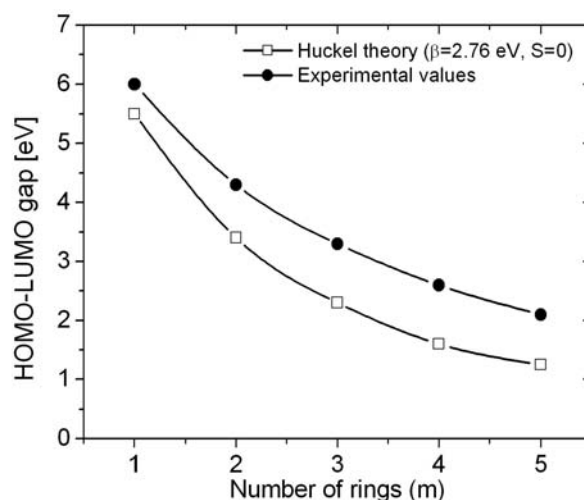


Fig. 2.2. HOMO-LUMO gap from experiment (solid circles) and calculated with Hückel theory (open squares) (reprinted from [27]) for organics from benzene to pentacene.

2.1.3 Excited states in organic molecules

As indicated in Eq. 2.2 and 2.3, the energy states of molecules correspond not only to electronic, but also to vibrational and rotational degrees of freedom. However, the energy transition processes are dominated by transitions between electronic states with magnitude in the order of eV. Therefore, typical energy levels/states and energy-transfer processes can be well described by a modified Jablonski diagram where only electronic levels are presented (see Fig. 2.3).

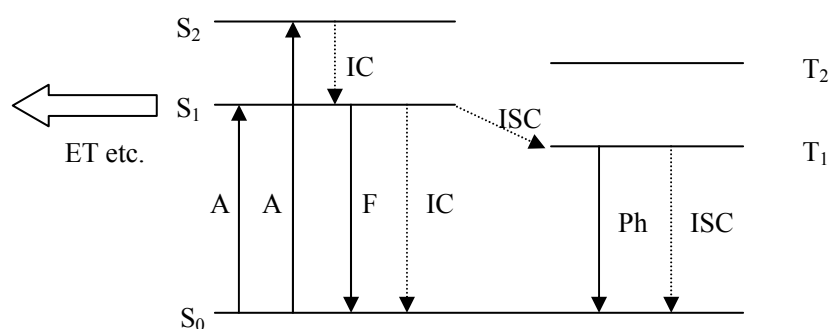


Fig. 2.3. Jablonski diagram of an organic molecule depicting typical energy transitions processes. Solid and dashed arrows represent radiative and non-radiative process, respectively. A-Absorption; F-Fluorescence; IC-Internal conversion; ISC-Intersystem crossing; Ph-Phosphorescence; ET-Energy transfer to other molecules.

By photoexcitation, an electron from the ground states could be promoted to an excited state resulting in two unpaired electrons with one electron in an unfilled orbital having higher energy (for example in the LUMO), while the other one remains in a partially filled ground state (for example in the HOMO) with each electron

having spin 1/2. According to quantum mechanics, the total spin S of these two unpaired electrons can only take the values of $S=0$ or $S=1$. The $S=0$ state, called singlet state (denoted by S), is spin antisymmetric under particle exchange with the spin state:

$$\sigma_- = \frac{1}{\sqrt{2}} \{ \uparrow(e_1) \downarrow(e_2) - \downarrow(e_1) \uparrow(e_2) \}. \quad (2.4)$$

In contrast, the $S=1$ state which is called triplet state (denoted by T), is spin symmetric under particle exchange having three possible spin states:

$$\sigma_+ = \frac{1}{\sqrt{2}} \{ \uparrow(e_1) \downarrow(e_2) + \downarrow(e_1) \uparrow(e_2) \}, \quad (2.5)$$

$$\sigma_+ = \uparrow(e_1) \uparrow(e_2), \quad (2.6)$$

$$\sigma_+ = \downarrow(e_1) \downarrow(e_2). \quad (2.7)$$

Here, the symbols of \uparrow and \downarrow represent the possible spin states of each electron. Two electrons are signified by e_1 and e_2 , respectively [28].

In a simplified case, the singlet and triplet states of two unpaired electrons can be schematically represented as shown in Fig. 2.4.

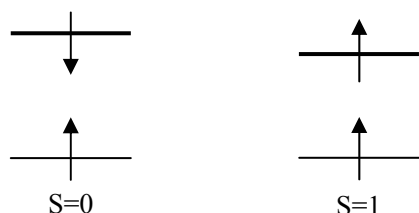


Fig.2.4. Simplified representations of singlet and triplet states.

Normally, the triplet state is at a lower energy than the corresponding singlet state because according to Pauli's exclusion principle, the average Coulomb repulsive force is larger in the singlet than in the triplet state as a result of closer average distance of electrons in the singlet state. The energy splitting between them is typically in the order of 0.1-1 eV.

2.1.4 Electronic transitions in organic semiconductors

As illustrated in Fig. 2.3, after an electron being promoted to an excited state as a result of energy absorption, the electron relaxes towards the ground state losing energy via both radiative and non-radiative processes. The extent of these decay pathways is determined by the relative magnitudes of their rate constants.

2.1.4.1 Radiative transitions

According to Pauli's exclusion principle, the ground state is a singlet state S_0 . This means that only singlet excited states (S_1 , S_2 etc.) can be created directly by photo-absorption because the total electron spins have to be conserved during the transitions. The recombination from S_1 to S_0 can occur by the radiative emission, known as fluorescence. As a spin allowed transition, fluorescence is a rapid radiative process with a typical rate constant of $\sim 10^6$ - 10^9 s⁻¹ [25]. Although theoretically spin forbidden, radiative decay from the triplet to the ground states is also possible due to singlet-triplet states mixing because of spin-orbit coupling induced by heavy elements. This radiative emission is called phosphorescence, which is much slower with a rate constant of $\sim 10^{-2}$ - 10^6 s⁻¹ [25].

2.1.4.2 Non-radiative transitions

The radiative transitions discussed above have to compete with non-radiative transitions during the energy transfer process. If a non-radiative transition occurs within the same spin multiplicity, it is called internal conversion (IC). As one of the major non-radiative transitions, internal conversion always occurs from higher lying excited states (for example S_{n+1} to S_1 , where $n \geq 1$) to lower ones, losing energy via vibrational relaxation on the same timescale as molecular vibrations (10^{-13} s), which is orders of magnitude faster than radiative decay. As a consequence, molecular luminescence always occurs from the lowest excited states (S_1 or T_1), which is known as the Kasha rule. Although it is much slower, the internal conversion can also occur during transitions from S_1 to the ground state (S_0). In this case, the internal conversion rate is approximately proportional to the number of possible non-radiative pathways and is therefore usually larger for larger molecules and aggregates of molecules. On the other hand, electron transfer between states of different multiplicities via spin-inversion is called intersystem crossing. As illustrated in Fig. 2.3, the process involves the conversion of singlet to triplet states or vice versa. By spin-orbit coupling induced by heavy elements, the intersystem crossing from S_1 to T_1 can be very efficient, resulting in highly efficient phosphorescent OLEDs with internal quantum efficiency close to 100% by harvesting both singlet and triplet excitons [29, 30].

An excited molecule can also transfer its energy non-radiatively to neighboring molecules via dipole-dipole interactions (Förster transfer), electron exchange (Dexter transfer) or emission-reabsorption processes (rarely occurring in OLEDs). The first two are the major mechanisms for achieving high efficiency OLEDs based on host-guest emission systems (details in Section 2.2.2).

2.1.5 Excitons

The singlet (triplet) excited states can further localize with the formation of singlet (triplet) excitons under Coulomb attraction. Thus, excitons appear as bound states of charge carrier pairs with opposite electric charge. In solid materials, according to their degree of delocalization, there are normally three kinds of excitons, which are called Frenkel, charge-transfer, and Mott-Wannier excitons [31].

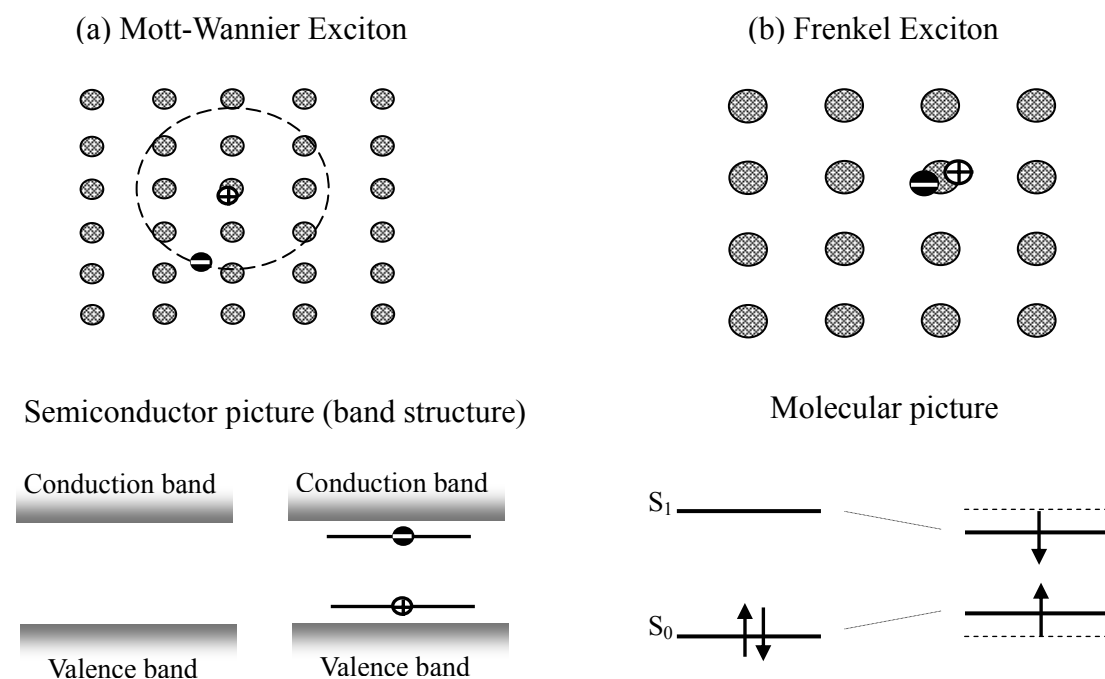


Fig. 2.5. Schematic of a (a) Mott-Wannier exciton with the corresponding semiconductor band diagram and (b) Frenkel exciton (singlet) showing the energy level diagram of discrete molecular states (reprinted from [26]).

As shown in Fig. 2.5, a Mott-Wannier exciton is a weakly correlated excited state with a large exciton radius (4~10 nm), which is usually found in inorganic semiconductors with well defined band structure. On the contrary, a Frenkel exciton is a strongly correlated electron-hole pair^b that is rather localized on a single molecule with its size corresponding to the molecular size (typically 0.5-1 nm) and a binding energy in the order of 0.3-1 eV. As a transitional excited state, a charge-transfer exciton is an intermediate between a Mott-Wannier and a Frenkel state, which may further localize to a Frenkel exciton.

In organic semiconductors, only Frenkel excitons and their precursors, the transitional charge-transfer (CT) excited states (excitons) can be found because of the strong Coulomb interaction between positive and negative polarons due to the small

^b Actually, charge carriers here are not electrons or holes but rather polarons.

dielectric constant of the material.

2.1.6 Transport properties of excited states

2.1.6.1 Charge carriers in organic solids

Due to the weak van der Waals interaction between molecules of organic semiconductors, the distance between molecules is so large that there is only a weak overlap of the molecular orbitals, resulting in a small intermolecular electron exchange. Charge carriers are rather localized at individual molecules. As a result of their local relaxation, charge carriers interact strongly with the electronic and nuclear subsystem of crystals, which may lead to the formation of electronic, molecular, and lattice polarons^c. The electronic polarization (electronic polaron), interaction of a localized charge carrier with valence π and σ electrons of its neighboring molecules, is a very fast process with a typical relaxation time between 10^{-16} - 10^{-15} s, which is much shorter than the typical moving time of charge carriers [31]. It is therefore the primary and dominant interaction of an excess charge carrier with surrounding molecular lattices, having a typical energy of 1.5 - 2.0 eV [31]. Consequently, the electronic polarization is the most important factor determining the charge carrier's self-energy and, correspondingly, the position of electronic conduction states in the energy diagram of organic semiconductors. The other two processes have similar time scales as those of charge transport in organic materials. The relaxations can thus be complete (adiabatic transport) or incomplete (non-adiabatic transport). In disordered organic materials, however, charge carrier transport is so slow that all three relaxation processes can be assumed to completely take place.

2.1.6.2 Charge carrier transport in amorphous organic thin films

All the relaxation processes discussed above stabilize the charge carriers energetically, and, thus, reduce the band gap. They either lead to hopping transport or band-like transport with a reduced bandwidth [32].

At very low temperature, charge carrier transport in some sufficiently pure and perfect organic crystals can be described by coherent band-like transport [33], leading to quite high mobility around $400 \text{ cm}^2/\text{Vs}$ or even higher [34]. However, for disordered organic molecular thin films, like most of the organic layers in OLEDs,

^c A Polaron is a quasiparticle comprising a charge carrier and the induced surrounding polarization. Based on different kinds of polarization process such as electronic, vibronic and phononic relaxation, the quasiparticles are divided into electronic, molecular, and lattice polarons, respectively.

there are no well-defined band structures due to the absence of extended delocalized states, which results in a relatively broad density of states (DOS) energy distribution for both neutral and charged excitations. The HOMO and LUMO energy levels of the molecules are thus rather widely distributed as a result of the structural disorder and in some case can be well approximated by a Gaussian-like distribution [35]. Charge carrier transport in such a system can then be described as stochastic hopping process between strongly localized states, resulting in low carrier mobilities. The hopping rate from one site to another depends on both their energy difference and the distance between them, being therefore strongly dependent on temperature and electric field [36, 37], which is frequently observed following a Poole-Frenkel like formula:

$$\mu(E, T) = \mu_0 \exp(\beta\sqrt{F}), \quad (2.8)$$

where μ_0 is the charge carrier mobility without field and β is the electric field activation parameter of the mobility, both of which are characteristic constants of the organic material. It is found that β is related to the degree of disorder in the material [38] and μ_0 primarily to the hopping distance, hopping frequency, and wave function decay constant of the carrier in the material [39]. Although many transport concepts developed for amorphous inorganic materials can be adapted to organic systems to some extent [40], the Gaussian shaped density of states (DOS) and the weak molecule interaction lead to some peculiarities in organic materials. Using a disorder-based model, Bässler and coworkers could achieve a quite good fit to the transport measurements of disordered organic materials [35]. For electrically doped organics, several other methods are used to describe hopping transport and determine conductivity or mobility, which includes the effective transport energy concept [40] and percolation theory [41, 42].

2.2 Device physics of organic light-emitting diodes

2.2.1 Device structure

Theoretically, an OLED has a structure that can be as simple as only one organic layer sandwiched in between two electrodes, an anode and a cathode, as shown in Fig. 2.6.

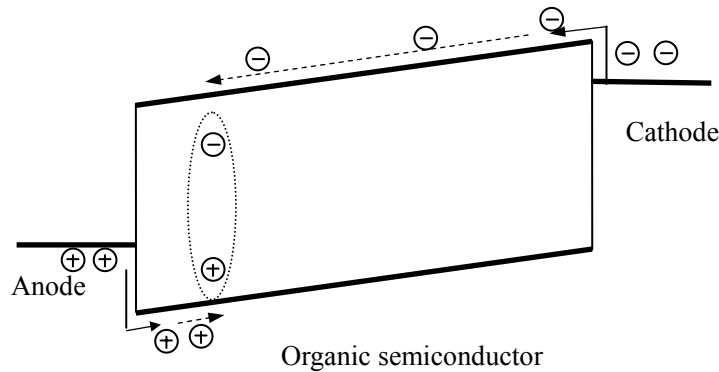


Fig. 2.6. Single-layer device under forward bias with the organic layer acting as charge carrier injection, transport, and emission layer.

To have light coupled out of the device, at least one of the electrodes is light transmissive. When an electric potential is applied between the electrodes so that the device is forward biased, i.e. the anode is at positive and cathode at negative bias, holes and electrons are injected into the organic layer from anode and cathode, respectively. After charge carrier injection, they are transported towards the opposite electrode under the internal electric field, until in an ideal case, they catch each other forming excitons, which then decay radiatively (and non-radiatively). In this case, the organic layer has to function not only as the emission layer (EML), but also the hole injection / hole transport layer (HIL/HTL) and electron injection/electron transport layer (EIL/ETL).

However, the single-layer structure is rarely used because of its extremely low efficiency: Usually, an organic semiconductor has different electron and hole mobility, so that the exciton formation occurs at positions very close to the electrodes where the excitons can be easily quenched. Furthermore, due to the different hole and electron injection efficiency into the organics, charge carriers are unbalanced in the organic layer, resulting in an excess of one carrier type which leads to not only a low efficiency and short device lifetime, but also to high leakage current, which reduces device stability. To get high performance OLEDs, a multilayer structure has to be used, as shown in Fig. 2.7. Every layer has to fulfill specific requirements so that individual steps involved in OLEDs can be optimized separately. Normally, from the hole

injection and transport side, the HIL is used with a suitable energetic level of the HOMO so that the energy barrier for hole injection is reduced, making hole injection from the anode into the HTL easier. The HTL should have a high hole mobility and appropriate HOMO and LUMO level so that it can also block electron injection in the opposite direction. EIL and ETL are normally used with similar requirements for the LUMO positions for electron injection, transport and hole blocking. For the EML, the primary criterion is its intrinsic efficiency: It should be as high as possible. In addition, the HOMO and LUMO positions of the EML have to make hole and electron injection from the neighboring layers possible. The desired light wavelength can be achieved by using different emitters either as bulk material or by co-evaporation with a matrix material. In phosphorescent devices, where the long lifetime of the triplet excitons normally leads to a large diffusion length of triplets, additional layers, so called hole and electron blocking layers (HBL and EBL) are widely used to confine excitons within the EML.

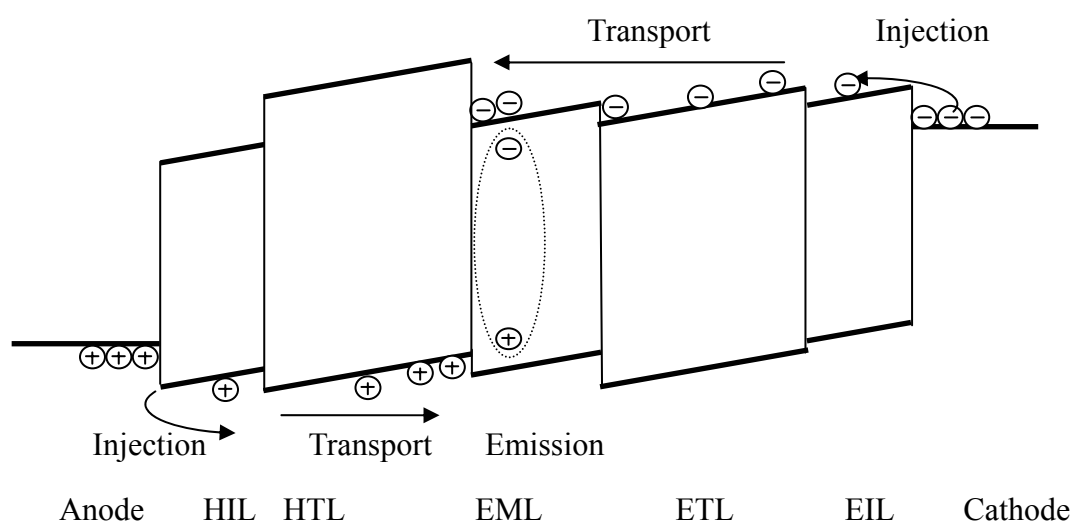


Fig. 2.7. Multi-layer OLED structure with ideal energy diagram under forward bias.

Although small molecule organics used in OLEDs usually rely on disordered materials without a well defined band structure, for simplicity, the HOMO and LUMO levels are still treated in a band-like fashion with the additional assumption that the vacuum level of every layer is aligned (see Fig. 2.7)^d.

^d It is well established that interface dipoles are usually formed at organic/metal interfaces, which makes the assumption invalid. However, the assumption is reasonable for organic/organic interfaces, since most of the organic/organic heterojunction have interface dipoles with energy < 0.1 eV [43].

2.2.2 Electrical processes in the device

Under forward bias, the electrical processes in a typical OLED can be roughly divided into four steps: (1) hole and electron injection from anode and cathode, respectively; (2) charge carrier transport towards the opposite electrode under internal electric field; (3) exciton formation due to the Coulomb interaction; (4) exciton diffusion and recombination (radiative and nonradiative decay). Among these steps, charge carrier injection and transport are of great importance in determining device efficiency [44] and lifetime [45].

2.2.2.1 Charge carrier injection

In an OLED, hole injection takes place from the Fermi level of the anode into the HOMO of the HIL (or HTL) and electron injection from the Fermi level of the cathode into the LUMO of the EIL (or ETL). Due to differences of their energy level, energy barriers for charge carrier injection exist and have to be overcome. For interfaces formed between inorganics or polymers with a metallic contact, the energy barriers can be predicted by the Schottky-Mott model with nearly perfect vacuum level alignment across the interfaces [46]. However, it is found that interface dipoles usually exist at the molecular organic/metal interfaces due to possible induced gap states [47], charge exchange [48], or molecular adsorption etc. [49], which makes the calculation of the barrier height difficult. Using a general model called induced density of interface states (IDIS), Kahn et al. tried to relate the barrier to the metal work function and to organic parameters [50]. They found that the density of gap states in the organic, which is induced by metallic states in close proximity to it, plays a key role in defining the position of the Fermi level. The occupation of these gap states determines the size and sign of the interface dipole [43].

To get maximum possible charge carrier injection, it is desirable to have Ohmic contacts so that the current flowing in the OLEDs is only limited by charge transport in organic layers. However, if energy barriers at the electrode/organic interfaces are high enough, an injection limitation will occur. For inorganic semiconductors, two models are mainly used to describe charge carrier injection: The Richardson-Schottky (RS) thermionic emission and the Fowler-Nordheim (FN) tunneling model [51]. In the RS model, tunneling is ignored and charge carriers from the contact can be injected once they have acquired sufficient thermal energy to overcome the maximum potential resulting from the superposition of the external and the image-charge potential. The temperature dependent current density is given by:

$$j_{RS} = A^* T^2 \exp\left(-\frac{\delta_B}{k_B T}\right) \exp\left(\frac{\beta_{RS} \sqrt{F}}{K_B T}\right). \quad (2.9)$$

Here, A^* is the Richardson constant ($A^*=120A/(cm^2K^2)$ if the effective mass of electrons inside the dielectric is equal to free electron mass), T the temperature in K , δ_B the zero field barrier height, and F the external electric field. In the FN model, charge carriers are injected into the semiconductor by tunneling. Ignoring the image charge effects and assuming tunneling through a triangular barrier, the FN model yields:

$$j_{FN} = \frac{q^3 F^2}{8\pi\hbar\delta_B} \exp\left(\frac{8\pi(2m^*)^{1/2} \delta_B^{2/3}}{3\hbar e F}\right). \quad (2.10)$$

Both mechanisms are only valid under certain conditions for carrier injection into semiconductors with extended band states and large mean free path. However, they are not suitable for carrier injection into organics, which are usually disordered systems with rather low average mean free path (in the order of the molecular distance). Nevertheless, both models can qualitatively describe carrier injection into organics to some extent. It is obvious from both models that the carrier injection depends on the barrier height (δ_B), which is the difference between the work function of the anode (cathode) and HOMO (LUMO) of organics, assuming that there is no interface reaction and dipole formation. This is confirmed by the experiments of various groups [52-54], which found that the injection efficiency (defined by the ratio of injection limited to the bulk limited current) scales with the difference in the appropriate energy levels of the metal and the organic. To describe the charge injection into organics well, a large backflow of injected carriers to contact due to the low mobility has to be taken into account. This means that the charge carrier injection may also depend on the carrier mobility in the organics [55]. There have been already several analytical studies and simulations on charge carrier injection into disordered hopping systems^e [56-58].

It is estimated that a barrier height around 0.3-0.4 eV is low enough to result in an Ohmic contact for an organic layer with a mobility in the order of $10^{-5} \text{ cm}^2 /(\text{Vs})$ [59]. However, in OLEDs, a barrier height in this range will not guarantee an Ohmic contact due to the fact of double-carrier injection, where charges of opposite sign are mutually able to compensate part of the space charges and recombine. Thus, it is more

^e Details are given in Section 2.1.6.2

complicated to simulate the carrier injection in OLEDs. Nevertheless, from the above discussion, it is possible to improve charge carrier injection by reducing barrier heights and increasing charge carrier mobilities of organics. This can be achieved by p- and n-type doping of charge carrier injection and transport layers, which we are going to discuss in detail in Section 2.2.5.

2.2.2.2 Charge carrier transport in organic layers

After injection from the electrodes into the organics, charge carriers are transported under an applied electric field towards the counter electrode. Since charge carriers are rather localized at the individual molecules, there exists a pronounced interaction between charge carriers and surrounding molecules, which leads to full relaxation of charge carriers. Thus, it is widely accepted that charge carriers exist as polarons rather than as free holes and electrons. Therefore, following carrier injection, electrons and holes enter negative (P^-) and positive polaron (P^+) states, respectively. In addition to the localization of charge carriers, small molecular organic films prepared by physical vapor deposition are usually amorphous without periodic order, so that charge carrier transport can not be defined as coherent motion in a well-defined band structure as it is in inorganic semiconductors. Carrier transport in organic layers is normally described by incoherent jumps between sites with different energy and distance due to the disorder in organics. Moreover, carriers can be intermittently trapped in local states induced by impurities or structural defects. All these factors lead to much lower charge carrier mobility as compared to inorganic semiconductors. For undoped organic layers in OLEDs, the hole mobility is typically between 10^{-7} and 10^{-3} cm^2/Vs , and the electron mobility is typically by a factor of 10-100 lower at room temperature.

As discussed before, charge carriers flowing in the device can also be limited by carrier transport in organic layers, which is the so-called space charge limited current (SCLC). In this case, electrodes have to be able to inject carriers faster than the organic bulk material can move them away, creating space charges. This in turn reduces the electric field at the injecting contact and thus impedes further charge carrier injection. For a single carrier device with a negligible intrinsic concentration of both carriers and traps, and with a mobility independent of the electric field, the SCLC is proportional to the mobility, square of the applied bias, and inverse to the organic layer thickness, following the Mott-Gurney equation [60]:

$$j_{SCLC} = \frac{9}{8} \epsilon \epsilon_0 \mu \frac{V^2}{d^3}. \quad (2.11)$$

In real single carrier devices, however, there exists a high density of trap states in the

organic layers. The Mott-Gurney equation is therefore only valid at high voltage where all traps are filled. At relatively low voltages, before all traps are filled, a trap charge limited current (TCLC) can be expected, with a power law dependence of current on voltage, following $J \sim V^{m+1}$, where the empirical parameter m indicates the distribution of trap states in the band gap [61]. This TCLC can also be found in some kinds of OLEDs, for example, in the Alq₃ based bilayer (only one heterojunction) device with one dominant kind of carrier, despite of double carrier injection. In this case, the device can be treated as a single carrier device and a large exponent power law dependence of $J \sim V^{8-9}$ is observed over a wide voltage range [62]. However, the situation becomes more complicated in state-of-the-art OLEDs, which have a multi-layer structure (several heterojunctions). Double carrier injection, exciton formation, diffusion, and recombination have to be taken into account. In addition, there exist energy offsets at these heterojunctions, which have to be overcome during charge transport.

2.2.2.3 Exciton formation

Following electron and hole injection into organic semiconductor thin films, free polarons are formed. When P^+ and P^- polarons encounter each other, they can be bound together by the Coulomb force, forming a neutral bound polaron pair, or charge transfer (CT) state. Once the CT states are formed, they continue to localize, forming triplet and singlet Frenkel excitons, as illustrated in Fig. 2.8.

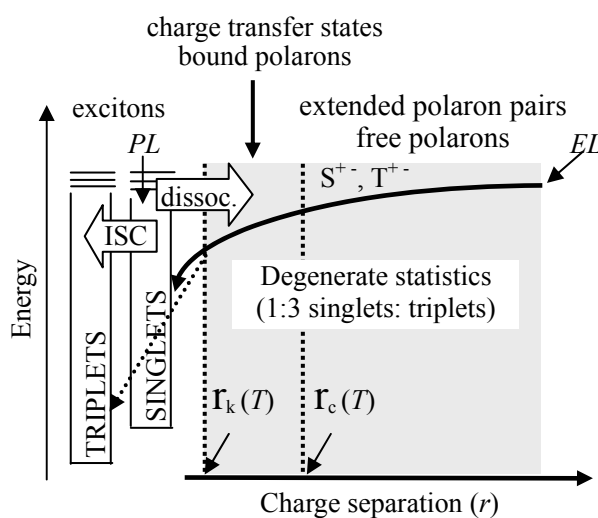


Fig. 2.8. Illustration of physics of spin formation (reprinted from [63]).

In an ideal situation where there is a random electrical injection, as in the case of light-emitting diodes and spin independent recombination, the numbers of singlet to triplet excitons formed approximately follow spin statistics (see Section 2.1.3) with the ratio of 1:3 [64]. For small-molecule devices, it is generally accepted that only

25% singlet excitons are formed during electrical excitation [30, 65]. This singlet exciton ratio (25%) is believed to limit the external quantum efficiency of fluorescent OLEDs to 5% assuming the outcoupling efficiency to be 20%. However, very recently, Shibata et al. questioned this singlet to triplet ratio by showing fluorescent OLEDs with an external quantum efficiency as high as 10% [66]. The ratio is also under controversy for polymer semiconductors. Although several results show that in some polymers, electrical excitation could generate singlet excitons far exceeding 25% [67-69], there are also arguments that the ratio is still around 25% and the observed relative high efficiency in fluorescence polymer LEDs, compared to their small molecule OLED counterparts, is mainly attributed to a high outcoupling efficiency of the devices due to preferentially in-plane aligned polymer chains [63].

2.2.2.4 Exciton diffusion (energy transfer) and decay

Excitons can diffuse in the solid after their formation and subsequently self-trapping by exciton-phonon coupling. As mobile molecular excited states without involving any net electric charge exchange, the exciton diffusion is actually an energy transport process between either the same or different type of organic molecules. The former process is called energy migration while the latter is called energy transfers. The bulk behavior of exciton diffusion can be described by the diffusion length:

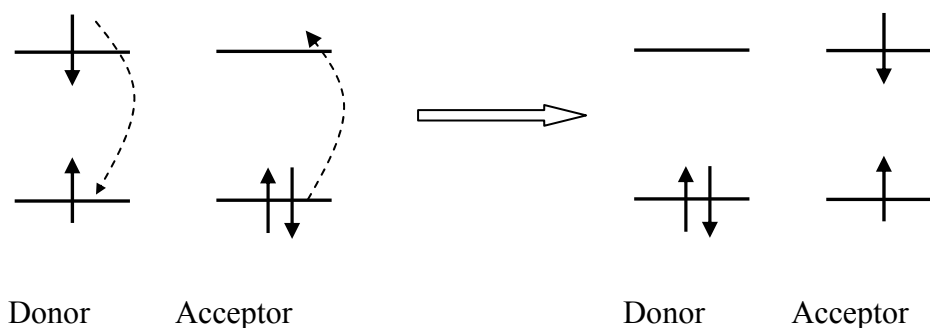
$$L_D = \sqrt{D_e \tau}, \quad (2.12)$$

where D_e is the diffusion constant and τ the exciton lifetime. Normally, four methods are used to measure diffusion of excitons: Bulk quenching, surface quenching, bimolecular recombination, and photoconduction. It is demonstrated that the diffusion length of excitons in fluorescent materials, for example Alq₃, is usually within 10 nm [70]. In phosphorescent materials, it depends strongly on current density applied because of triplet-triplet annihilation and triplet-charge carrier quenching due to the long lifetime of triplet excitons (normally on the order of μ s to ms) [71].

There are generally two mechanisms regarding the energy transfer between molecules (of the same or different type), which are called Förster and Dexter transfer, respectively (see Fig. 2.9). Förster transfer is based on resonant dipole-dipole interaction and mediated by the electromagnetic field so that it can be considered as long range energy transfer (\sim 4-10 nm). The transfer rate depends not only on the overlap between the absorption of the acceptor (A) and the emission spectrum of the donor (D), but also on the local photonic mode density [72]. In this energy transfer, normally spin conservations of both donor and acceptor have to be obeyed so that theoretically, only energy transfer between singlet states is efficient. Dexter transfer

occurs if there is sufficient orbit overlap between molecules so that intermolecular electron exchange could take place at a rate proportional to the orbital overlap of the donor and acceptor molecules. This means that it is a short distance energy transfer (typically ~ 1 nm) via charge carrier exchange. Since only total spin conservation of donor and acceptor is needed in Dexter transfer, both triplet to triplet and singlet to singlet energy transfer are possible. In principle, Dexter transfer is the only mechanism allowing for energy transfer between triplets. Therefore, a much higher phosphorescent dye concentration is usually needed in phosphorescent OLEDs to get maximum efficiency than in fluorescent OLEDs due to this short range of the Dexter process.

a) Förster energy transfer



(b) Dexter energy transfer

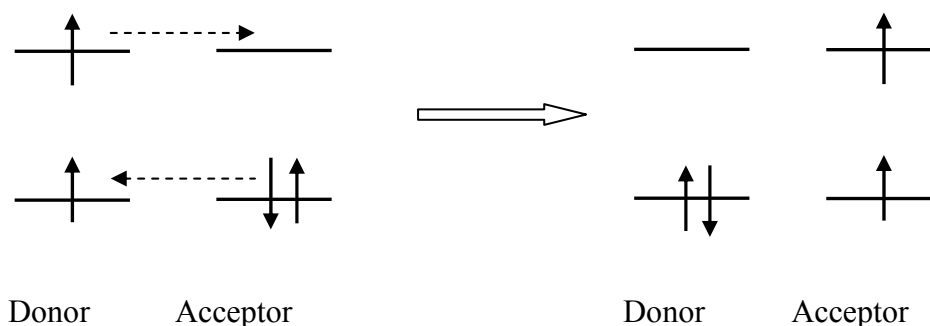


Fig. 2.9. (a) Förster process in singlet-singlet and (b) Dexter process in triplet-triplet energy transfer.

I. Exciton formation in dye doped emissive layers

It is generally accepted that high OLED efficiency and device stability can be achieved by doping of fluorescent [73, 74] or phosphorescent dyes [30] with high photoluminescence quantum efficiencies into wide energy gap host materials where balanced charge injection and efficient transport can occur. In this host-guest system, besides energy transfer from host to guest excitons via Förster or Dexter process, excitons can be formed directly on the guest molecules due to the energy level structure of the dopant that might render it an electron or hole trap, which can

subsequently capture an opposite charge. In this case, the host mainly acts as charge carrier transport layer and dispersive layer to reduce triplet-triplet annihilation and triplet-carrier quenching.

II. Exciton recombination (decay)

As excited states, excitons are not energetically stable and have to decay (recombine) to more stable ground states, losing energy via both radiative and non-radiative processes. Since the ground state of almost all organic molecules is singlet, radiative decay of singlet (fluorescence) is favorable while triplet decay (phosphorescence) is normally not permitted due to spin conservation. However, radiative decay of triplets often occurs also weakly due to spin-orbit coupling. As a result, singlet excitons have a very short lifetime, typically on the order of 10^{-9} s while triplet excitons have a much longer lifetime (from 10^{-6} up to 10^2 s). In addition to radiative decay, there are several other non-radiative decay channels, which involve interaction of excitons with phonons, other excitons, charge carriers, foreign molecules, and structural defects. These non-radiative decays adversely reduce the device efficiency.

2.2.3 Optical processes in OLEDs

Optical processes in OLEDs can be roughly divided into two steps: Light generation in the emission layer and light outcoupling afterwards.

2.2.3.1 Light generation and reabsorption

Light generation is achieved by radiative decay of excitons. It is possible that the generated light can be reabsorbed by constituent organic layers. However, the reabsorption is negligibly small in OLEDs: Emission spectra of almost all organics are red-shifted compared to their corresponding absorption spectrum (called Stokes shift). The shift leads to little absorption of emitted light by themselves, i.e., organics are highly transparent in their own emission bands. In addition, since the other organic layers in OLEDs such as charge carrier transport and blocking layers are usually wide gap materials, light reabsorption in these layers can also be neglected.

2.2.3.2 Light outcoupling

After generation, light needs to be coupled out of the devices via at least one transparent or semitransparent electrode. Since the light is outcoupled from a dense medium to air, part of the light generated within devices suffers total internal reflection and is trapped and finally absorbed in the devices. The latter is the main

energy loss channel in OLEDs up to now.

I. Light outcoupling in conventional bottom-emitting OLEDs

Conventional bottom-emitting OLEDs, which have light coupling out through the bottom substrate, consist of multiple thin organic films (refractive index between 1.6 and 1.8) sandwiched in between an ITO- (refractive index ~ 1.8) coated planar glass substrate (thickness around 1 mm and refractive index around 1.5) and a highly reflective cathode (most often Mg:Al or Al). According to classical ray optics, the emitted light suffers total internal reflection at the substrate/air and organic-ITO/substrate interfaces due to different refractive index of constituent layers. As the result, the emitted light can be roughly classified into three modes as escaped (I), substrate (II), and ITO-organic modes (III), as shown in Fig. 2.10.

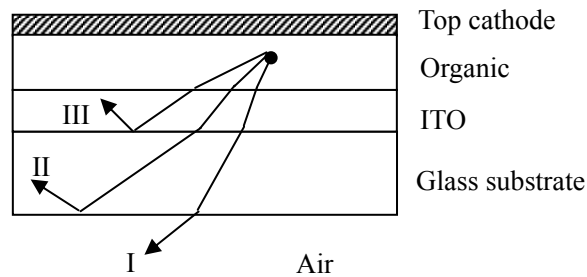


Fig. 2.10. Schematic diagram showing photons emitted into different modes in a typical bottom-emitting OLED.

Based on the assumptions of homogeneous, isotropic emission and a perfectly reflective cathode, the fraction of light outcoupled through the surface can be estimated in a first approximation using classical ray optics, following $\eta_{\text{out}} \approx 1/2n^2$. With the refractive index of organics around 1.7, the calculation indicates that no more than 20% of the light generated inside can be extracted from the device surface. This is a rather rough estimation since the ray optic model does not include optical interference effects between directly emitted and reflected light as well as absorption losses in constituent layers. By taking into consideration interference effects as well using a simple half-space model, Kim et al. calculated that the surface outcoupling efficiency of an OLED is $0.75 n^{-2}$ and $1.2 n^{-2}$ for isotropic and in-plane emission, respectively [75]. Based on a combined classical and quantum mechanical model, Lu et al. demonstrated that the external outcoupling efficiency could be as high as 50% [6]. However, it should be noted that this outcoupling efficiency includes also the light escaped from the edge of the glass substrate, which, for display applications, is useless. With a completely different approach by calculating the power losses of an emissive dipole in a multilayer structure using a classical technique, Smith et al.

demonstrated that the maximum outcoupling efficiency of a conventional bottom-emitting OLED is around 20% [77].

Different schemes have been used to extract the light trapped within the devices and substrates to increase light outcoupling by using, e.g., a microcavity structure [78, 79], an index matching medium [80, 81], shaped substrates [82, 83], polymer microlenses [84], or substrate scattering [85].

II. Light outcoupling in top-emitting OLEDs

In contrast to bottom-emitting OLEDs, light generated within top-emitting OLED is outcoupled from the top contact instead of the bottom substrate. Therefore, no loss of light into substrate zigzag modes is expected. Because of complicated interference processes within the devices, there are only a few publications related to the calculation of outcoupling efficiency of top-emitting OLEDs. It was calculated that in spite of the absence of substrate modes, the maximum outcoupling efficiency of a top-emitting OLED is still around 20% [77, 86], which agrees with experimental results reported so far [87].

2.3 High efficiency top-emitting OLEDs

2.3.1 Definition of efficiency

To evaluate the performance of an OLED, three kinds of efficiencies are mainly used, which are external quantum, power, and current efficiency. The external quantum efficiency is one of the most important indices which can be used to investigate the fundamental device physics responsible for light emission. It is also generally used to compare light outcoupling efficiency between different OLEDs because as a radiometric unit, it does not involve the sensitivity of human eyes. While a photometric unit, the power efficiency is the primary concern of OLEDs for display and lighting applications because it determines the device power consumption at a specified brightness as recognized by human eyes.

2.3.1.1 External quantum efficiency

For display and lighting applications, the external quantum efficiency η_{ext} (in %), is usually defined as the ratio of the number of photons (n_p) emitted in the viewing direction to the number of electrons (n_e) injected which can be expressed as follows [88, 89] :

$$\eta_{ext} = \frac{n_p}{n_e} \times 100\% = \frac{\iint \frac{2\pi E(\lambda, \theta)}{hc/\lambda} \sin \theta d\theta d\lambda}{I/e} \times 100\%, \quad (2.13)$$

where $E(\lambda, \theta)$ is the irradiance of emitted light at viewing angle θ and wavelength λ in W/sr. h is Planck's constant and c is the velocity of light in vacuum. The total number of injected electrons is calculated from the OLED current divided by electron charge (I/e).

Two different methods are used to determine the external quantum efficiency of OLEDs. The first method directly evaluates the total absolute emission intensity of a device with a small emissive surface using calibrated photosensitive detectors. In this method, integrating spheres are often used to accurately measure the absolute emission intensity. It is thus the most precise measurement method of both quantum and power efficiency, although the instruments require absolute calibration. The other method evaluates the absolute luminance of a device using a conventional luminance meter, and then converts luminance values into photon numbers. Although simple, this method is only valid when the device emits perfectly Lambertian and will lead to significant errors especially in the case of top-emitting OLEDs, where the devices show an angular dependence of emission (with respect to both intensity and spectrum)

[88-90].

2.3.1.2 Power and current efficiency

The power efficiency η_P (in lm/W), also called luminous power efficiency, is defined as the ratio of total light output (L_P) in lumens to electrical input power in Watts [88, 91]:

$$\eta_P = \frac{L_P}{IV} = \frac{\iint 2\pi E(\lambda, \theta) g(\lambda) \sin \theta d\theta d\lambda}{IV}. \quad (2.14)$$

As a photometric unit, the photopic response of the eyes has to be taken into account in the calculation of power efficiency, which is described by a spectral shape function, $g(\lambda)$.

The current efficiency η_C (in cd/A) is defined as the ratio of the luminous intensity normally in perpendicular direction to the substrate to the current flowing through the OLED. It is a frequently used display efficiency unit which is convenient for quantifying the properties of an OLED for display applications.

2.3.2 Basics of a microcavity

Because of a highly reflective top cathode and a device thickness on the order of the emission wavelength, conventional bottom-emitting OLEDs already show a weak microcavity effect as a result of wide-angle interference within the devices [92, 93]. The microcavity effect is even stronger in top-emitting OLEDs due to both wide-angle and multiple-beam interference [94, 21]. Therefore, from the optical point of view, a top-emitting OLED can be treated as a planar microcavity.

A microcavity is an optical resonator with one or more dimensions on the order of the optical wavelength. One of the important parameters of a microcavity is its Q factor, which stands for quality factor. For a planar Fabry-Perot microcavity, the Q factor of the cavity is related to the resonance wavelength (λ) of the cavity, cavity optical length (L), and the mode linewidth ($\Delta\lambda$) by [79, 95]:

$$Q = \frac{\lambda}{\Delta\lambda} = \frac{2\pi L}{\lambda} \left[-\ln \sqrt{R_T R_B} \right]^{-1}, \quad (2.15)$$

where R_T and R_B are reflectivity of top and bottom mirrors, respectively.

For a planar microcavity with organics sandwiched in between two metal mirrors, the optical length of the cavity in the direction normal to the cavity, L , is given approximately by [95]:

$$L = \sum_i n_i L_i + L_{m,cathode} + L_{m,anode} \quad (2.16)$$

where n_i and L_i are refractive and thickness of constituent organic layers, respectively. L_m is the effective penetration depth of metal mirrors, which depends on phase change φ_m of light wave (λ) upon reflection at its interface, following [95, 96]:

$$L_m = \frac{\lambda}{4\pi} \varphi_m = \frac{\lambda}{4\pi} \arctan\left(\frac{2n_{org}k_m}{n_{org}^2 - n_m^2 - k_m^2}\right), \quad (2.17)$$

where n_{org} is the refractive index of the organic layer in contact with the metal mirrors. n_m and k_m are the real and imaginary parts of the refractive index of the metals.

The resonance wavelengths (positions of cavity modes) of a cavity are given by the relation $m\lambda_{res}=2L$, where m is the mode index. From Eq. 2.16, it is obvious that the resonance wavelengths of a microcavity can be tuned by altering the thickness of the organic layers and, thus, the optical path length.

It is well known that spontaneous emission is modified in a microcavity, resulting in a redistribution of photon density of states. As a consequence, only those wavelengths that correspond to allowed cavity modes are emitted in a given direction, which leads to spectral narrowing and angular distribution of emission (both color and intensity) with full width at half maximum (FWHM) of the spectrum following [97]:

$$\Delta\lambda_{FWHM} = \frac{\lambda^2}{2L} \times \frac{1 - \sqrt{R_T R_B}}{\pi(R_T R_B)^{1/4}}. \quad (2.18)$$

2.3.3 Factors determining the external quantum efficiency of an OLED

Based on the physical processes involved in OLEDs, one can easily conclude that the external quantum efficiency of an OLED depends not only on the intrinsic properties of the emitter, but also on the electrical and optical structure of the device, following:

$$\eta_{ext} = \eta_{out} \times (\eta_{CB} \times \eta_r \times \eta_{int}), \quad (2.19)$$

where η_{out} is the outcoupling efficiency, which depends on the optical device architecture. η_{CB} represents the charge (electron-hole) balance within the emission layer, which is determined by the electrical properties of the device. Depending on the emission properties of the emitter itself, η_r is the efficiency of formation of an emissive exciton for an electron-hole pair (~ 0.25 for fluorescent and 1 for

phosphorescent emitters) and η_{int} is the intrinsic quantum yield of the emitter.

It is clear from Eq. 2.19 that for achieving high efficiency OLEDs, not only high quantum yield emitters are needed, but also optimized optical and electrical device structures are desired. Last but not least, high power efficiency, which is desirable in display and lighting applications, requires that the device has superior electrical properties and operates under low driving voltage as indicated from Eq. 2.20:

$$\eta_p = \eta_{ext} \times \frac{\overline{h\nu}}{eV}, \quad (2.20)$$

where η_{ext} is the external quantum efficiency. $\overline{h\nu}$ is the average energy of emitted photons. e is the electron charge and V is the device driving voltage.

2.3.4 Ways to improve performance of top-emitting OLEDs

Since light is coupled out through the top contact, one of the key issues for top-emitting OLEDs is to make top contacts which have not only good optical, but also good electrical properties. Sputtered transparent conducting oxides, usually ITO, with an additional buffer layer are widely used as top contact because of their high transmittance in the visible range and a low electrical resistivity [7-10]. However, being a high energy process, sputtering normally introduces energetic ion damage to the underlying organic layers, leading to deterioration of device performance. Many efforts have been exerted on sputtering of ITO top cathodes to reduce the damage of underlying organics by using different buffer layers [8-13] or optimized sputtering processes [14-17]. In both cases, buffer layers have to be used as electron injection layer [8-17]: In the first case, the buffer layers act also as electron injection layer while in the latter case, an additional buffer layer has to be used to improve electron injection from ITO, which has a too high work function and thus leads to a large electron injection barrier. More recently, very thin metal films (15-20 nm) have been introduced as top contact, which can be easily prepared using thermal evaporation [20, 21, 98, 99]. These metal top contacts are semi-transparent with a transmittance no more than 60%, which is much smaller than that of ITO. In spite of this low transmittance of the metal thin film top contact, high efficiency is still achieved in top-emitting OLEDs by carefully manipulating the wide-angle and multiple-beam interferences within the devices [100-102]. With additional organic or other dielectric/semiconductor layers on top of the top contact, the optical properties of the top contact can be tuned and the efficiency of top-emitting diodes can be improved [20, 21, 100-102]. The mechanism of this effect will be investigated in Chapter 4 in detail.

In all OLEDs discussed so far, a low work function metal or a thin electron injection layer has to be used to improve electron injection from the thin metal electrodes [12-14]. To get high efficiency top-emitting OLEDs, highly reflective metals such as Ag are always used as bottom anode. However, to have good hole injection, the surface Ag anode is always modified [98, 103] or additional high work function metals have to be used [18, 21, 104], which unfortunately reduces the reflectivity of the bottom anode. All those techniques used to improve the charge carrier injection and, thus, the electrical properties of the devices, inevitably compromise the optical device structure. In addition, both optical and electrical device structures depend on constituent organic layer thickness. This makes optimization of both optical and electrical device structures even more difficult.

In our group, high efficiency bottom-emitting OLEDs have been demonstrated with ultra-low operating voltages by using electrical doping of hole and electron transport layers [105-107]. In this work, it is demonstrated that this doping technique is even more crucial for achieving high efficiency top-emitting OLEDs, with the possibility to optimize both optical and electrical device properties simultaneously. Therefore, it is necessary to introduce and review the mechanism of doping. As an example, p-type doping is discussed in the following Section.

2.3.5 Doping basics

Similar to inorganic semiconductors, it has been demonstrated that organic semiconductors can also be efficiently doped with molecular donors or acceptors with appropriate molecular matrix/dopant systems. Using zinc-phthalocyanine (ZnPc) doped with 2,3,5,6-tetrafluoro-7,7,8,8-tetracyano-quinodimethane (F₄-TCNQ) as a p-type model system, Pfeiffer et al. conducted a basic study of p-type doping and found that the conductivity of the doped ZnPc layer increased superlinearly with doping concentration, as shown in Fig. 2.11 [32].

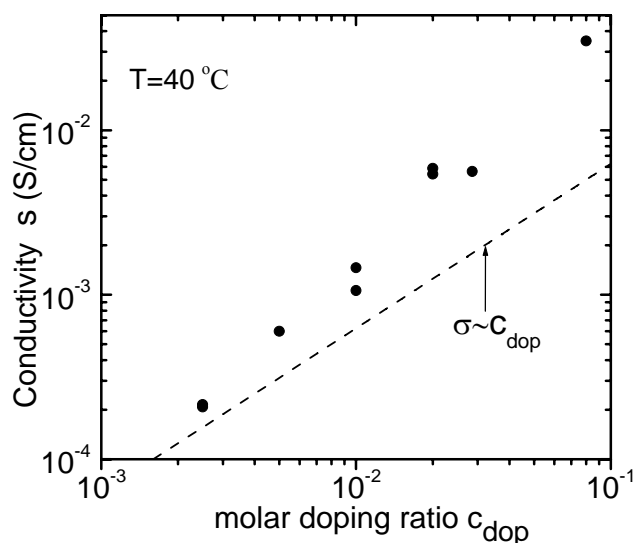


Fig.2.11. Conductivity of doped ZnPc with F₄-TCNQ vs. doping concentration at 40 °C. The dashed line represents a linear dependence (reprinted from [32]).

They further investigated the doping mechanism by measuring the Seebeck (thermopower) effect^f, in which the conduction type and the energetic distance between the Fermi level (E_F) and the transport level (E_h) in the doped organic layers can be determined by^g [32]:

$$S(T) = \frac{E_F(T) - E_h}{eT} = \frac{k_B}{e} \ln \left\{ \frac{N_h - p(T)}{p(T)} \right\} \approx \frac{k_B}{eT} \ln \left\{ \frac{N_h}{p(T)} \right\}, \quad (2.21)$$

where T is the absolute temperature, p the hole density and k_B the Boltzmann constant. As shown in Fig. 2.12, with increasing dopant concentration, S decreases and the Fermi level approaches the transport level with the increase of hole density. It is therefore concluded that upon doping, electron transfer from the matrix (ZnPc) to the dopant molecules (F₄-TCNQ) leads to an increased number of mobile holes, thus increasing the conductivity.

^f In the Seebeck measurement, one measures the thermovoltage V_{12} between two contacts which have temperature difference of ΔT . The Seebeck coefficient is defined as: $S(T) = \lim_{\Delta T \rightarrow 0} \frac{V_{12}(T, \Delta T)}{\Delta T}$.

^g One assumes hopping transport of charge carriers take places homogeneously at nearly one transport level.

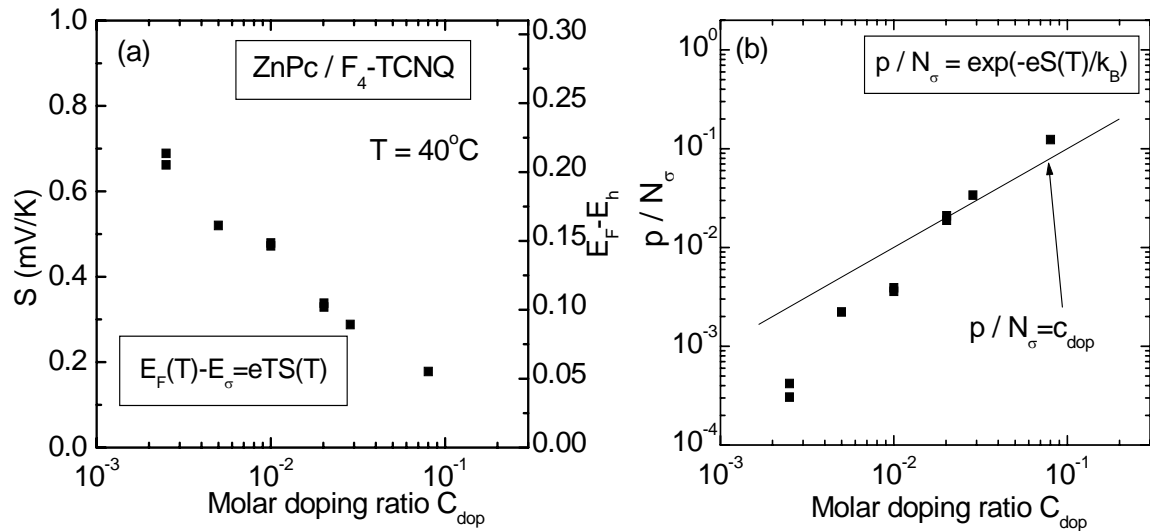


Fig. 2.12. (a) Seebeck coefficient (left axis) and energetic difference between the Fermi level E_F and the hole transport state E_h (right axis) vs. doping ratio measured at 40 °C, and (b) calculated hole density per total density of states N_h at the transport state E_h vs. doping density. The line for 100 % doping efficiency ($C_{dop} = p/N_h$) is also shown (reprinted from [32]).

Another advantage of doping is that doping leads to very thin (<5 nm) space charge layers as a result of energy level bending at contacts associated with efficient charge carrier injection, as shown in an organic/metal interface study (see Fig. 2.13) [105].

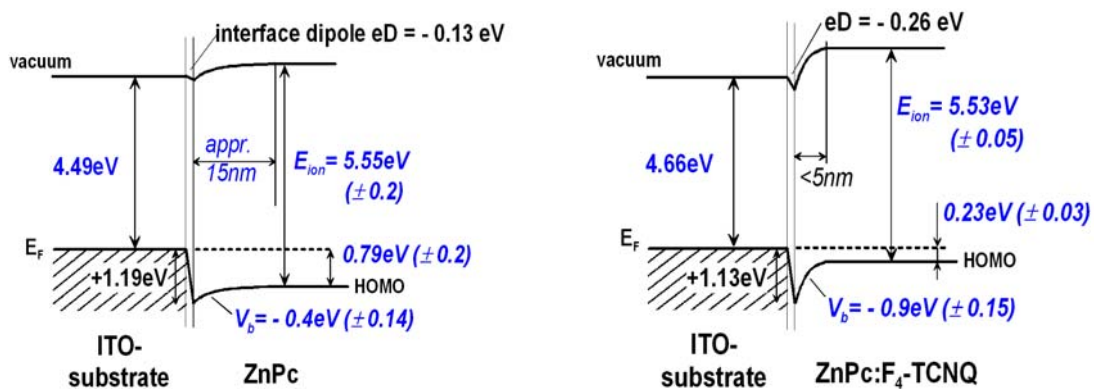


Fig. 2.13. Energy diagram as derived from UPS/XPS spectroscopy for the organic semiconductor ZnPc on ITO. Left side: undoped ZnPc on ITO; right side: ZnPc doped with F₄-TCNQ (reprinted from [105]).

Recently, electrically doped charge carrier transport layers (both p-doped hole transport layer and n-doped electron transport layer) have been successfully incorporated in OLEDs in our group, which results in high performance devices in terms of driving voltages and efficiency [106-110].

Chapter 3

Materials and experiments

In this Chapter, the main organic materials used in this study will be introduced, which includes their molecular structures and relevant physical properties. Then, device preparation and characterizations will be presented, which is followed by the description of all main experimental methods used in this study.

3.1 Materials and their properties

3.1.1 Hole conduction materials for hole transport and electron blocking

A typical hole conduction material usually has a hole mobility several orders of magnitude higher than its electron mobility so that its electron transport ability can be neglected. Hole conduction materials were used in this study as matrix of the hole transport layer, as electron blocker, and as matrix for the emission layer. Most of the hole conduction materials normally used in OLEDs are based on the basic structure of tri-phenylamines [111, 112].

1. N,N,N',N'-tetrakis(4-methoxyphenyl)-benzidine (MeO-TPD)

MeO-TPD (see Fig. 3.1) was used in this study as a matrix for the hole transport layers with a HOMO around -5.1 eV. Upon p-type doping by F₄-TCNQ (2 mol% doping concentration), its conductivity can reach 5×10^{-6} S/cm, which is a big advantage for device operating voltage. The major disadvantage of MeO-TPD is its low glass transition temperature T_g , which is only around 55 °C. This will lead to stability problems at elevated temperatures. In addition to MeO-TPD, another hole conduction matrix called NHT5 (from Novaled AG) has also been used, which is comparable to MeO-TPD regarding electrical properties, but more stable due to its

high T_g (145 °C)^h.

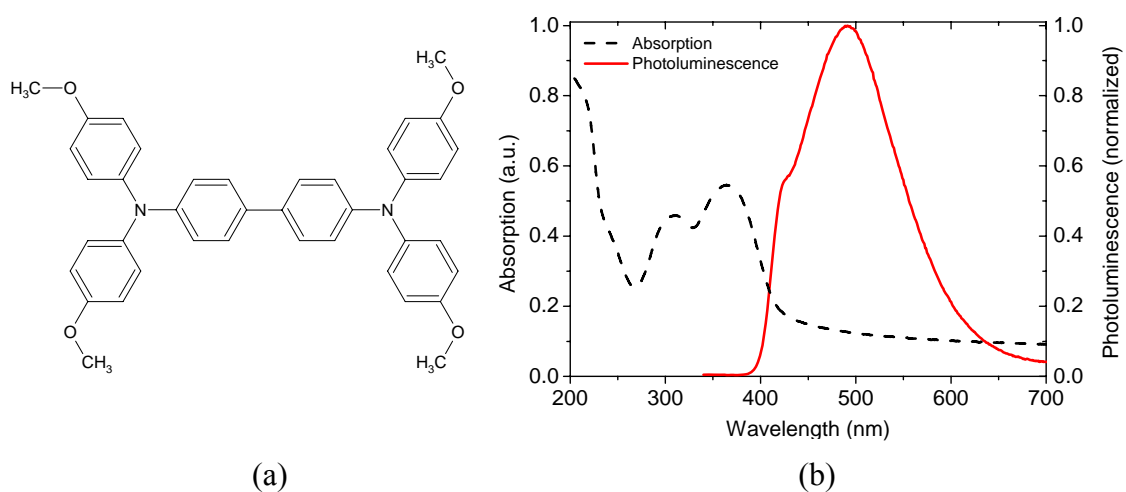


Fig. 3.1. (a) Molecular structure of MeO-TPD and (b) its absorption and photoluminescence spectra.

2. 2,2',7,7'-tetrakis-(N,N-diphenylamino)-9,9'-spirobifluorene (Spiro-TAD)

As a wide gap hole conduction material with a high lying LUMO around -2.2 eV, Spiro-TAD can work effectively as an electron blocker in OLEDs. Further, it has a suitable HOMO around -5.4 eV, which is well in between the HOMOs of hole transport layer and emission layer. Further advantages of Spiro-TAD are its high glass transition temperature and high thermal stability, both of which are due to its spiro-bridged core structure. Fig. 3.2 shows molecular structure, absorption and photoluminescence spectra of Spiro-TAD.

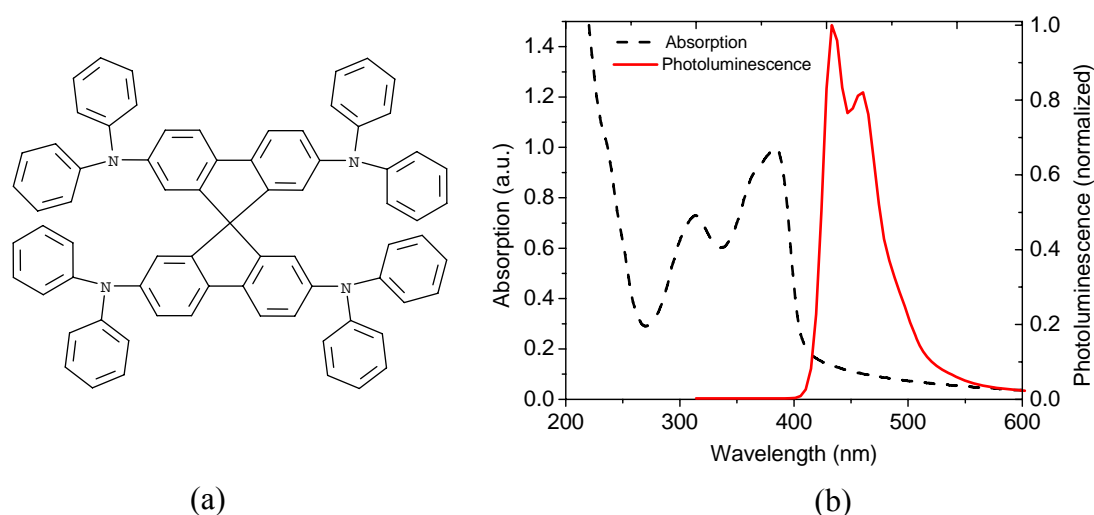


Fig.3.2. (a) Molecular structure of Spiro-TAD and (b) its absorption and photoluminescence spectra.

^h NHT5 is a proprietary material of Novaled. Therefore, its molecular structure may not be disclosed.

3. N, N'-di(naphthalen-2-yl)-N, N'-diphenyl-benzidine (α -NPD)

NPD is one of the most widely used hole transport materials in OLEDs so far with its HOMO between -5.5 eV and -5.7 eV. Although the glass transition temperature of NPD is not very high (T_g around 96 °C), it has quite good stability against radical anions. With a low LUMO around -2.6 eV, NPD can also be used as an electron blocking layer. In this study, it was used mainly as electron blocking layer and as a matrix for the red phosphorescent dye in red OLEDs. Its molecular structure, absorption and photoluminescence spectra are shown in Fig 3.3.

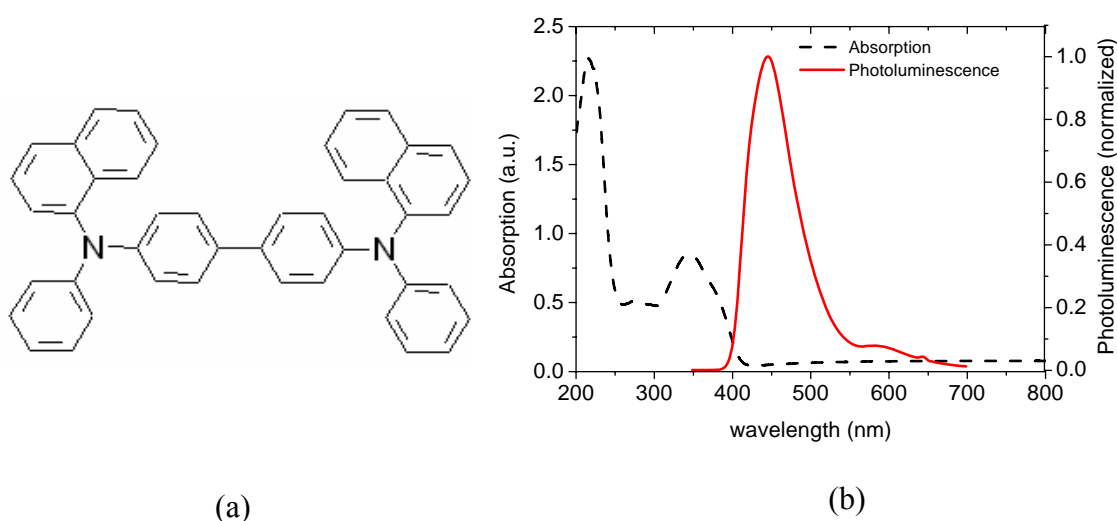


Fig. 3.3. (a) Molecular structure of α -NPD and (b) its absorption and photoluminescence spectra.

3.1.2 Electron conduction materials for electron transport and hole blocking

In contrast to hole conduction materials, an electron transport material has much smaller hole mobility compared to its electron mobility. They were used in this study as matrix of the electron transport layer and as the hole blocking layer.

1. 4,7-diphenyl-1,10-phenanthroline (Bphen)

As a wide gap material (LUMO \sim -3.0 eV, HOMO \sim -6.4 eV [113]) with a high electron mobility which is around 10^{-4} cm²/Vs [114], Bphen is suitable both as electron transporter and hole blocker. In this study, Bphen was mainly used as a matrix for the electron transport layer, which can be effectively n-doped by cesium (Cs) with the conductivity of doped layer reaching 10^{-5} S/cm. However, because of its low glass transition temperature of 62 °C [115], Bphen is morphologically unstable and tends to crystallize. This may lead to relatively short lifetime especially when Bphen is used as hole blocking layer [115]. The molecular structure of Bphen and its

absorption and photoluminescence spectra are shown in Fig. 3.4.

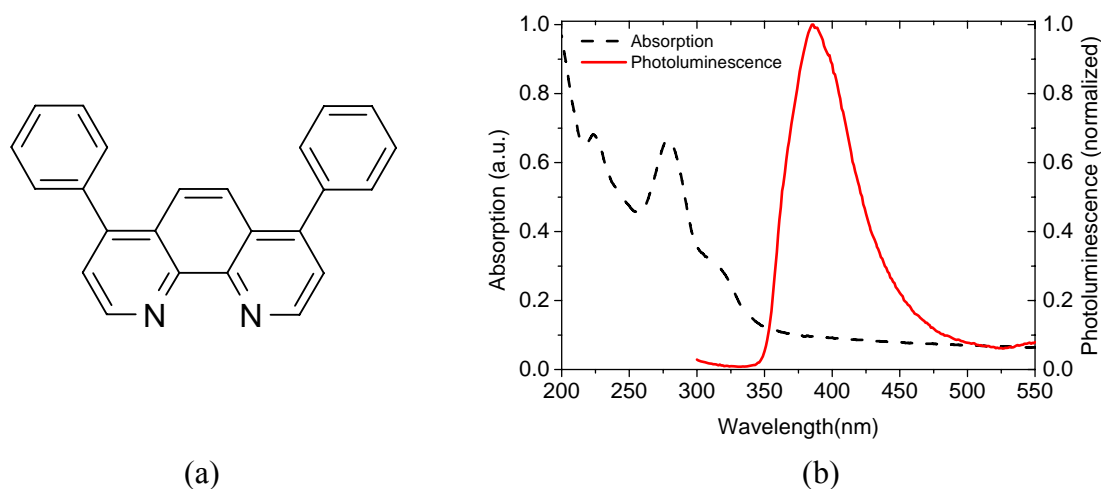


Fig. 3.4. (a) Molecular structure of Bphen and (b) its absorption and photoluminescence spectra.

2. Bis(2-methyl-8-quinolinolato)-(para-phenylphenolato)-aluminium(III) (BALq)

As another wide gap electron conduction material, BALq was also used (molecular structure shown in Fig. 3.5). Its LUMO and HOMO are at around -3.3 eV and -6.5 eV, respectively. Although it has a much lower electron mobility than Bphen, due to its higher glass transition temperature, which is around 92 °C [115], it is still relevant. Therefore, BALq has been used as hole blocker in OLEDs to achieve better device lifetime [116].

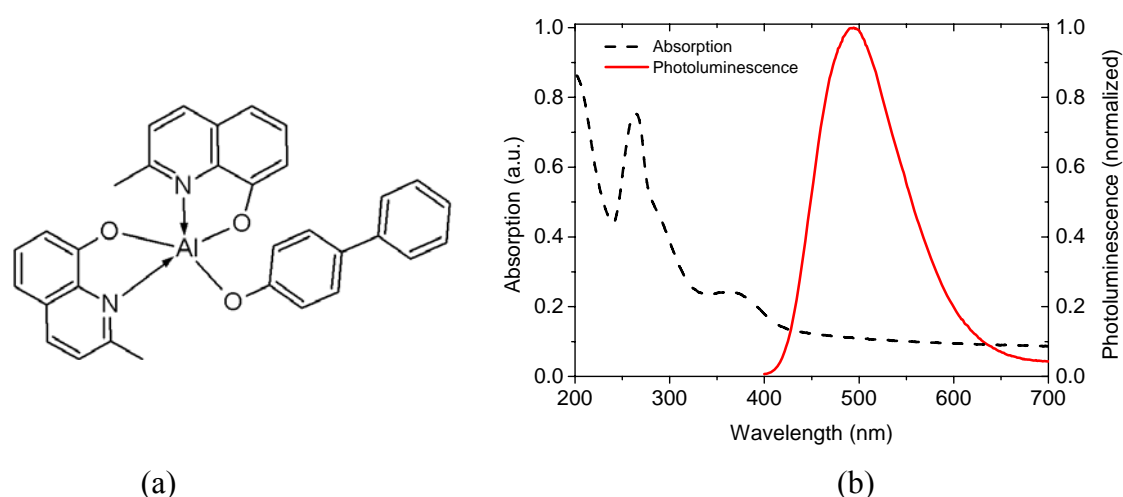


Fig. 3.5. (a) Molecular structure of BALq and (b) its absorption and photoluminescence spectra.

3.1.3 Host materials for emissive dopants

As discussed in Chapter 2, one of the key developments in OLED technology was the invention of the guest-host emitter system which combines good transport

properties of host materials and high photoluminescence efficiency of guest dyes with desired colors [73]. Another advantage of this guest-host system is the enhancement of the device stability by the transport of electro-generated excitons or direct exciton formation on highly emissive and stable dopant sites [74]. The primary criterion of a host material is the energetic location of its singlet (for fluorescent dopants) or triplet state (for phosphorescent dopants), which have to be larger than those of the corresponding dopants to have an efficient energy transfer of excited states or direct charge carrier trapping.

1. 4,4',4''-tris(N-carbazolyl)-triphenylamine (TCTA)

TCTA (see Fig. 3.6) is an ambipolar transporter with preferred hole transport ability. Because of its large triplet state energy gap, it has been used as host material for green and blue phosphorescent dyes in this study [117]. Its LUMO and HOMO are at -2.7 eV and -5.9 eV, respectively [118].

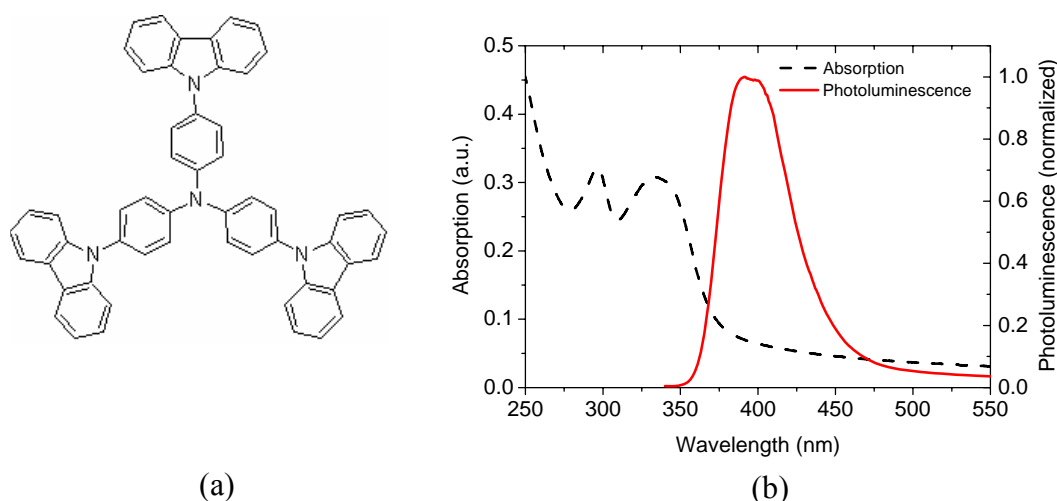


Fig. 3.6. (a) Molecular structure of TCTA and (b) its absorption and photoluminescence spectra.

2. 2,2',2''-(1,3,5-benzenetriyl)tris[1-phenyl-1H-benzimidazole] (TPBI)

Although TPBI (see Fig. 3.7) is sometimes regarded as also an ambipolar transporter [119], its electron transport capability is dominant [120]. In this study, TPBI was mainly used as matrix for the green phosphorescent dopant with its LUMO and HOMO at -2.7 eV and -6.2 eV, respectively [121]. Because of its high HOMO, TPBI can also be used as hole blocking material [120].

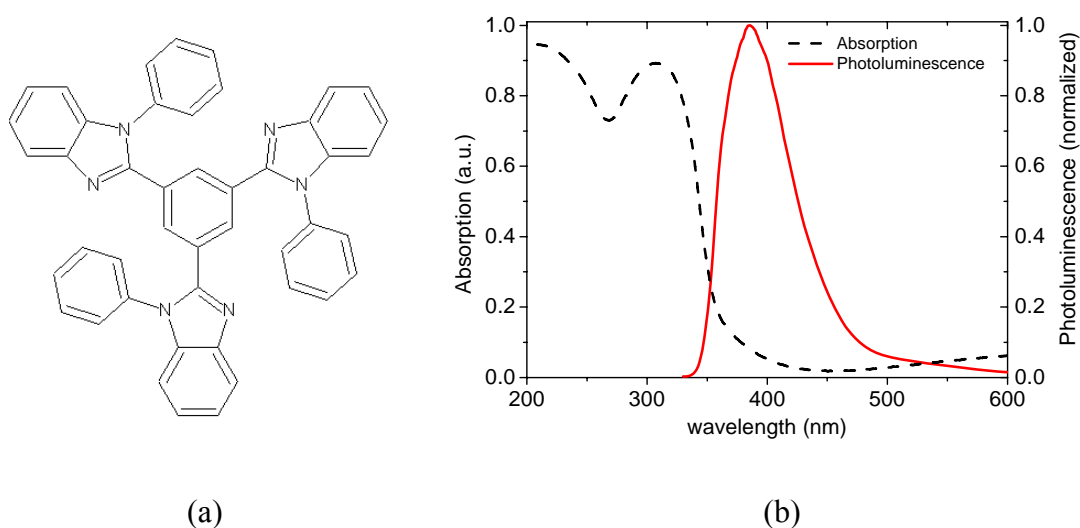


Fig. 3.7. (a) Molecular structure of TPBI and (b) its absorption and photoluminescence spectra.

3.1.4 Emitters and emissive dopants

1. 2,2',7,7'-tetrakis(2,2-diphenylvinyl)spiro-9,9'-bifluorene (Spiro-DPVBi)

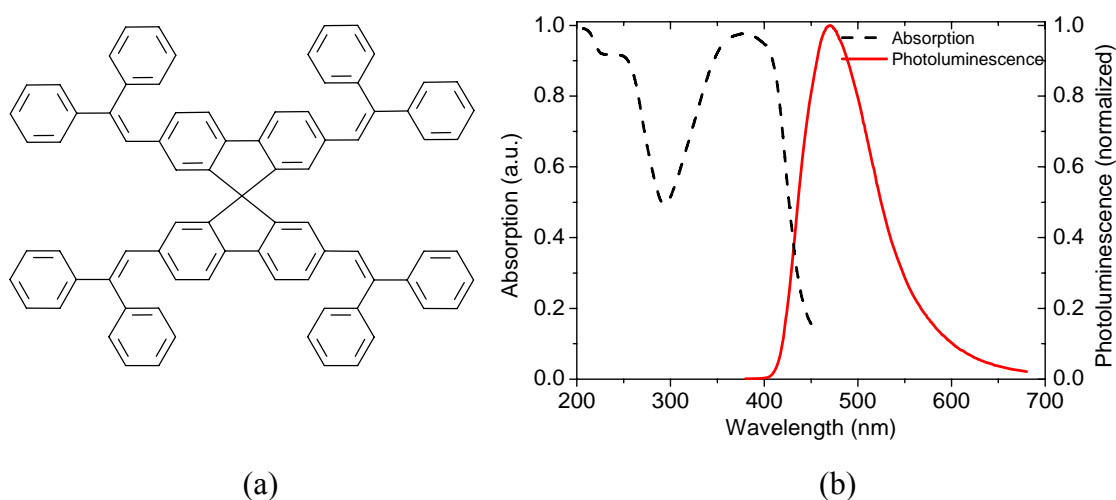


Fig.3.8. (a) Molecular structure of Spiro-DPVBi and (b) its absorption and photoluminescence spectra.

Spiro-DPVBi is a well known fluorescent material from the study of organic lasers with an emission in the light blue range (see Fig. 3.8). Being a spiro compound, it has a high glass transition temperature of 130 °C with LUMO and HOMO at -2.8 eV and -5.6 eV, respectively [122]. Although Ruhstaller et al. reported that Spiro-DPVBi has comparable hole and electron mobility around $2 \times 10^{-8} \text{ cm}^2/\text{Vs}$ [123], our experiments indicated that it is rather an electron transporter.

2. 9,10-Bis(9,9'-spirobi[9H-fluorene]-2-yl)anthracene (Spiro-Anthracene)

Spiro-Anthracene is another fluorescent emitter with relatively high efficiency and deep blue emission as shown in Fig. 3.9 [110]. In spite of above advantages, OLEDs using Spiro-Anthracene as emitter show a short lifetime, which limits its practical application.

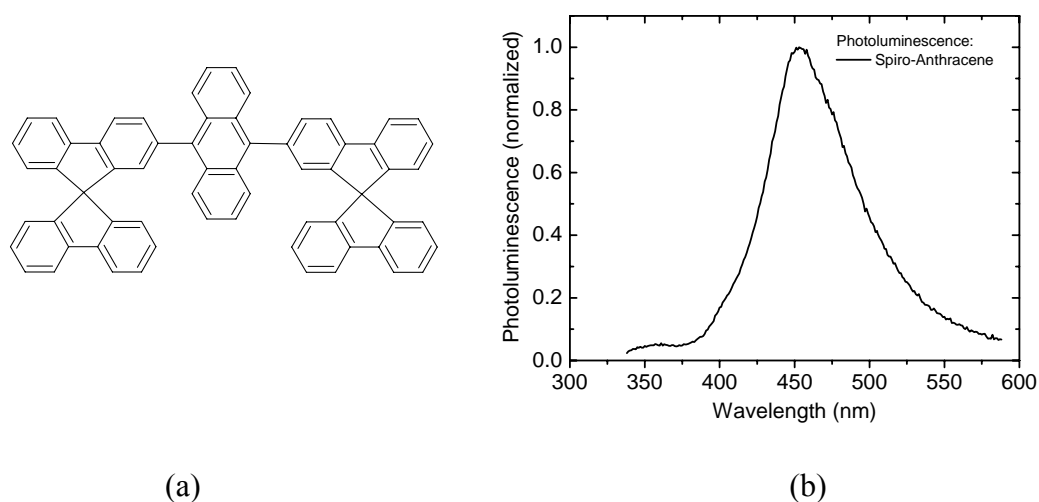
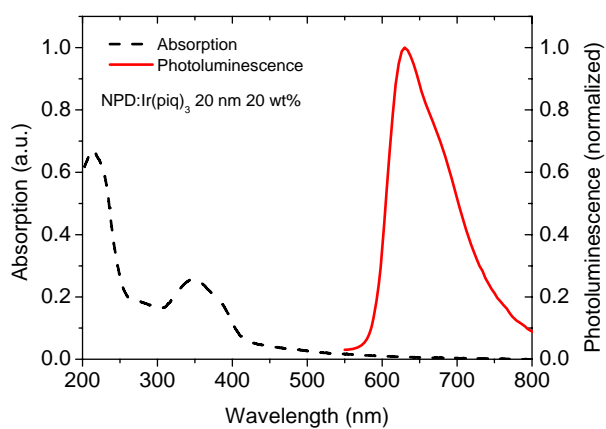
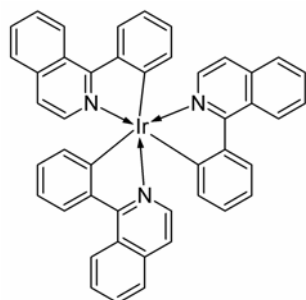
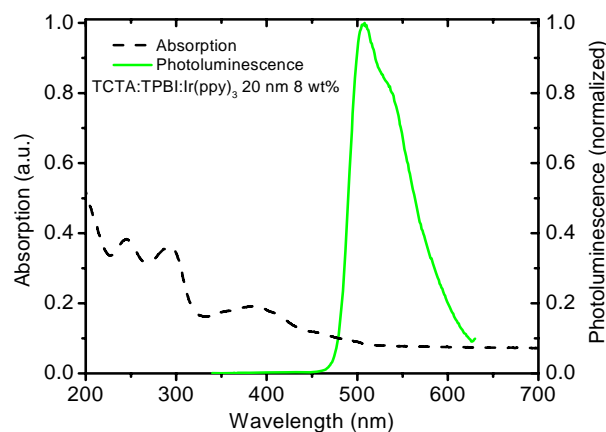
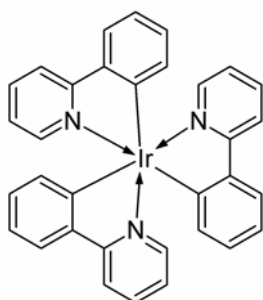


Fig. 3.9. (a) Molecular structure of Spiro-Anthracene and (b) its photoluminescence spectrum.

3. Phosphorescent dopants

All three phosphorescent dyes used in this study are iridium based metal complexes, which are tris(1-phenylisoquinoline)iridium $[\text{Ir}(\text{piq})_3]$ [124], tris(2-phenylpyridine) iridium $[\text{Ir}(\text{ppy})_3]$ [125], and iridium(III) bis[(4,6-difluorophenyl)-pyridinato-N,C2]picolinate (FIrpic) [126] for red, green and blue emission, respectively (molecular structures in Fig. 3.10). In red phosphorescent devices, $\text{Ir}(\text{piq})_3$ doped NPD with a doping concentration of 20 wt% was used as emission layer. In green phosphorescent devices, double emission layers were used, which consist of both $\text{Ir}(\text{ppy})_3$ doped TCTA and TPBI with the same doping concentration of 8 wt%. For blue phosphorescent devices, TCTA doped with FIrpic was used as emission layer with a doping concentration of 12 wt%. The photoluminescence spectra of all three triplet emitters in their corresponding matrices are also shown in Fig. 3.10.

(a) Ir(piq)₃(b) Ir(ppy)₃

(c) FIrpic

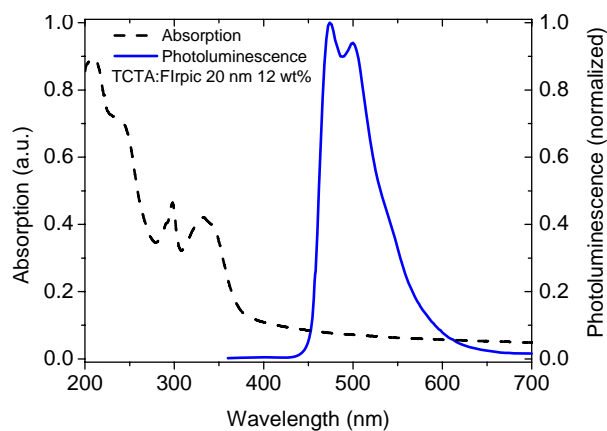
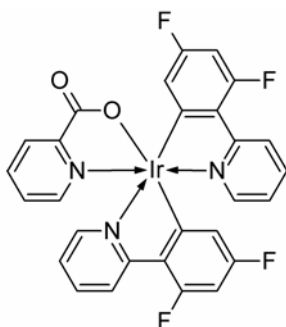


Fig. 3.10. (left) Molecular structures and (right) Absorption and photoluminescence spectra of (a) Ir(piq)₃ (20 wt%), (b) Ir(ppy)₃ (8 wt%) and (c) FIrpic (12 wt%) in corresponding matrices.

3.1.5 Electrical dopants

Because of the big advantages of electrical doping of charge carrier transport layers [107-112], p-doped MeO-TPD and n-doped Bphen have been used in this study as hole and electron transport layers, respectively.

1. p-dopant: 2,3,5,6-tetrafluoro-7,7,8,8-tetracyano-quinodimethane (F₄-TCNQ)

With a deep LUMO around -5.2 eV [32], which is in resonance with the HOMO of MeO-TPD, CuPc and some other hole transport materials, F₄-TCNQ (see Fig. 3.11) works effectively as an acceptor in the matrix of MeO-TPD and several other hole transport materials. The sublimation temperature of F₄-TCNQ, however, is quite low (between 90-100 °C), which limits its applicability for devices at high temperature. Therefore, another more stable p-type dopant with an evaporation temperature of more than 120 °C, called NDP2 (from Novaled AG) [127], has been used in this study as well. The doping process (p-type) is schematically illustrated in Fig. 3.12, where the matrix (MeO-TPD, NHT5 etc.) acts as the electron donor and the dopant (F₄-TCNQ for MeO-TPD or NDP2 for NHT5) as the electron acceptor.

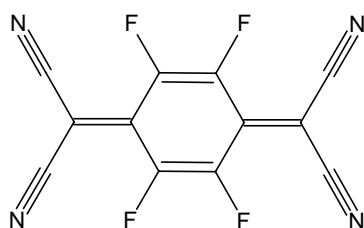


Fig. 3.11. Molecular structure of F₄-TCNQ.

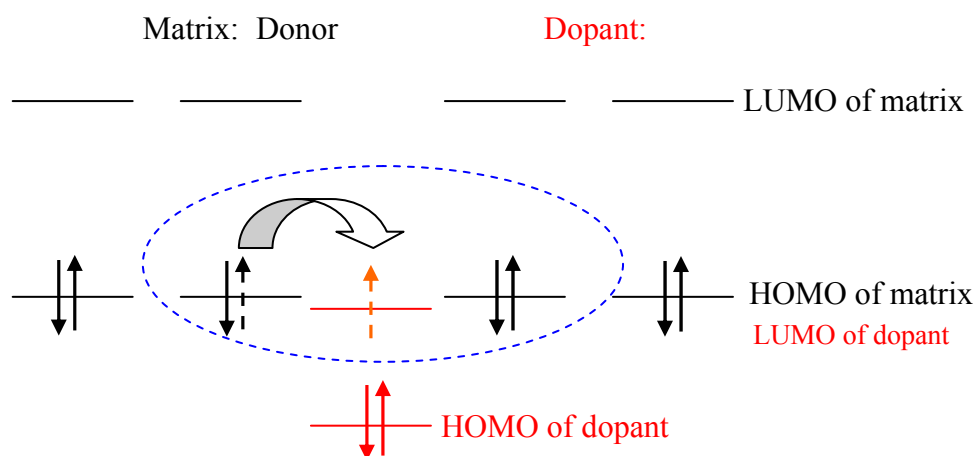


Fig. 3.12. Schematic illustration of p-type doping where electron transfer from matrix to dopant is shown.

2. n-dopant: Cesium (Cs)

Although there are already some molecular n-dopants available for organic solar cells [125], n-type doping of electron transport layers in OLEDs is still carried out mainly using alkali metals like Li or Cs [107, 110]. With their LUMO around -3 eV, these electron transport materials are weak electron acceptors. This imposes rigorous requirements on the position of the HOMO of the donors (has to be also around -3 eV), which is difficult to meet [128]. More recently, Novaled AG developed a new type of molecular n-dopant, called NDN-1, which can be used as an effective donor in an electron transport matrix called NET5 [127]. However, both are proprietary materials of Novaled.

In this study, Cs was used as n-dopant and Bphen as host for the electron transport layer by co-evaporation of them.

3.1.6 Purification of organic materials

The purity of organic materials is of great importance for the device performance and lifetime [129]. Therefore, all organic materials used in this study have been purified by gradient sublimation in high vacuum at least twice before they were used.

3.2 OLED preparation and measurements

Most of the OLEDs in this study were prepared in a multiple-chamber ultra-high vacuum system with a base pressure around 10^{-8} mbar. This cluster tool allows making transport, emission and metallization layers in different chambers without breaking the vacuum. Because each of the four organic material evaporation chambers of this tool can hold at least 4 sources, it is possible to make organic optoelectronic devices with very complex structures. The rest of the samples were fabricated in a custom-made vacuum system from K.J. Lesker with a base pressure around 10^{-8} mbar. The main advantage of this equipment is that 16 independent groups of samples can be made at the same time, which are arranged in a matrix of 4×4 with 4 devices in each group. In both tools, calibrated crystal quartz monitors were used to precisely control the deposition rate and the thickness of every layer. The deposition rate for the electrodes, HTL, ETL and outcoupling layer was 1 Å/s. For all the other layers, a lower evaporation rate of 0.3 Å/s was used.

All metal pre-coated glass substrates in this study were provided by the Lehrstuhl für Bildschirmtechnik of University of Stuttgart (LfB). All ITO pre-coated glass substrates were from Thin Film Devices Inc. having a sheet resistance of $\sim 30 \Omega/\text{sq}$. Substrates were cleaned using a multi-step solvent process with the following

procedure: In an ultrasonic bath, the substrates were cleaned first in acetone and then in ethanol for 20 and 8 minutes, respectively. After rinsing in de-ionized water for 5 minutes, the substrates were dried with nitrogen gas and loaded into the deposition system.

Samples were usually measured in vacuum with a Keithley 2400 source measure unit for electrical data and a calibrated Si photodiode mounted above the OLED for collecting the emitted light in forward direction. The electroluminescence spectra were obtained using a Sentronic PL-USB2000 spectrometer. For lifetime and other measurements in air, the samples were encapsulated in a glove box attached to the vacuum system by covering the active device area with cavity glasses and glueing the edges with a two-component epoxy glue. The power and external quantum efficiencies of the devices were measured in a calibrated integrating sphere at Novaled AG. The angular dependence measurements were performed using an Autronic Melchers goniometer DMS-401 at Fraunhofer IPMS.

3.3 Experimental methods

3.3.1 Impedance spectroscopy

Impedance spectroscopy is a powerful method for investigating many of the electrical properties of dielectric materials (either liquid or solid), interfaces between them or their interfaces with electrodes by assessing the frequency response of them [130]. In this method, normally impedance is measured directly in the frequency domain by applying a modulation signal (single-frequency voltage) to the interface and measuring the phase shift and amplitude, or real and imaginary parts of the resulting current at that frequency. In this spectroscopy, if the capacitance is measured as the function of frequency under a specific bias voltage, the measurement is called capacitance-frequency (C-f) spectroscopy, whereas it is called capacitance-voltage (C-V) measurement when capacitance is measured as the function of bias voltage at a specific frequency.

In this study, the impedance of the devices was measured directly using a Hewlett-Packard 4284A LCR meter with the amplitude of the modulation signal (V_{dc}) being 20 mV. The C-f spectra were carried out at frequencies ranging from 20 Hz to 1 MHz. Using the simplest equivalent circuit model of only one RC unit, the total capacitance (C_p) and resistance (R_p) of an organic device can be calculated by:

$$C_p = \frac{X}{\omega(X^2 + R^2)}, \quad (3.1)$$

$$R_p = \frac{R^2 + X^2}{R}, \quad (3.2)$$

where R and X are the resistive and capacitance components of the device impedance ($Z=R(\omega)-jX(\omega)$) at the frequency ω .

Normally, a C-f spectrum is analyzed using equivalent circuit models. Having structures of several organic layers sandwiched in between two electrodes, organic diodes can be treated as planar capacitors and their impedance spectra can be understood based on equivalent circuit models with RC units (each unit consisting of a resistor in parallel with a capacitor) representing bulk or heterojunction regions. In the model, resistances represent conductive paths, and thus a given resistor in the circuit might account for the bulk conductivity of the material or conductivity of the characteristic region (depletion, barrier, contact regions etc). Similarly, capacitances will be generally associated with space charge polarization regions. It is known that the dielectric relaxation time of a material is roughly proportional to its resistance, i.e. the lower the conductivity, the longer the dielectric relaxation. Therefore, from the C-f spectra it is possible to distinguish the capacitance contribution from layers or regions with very different conductivity. Taking a hole only device as an example, which has the structure of ITO/ p-NHT5 (15 nm)/ NHT5 (100 nm)/ p-NHT5 (15 nm)/ Ag (30 nm), the C-f spectrum of the device is shown in Fig. 3.13a. In the moderate frequency range between 800 and 10000 Hz, the capacitance of the device drops drastically, which is mainly attributed to the relaxation of the bulk layer (intrinsic layer including depletion layer). This is because the relaxation of the doped layer can only take place at high frequencies beyond 10^5 Hz due to its high conductivity (around 10^{-5} S/cm). Consequently, capacitances at low frequencies (< 700 Hz) can only be assigned to a barrier layer at the p-NHT5/Au top interface since it is known that the bottom contact is ohmic. Based on above analysis, an equivalent circuit model (see Fig. 3.12b) can be built to simulate the device structure. The model consists of three single RC components, which are: C_i-R_i for the intrinsic NHT5 layer (including a possible depletion layer), C_d-R_d for the p-doped NHT5 layer (30 nm), and C_B-R_B for the barrier at the top interfaces. Additionally, a series resistor is included to represent the contact (electrodes and lead wire) resistance [131, 132]. To fit the C-f curve well, distributed impedance elements, for example constant phase elements (CPEs), are always used to replace the ideal circuit elements (capacitors, resistors etc.) in the circuit model due to a distribution of energy states or a spatially distributed conductivity of organic materials [130].

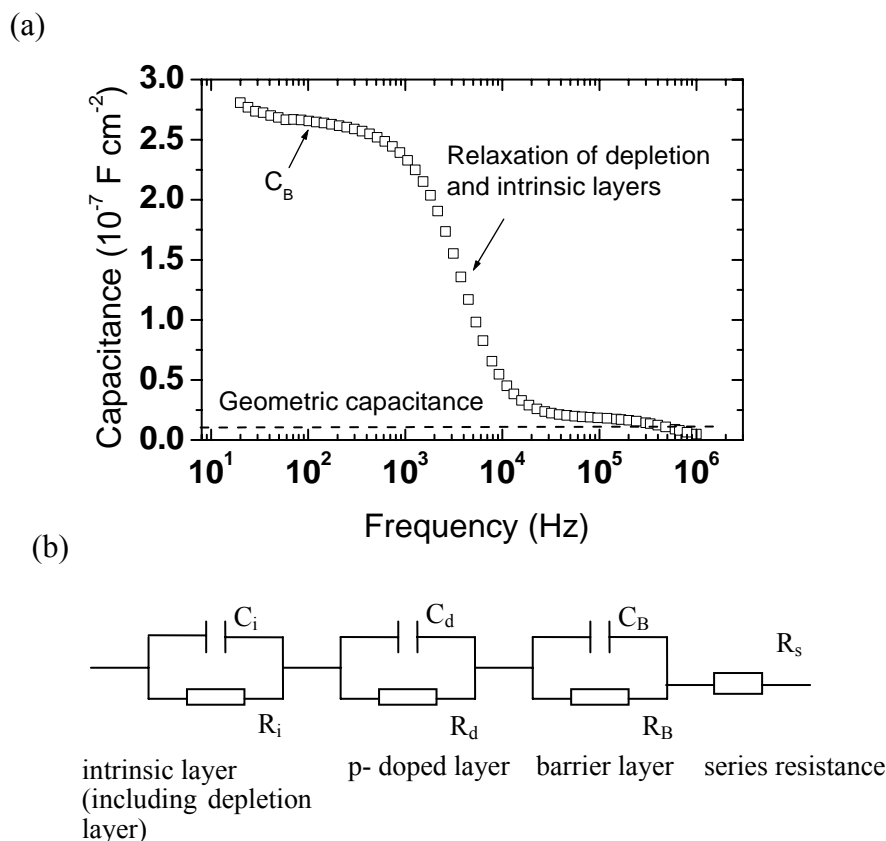


Fig. 3.13. (a) C-f spectrum of a hole only device and (b) the equivalent circuit model of the device with the following structure: ITO/ p-NHT5 (15 nm, 1.5 mol%)/ NHT5 (100 nm)/ p-NHT5 (15 nm, 1.5 mol%)/ Ag (30 nm).

For an organic electronic device, it is known that injection limitation is normally relevant in the low voltage range, while space charge limitation (SCLC) becomes more relevant at high bias as a result of barrier lowering by the external electric field so that at least one contact is able to provide more carriers than the material can transport away. These space charges do not only determine the I-V characteristics, but also lead to a characteristic frequency and bias-dependent electrical response [133]. Therefore, it is possible to use C-f and C-V spectra of devices to compare the injection capability of relevant contacts since the V_{dc} probes the existing space charge in the device and injects new charges. In this study, C-V and C-f spectra were used to analyze charge carrier injection in single carrier devices.

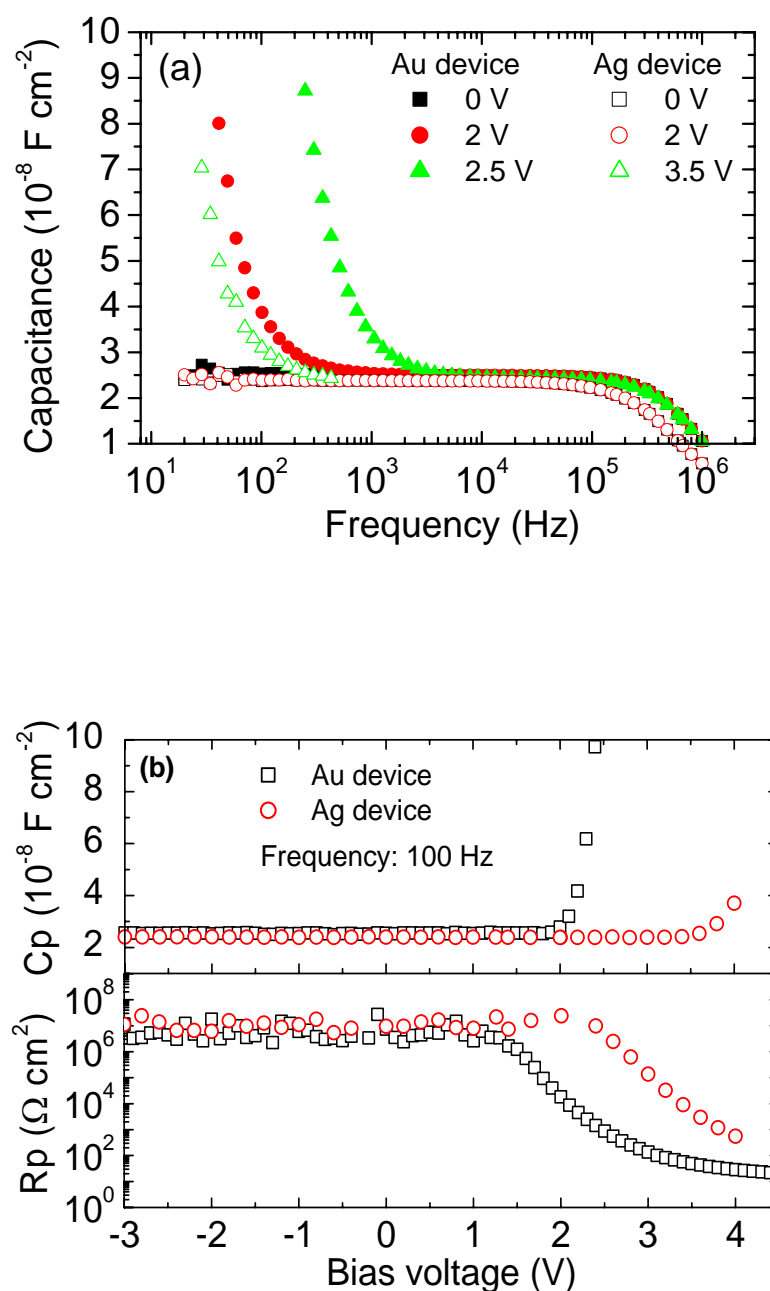


Fig. 3.14. (a) C-f spectra of two hole only devices at different voltages (bottom biased) and (b) C-V (top) and C-R spectra (bottom) of the devices. The devices have the following structures: ITO/p-NHT5 (15 nm, 1.5 mol%)/ NHT5 (100 nm)/ Au or Ag (30 nm).

Two hole only devices are used here as examples, which have the device structure of ITO/ p-NHT5 (15 nm, 1.5 mol%)/ NHT5 (100 nm)/ Au or Ag (30 nm), respectively. Fig 3.14a compares C-f spectra of the devices at different bottom positively biased voltages (bottom injection). With zero bias, the devices have similar C-f spectra. At the bias above 2 V, the Au device starts to show strong capacitance increase towards

lower frequency below a threshold frequency (f_{th}), indicating existence of space charges (SCLC) in the device. However, only at the bias of 3.5 V, does the C-f spectrum of the Ag device show this behavior. This means that although the bottom hole injection in both the devices is from ITO into p-NHT5, the effective injection barriers in both the devices are apparently different: The OLED using an Au top contact has a smaller effective bottom injection barrier for holes than the device based on Ag. The strong capacitance increase towards lower frequency is believed to be due to the disordered nature of the NHT5 layer, which leads to dispersive transport in the layer. The increase of the f_{th} towards higher bias voltage is mainly due to the decrease in average transit time of charge carriers with increase of the bias voltage. The difference in the effective bottom injection barriers of the two devices is further confirmed by their C-V spectra in Fig. 3.14 b.

3.3.2 Photoelectron spectroscopy (UPS/XPS)

Photoelectron spectroscopy involves irradiating a sample with photons of a characteristic energy and measuring the flux of electrons that leaves the surface. By utilizing photo-ionization and energy-dispersive analysis of the emitted photoelectrons, the composition and electronic states of the surface region of a sample can be studied. According to the type of the exciting radiation, photoelectron spectroscopy is subdivided into ultraviolet photoelectron spectroscopy (UPS) with the exciting light source in the ultraviolet range, and X-ray photoelectron spectroscopy using X-rays as radiation source. Since the energy of the ultraviolet light source in UPS is normally between 10 and 40 eV, it is suitable to determine the positions and shape of the HOMO of a molecule or molecular solids by analyzing escaped valence electrons bound in the outermost levels (the valence levels). In contrast, XPS is very sensitive to changes of the chemical bonds of molecular atoms due to the so-called chemical shift of the core level orbitals by studying core electrons escaped from the inner shells of atoms.

Photoelectron spectroscopy is based on Einstein's photoelectric effect: A photon can ionize an electron from a molecule if the photon has an energy greater than the binding energy of the electron in the molecule. Any photon energy in excess of that needed for ionization is carried by the outgoing electron in the form of kinetic energy. In general, the kinetic energy E_{kin} of a photoelectron is given by:

$$E_{kin} = h\nu - (E_A - E_B), \quad (3.3)$$

where $h\nu$ is the energy of the exciting radiation, and E_A and E_B denote the energies of the system after and before the ionization.

From the UPS spectra of an organic material, the ionization potential (IP) of this material can be easily calculated from the width of the spectrum by:

$$IP = h\nu - (E_{kin}^{max} - E_{kin}^{min}), \quad (3.4)$$

where E_{kin}^{max} and E_{kin}^{min} is determined by the HOMO cutoff energy and high binding energy cutoff (HBEC), respectively. When interface properties of metal/organic or organic/organic interfaces are investigated, possible interface dipoles and level binding at the interfaces can be determined by the shift of HBEC energy during the growth of the organic overlayers.

Because of the high energy of the exciting radiation in XPS measurements, the positions of core level peaks of the elements contained in the molecules can be investigated. If the above discussed level binding occurs, the position of these peaks should shift correspondingly. In addition, it is also possible to retrieve information regarding possible chemical reactions or metal diffusion at interfaces.

Being a well known tool for interface investigations, the reader is referred to Reference 134 and 135 for detailed information about the spectrum evaluation.

3.3.3 Efficiency measurements in integrating sphere

An integrating sphere is an optical device for various purposes such as measuring the optical flux from an optoelectronic device or measuring scattering losses from a surface. As shown schematically in Fig. 3.15, it consists of a hollow sphere having a diffusely and homogeneously reflecting internal surface with at least two openings (ports) for a light source and a photodetector system. In between the light source and the detector, a baffle is used to prevent direct illumination of the detector by the light source. As a relative measuring method, a calibration of the sphere with a standard lamp is required before measurements of test samples, which unfortunately introduces measurement errors caused by different self-absorption of the test and standard devices. An auxiliary lamp can be mounted permanently inside the sphere to compensate for this substitution error.

The basic principle of operation is the following: The emitted light undergoes multiple diffuse reflections before it reaches the detector, as shown schematically by the red arrow in Fig. 3.15. As a consequence, the light flux becomes very uniform at the detector, and nearly independent of the spatial and polarization properties of the emitted light. The detected intensity depends basically only on the total radiant power from the light source measured, given by:

$$E_{total} = \frac{\Phi_0}{4\pi R^2} \times \frac{\rho}{1 - \rho}, \quad (3.5)$$

where Φ_0 is the total light flux of the device, R the radius of the integrating sphere, and ρ the reflectivity of the inner surface. However, the detected intensity is only a relative value. To determine the absolute output of luminous flux (L_p) of a device, the photodetector signal has to be calibrated first by a standard lamp of known luminous flux. The power efficiency of the device can then be calculated by Eq. 2.14 (light output divided by input power) and the quantum efficiency can be determined by:

$$\eta_{ext} = \frac{\int \frac{L(\lambda)}{683 V(\lambda) hc / \lambda} d\lambda}{I / e}, \quad (3.6)$$

where $L(\lambda)$ is the spectral luminous flux. $V(\lambda)$ is the spectral luminous efficiency function, h is Planck's constant and c is the velocity of light in vacuum.

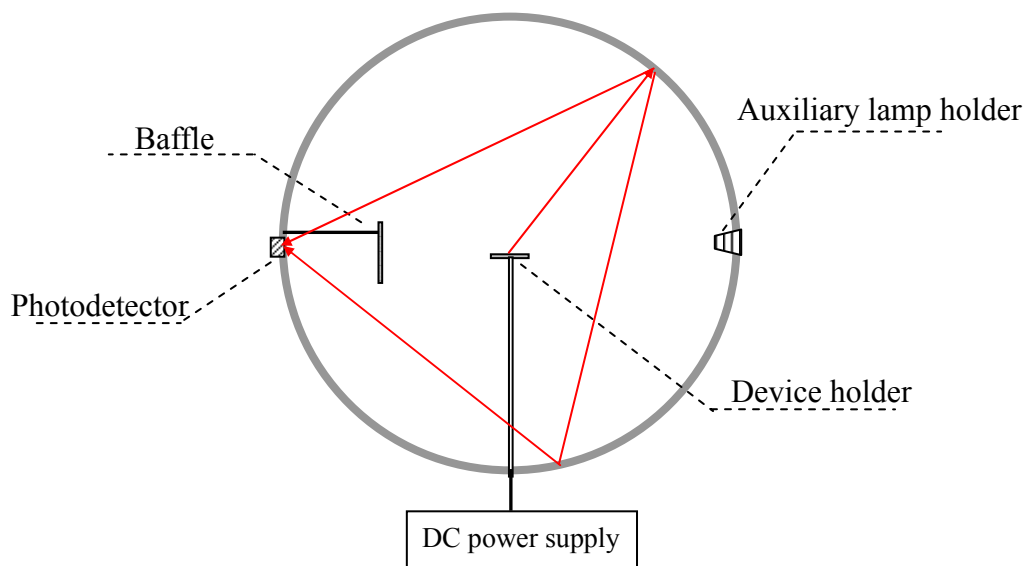


Fig. 3.15. Schematic illustration of an integrating sphere.

Chapter 4

Top-emitting OLEDs with non-inverted structure

In this Chapter, conventional top-emitting OLEDs, having the bottom electrode as anode and top electrode as cathode, will be discussed. Electrical properties of devices with different anode, cathode, and transport layer thickness will be compared first: It will be demonstrated that with electrically doped charge carrier transport layers, the electrical device structure is almost independent on the electrical properties of electrodes. This eases the device optimization by just considering their impact on the optical device structure. Then, it will be shown from simulations and experiments that the position of the emission zone and the reflectivity of the bottom anode are crucial for light outcoupling of a top-emitting device. Based on these investigations, high efficiency top-emitting devices will be demonstrated, which use Ag as both bottom anode and top cathode. After the device optimization, the outcoupling enhancement of top-emitting devices will be shown in detail. Finally, the influence of the optical device structure on the spontaneous emission of several triplet emitters will be investigated together with its influence on device efficiency.

4.1 Introduction

Because of the advantages of top-emitting OLEDs compared to bottom-emitting devices for applications in high resolution active matrix displays (as discussed in Chapter 1), OLEDs with a top-emitting architecture are receiving increasing interest. Since an OLED normally consists of several interfaces including organic/organic, metal/organic and organic/metal interfaces, the simplest way to design a top-emitting OLED is to just replicate the basic device structure of a conventional bottom-emitting device in such a way that the sequence of organic layers is unchanged while the ITO bottom anode and the metallic reflective top cathode of a conventional bottom-emitting device are replaced by a highly reflective bottom anode and

(semi)transparent top cathode so that light generated is coupled out from the top cathode, as shown in Fig. 4.1. Therefore, the bottom and top electrodes in such a top-emitting device, which is also called non-inverted device, are still acting as anode and cathode, respectively. In such devices, only the interfaces between HTL/anode and cathode/ETL are changed, whereas the layer sequence is basically untouched (see Fig. 4.1). This makes the device optimization comparatively easy, since the experience from bottom-emitting OLEDs can be used

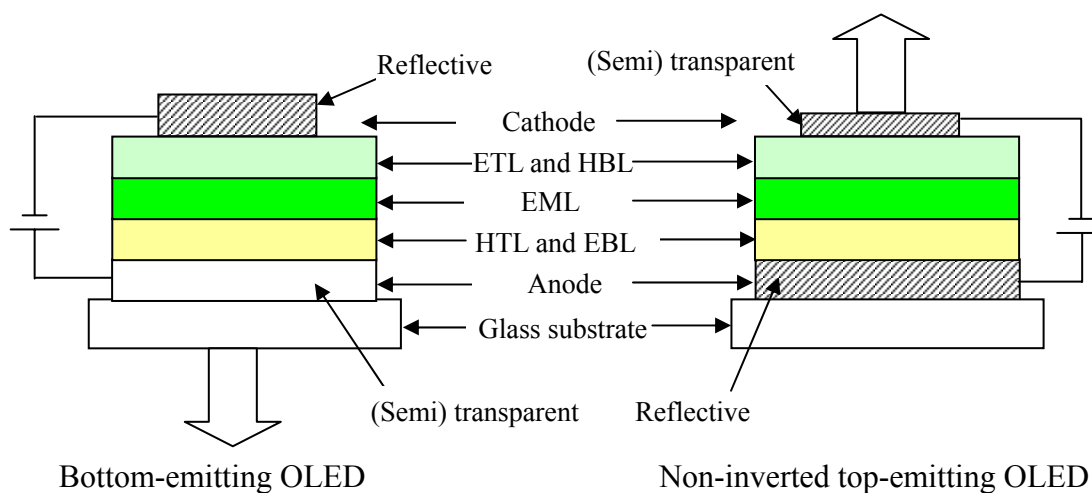


Fig. 4.1. Schematic illustration of a bottom-emitting (left) and non-inverted top-emitting OLED (right)ⁱ.

4.2 Optimization of the device structure

As discussed in Chapter 2, the device performance of a top-emitting OLED is determined by both the electrical and optical device structure. To have high efficiency top-emitting devices, it is required to optimize both the electrical and optical properties of devices simultaneously. It will be demonstrated here that with electrically doped charge carrier transport layers, the electrical and optical device structure of top-emitting OLEDs can be optimized at the same time.

4.2.1 Influence of electrode materials on the electrical device properties

First, the influence of the contact materials on the electrical device properties was investigated without considering their impact on the optical device structure. Blue top-emitting OLEDs with Spiro-Anthracene as emitter were used as model system (device structure in Fig. 4.2). NHT5 doped with NDP2 (4 mol%) was used as p-type hole transport layer and co-evaporated Bphen and pure Cs was used as n-type electron

ⁱ One should note that for a top-emission device, opaque substrates are often used instead of glass.

transport layer. Both transport layers showed a high conductivity around 10^{-5} S/cm.

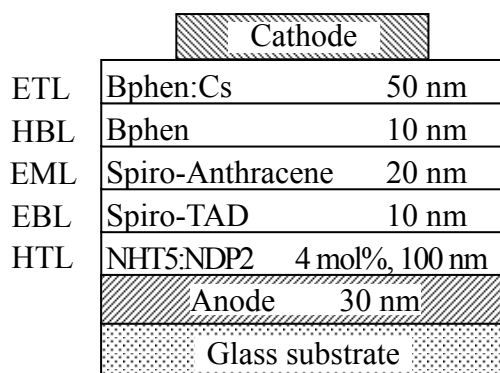


Fig. 4.2. The basic device structure of blue top-emitting OLEDs used to study the influence of electrode materials.

4.2.1.1 Different anodes

A series of devices having the same top cathode but different bottom anodes was investigated first. In all cases, a cathode consisting of 1 nm Al coated by 14 nm Au (represented by Al1Au14) was used to obtain a high transmittance in the full visible range, yet retaining high conductivity and good electron injection. The work functions of the anode materials are summarized in Table 1. In addition, devices with precoated and as-deposited Cr and ITO bottom anodes were compared as well. The surfaces of the precoated anodes were cleaned in oxygen plasma before they were put into use. It is thus expected that the precoated anodes have different surface properties from the as-deposited anodes because of the surface treatment, which may lead to different hole injection ability [136].

Elements	Work function (eV)
Ag	~ 4.3
Cr	~ 4.5
ITO	4.2-4.5
ITO (with O ₂ plasma)	~ 4.75
Au	~ 5.1

Table 1. Work functions of the anode materials used [51, 136].

Current density-voltage (J-V) characteristics of these devices are compared in Fig. 4.3. All samples show nearly the same onset voltage around 2.5 eV, indicating a similar charge carrier injection barrier in all devices although they have different anodes with significantly different work function. After the onset, the J-V curves of the devices are slightly different. This, however, does not correlate with the work functions of the anodes since the device using Cr (as deposited) as anode has better electrical properties than the device based on Au. In addition, the high leakage currents in the samples with home-made (as-deposited) anode are mainly attributed to

the large roughness of these bottom anodes.

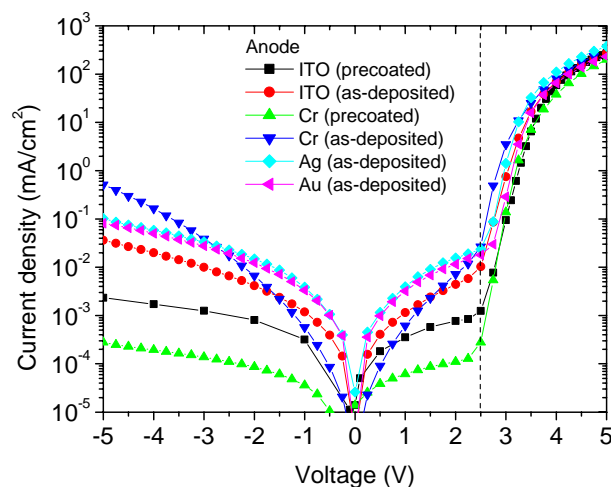


Fig. 4.3. J-V characteristics of top-emitting OLEDs with different anodes.

4.2.1.2 Different cathodes

Next, the influence of the cathode materials on the electrical device properties was investigated. For this, different cathode structures were tested: Al 1 nm/Au 14 nm (Al1Au14), Ag 15 nm (Ag15), and ITO 5 nm/Ag 15 nm/ITO (35 nm) (ITO5Ag15ITO35). In all cases, precoated Cr was used as anode. As demonstrated in Fig. 4.4, where the J-V characteristics of these three devices are compared, the work function of the cathode has almost no influence on the electrical device properties, which is similar to the anode variation case.

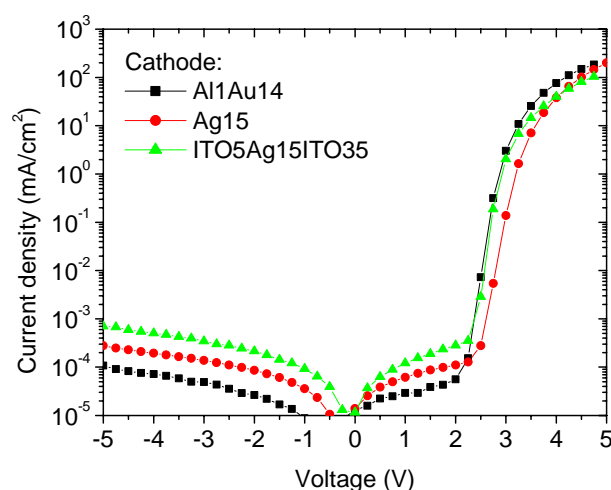


Fig. 4.4. J-V characteristics of top-emitting OLEDs with different cathodes.

In both cases shown above, the J-V curves of all devices show a step increase after the onset, indicating efficient carrier injection from both electrodes. Moreover, although all the devices discussed above have slightly different J-V curves, the

difference does not correlate with the work functions of the anodes. This confirms that the work function of the electrodes is not crucial in OLEDs with doped transport layers, which is consistent with the tunneling mechanism of charge carriers from the electrodes into the electrically doped charge carrier transport layers (as discussed in Chapter 2) [32, 107].

4.2.2 Influence of organic layer thickness on the electrical device properties

Top-emitting OLEDs with identical device structure, but different hole transport layer thickness were compared to study the influence of organic layer thickness on the electrical device performance. All devices had the following basic structure:

Cathode	Al/Au 1/14 nm	
ETL	Bphen:Cs	50 nm
HBL	Bphen	10 nm
EML	Spiro-Anthracene	20 nm
EBL	Spiro-TAD	10 nm
HTL	NHT5:NDP2	varied
Anode	Al/Au 30/4 nm	
	Glass substrate	

Fig. 4.5. The basic device structure of blue top-emitting OLEDs with varied HTL thickness.

All anodes were fabricated in the metal chamber and the thickness of the p-HTL (NHT5:NDP2) was varied as follows: 35, 45, 60, 75, and 100 nm. In addition, a reference sample with the same device structure but using precoated Cr as anode was fabricated as well. The sample has a HTL thickness of 35 nm.

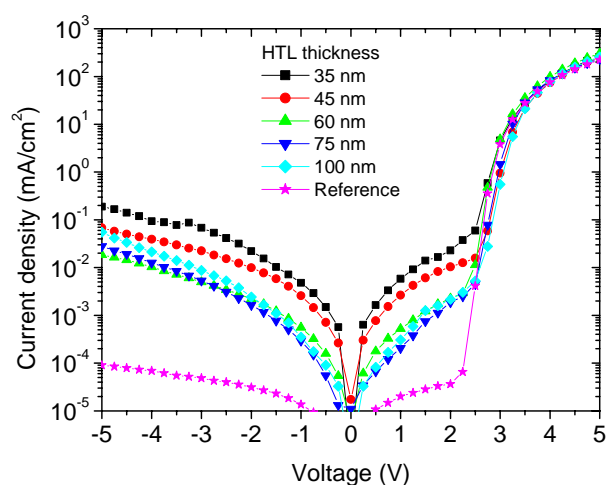


Fig. 4.6. J-V characteristics of top-emitting OLEDs with different HTL thickness. A reference sample using a precoated Cr anode with 35 nm HTL is shown for comparison.

The J-V curves of these devices are compared in Fig. 4.6. It is clearly shown that in forward bias, they have nearly the same J-V characteristics after the current onset, although all devices have very different HTL thickness. Before onset, the J-V curves are quite different, which is due to the different leakage currents (shunt currents) of the devices. It is known that the leakage current of an OLED is directly related to the peak-to-valley roughness of its bottom contact [137]. The surface roughness of a sample having identical structure as the anode was thus measured using atomic force microscopy (AFM). A couple of spikes that have a height larger than 60 nm were observed. It is these high spikes that lead to the high shunt currents especially when the HTL is thinner than 60 nm. With thicker HTL, the spikes may be covered completely by the HTL and the influence of these spikes on the leakage currents can be reduced. Therefore, one can expect that the devices show similar low leakage currents when the bottom anode is smooth enough. This is confirmed by J-V characteristics of a reference sample based on a precoated Cr anode, which has a relatively smooth surface with a spike height around 24 nm (determined by AFM measurements): This reference sample shows much lower leakage currents than all other devices based on the as-deposited anodes, although its HTL is as thin as 35 nm. Therefore, the difference in J-V curves before onset is mainly due to the high roughness of the as-deposited anode. All this indicates that because of the doped charge carrier transport layers having high conductivity around 10^{-5} S/cm, the thickness of the carrier transport layers has little influence on the electrical device properties.

It is obvious from these results that when using doped charge carrier transport layers, the electrical properties of the electrodes and the transport layer thickness have little influence on the electrical device properties. This may ease the optimization of top-emitting OLEDs by selecting electrode materials mainly according to their optical properties and optimizing the transport layer thickness only from the optical point of view.

4.2.3 Influence of the reflectivity of the bottom contact on the device efficiency

All top-emitting OLEDs comprising two metal electrodes (the bottom electrode is reflective while the top cathode is semitransparent) show strong microcavity effects. The emission of the devices can thus be modeled as the emission of dipoles in a Fabry-Perot cavity and may be quantified by calculations using multiple-beam summation from an internal source. As a result, the electroluminescence intensity emitted in perpendicular direction of a top-emitting OLED can be described roughly by [94]:

$$I(\lambda) \propto \frac{\left| 1 + \sqrt{R_B} \exp[j(4\pi nd / \lambda + \varphi_B)] \right|^2}{\left| 1 - \sqrt{R_B R_T} \exp[j(4\pi nL / \lambda + \varphi_B + \varphi_T)] \right|^2} T_T(\lambda), \quad (4.1)$$

where T_T is the transmittance of top electrode; R_B , R_T are the reflectance of bottom and top contact, respectively; n is the refractive index of the organics sandwiched in between; d is the distance of the emission dipole from the reflective bottom anode and L is the total thickness of the organics; φ_B and φ_T are phase changes at the bottom and top electrode, respectively. It is clearly seen from Eq. 4.1 that the reflectivity of the bottom electrode plays a crucial role on the device efficiency, which is confirmed by the experimental results shown in Fig. 4.7b.

In Fig. 4.7, the electrical characteristics and the current efficiencies of a set of green top-emitting devices with the same organic stack and top electrode, but employing anodes with different reflectance are compared. In the plot, the device based on a Cr substrate is used as the benchmark with its current efficiency (at a current density of 10 mA/cm²) and anode reflectivity being normalized to 1. As predicted by Eq. 4.1, the efficiency of the devices increases more rapidly than the reflectivity of the bottom anodes.

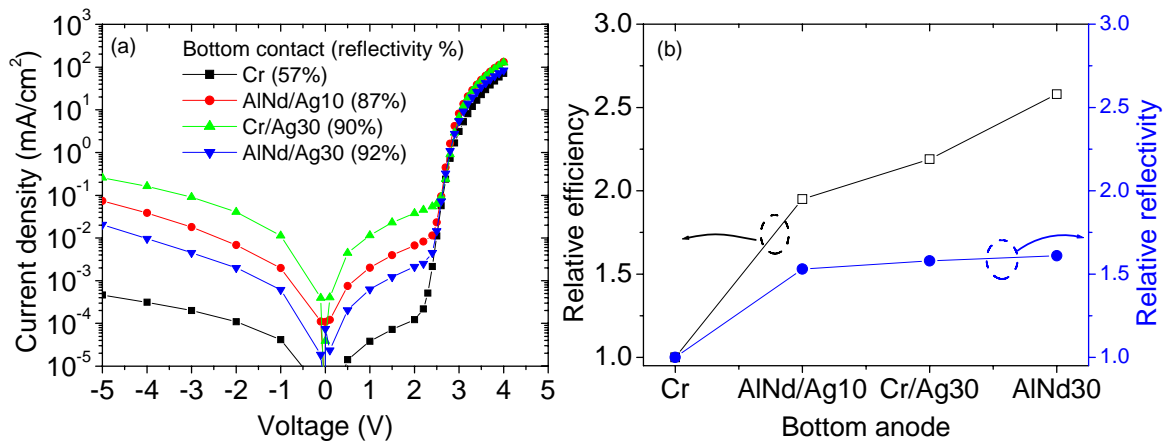


Fig. 4.7. (a) J-V characteristics and (b) relative current efficiencies of top-emitting OLEDs with different anodes to the device with Cr as the anode.

4.2.4 Influence of organic layer thickness on the device efficiency

With organic layers sandwiched in between two metal electrodes, the top-emitting OLEDs investigated in this study show strong microcavity effects. Therefore, to obtain maximum efficiency, it is desirable to have emission at the antinode position so that constructive interference between forward emitted and reflected waves can take place, as also indicated in Eq. 4.1. Hence, the location of emitters in the device is

crucial for the device efficiency. This may be adjusted by changing the thickness of HTL and/or ETL as demonstrated in Fig. 4.8: Fig 4.8 shows the calculated dependence of the vertical luminescence intensity on the thickness of HTL and ETL thickness of a device with the following structure:

Glass substrate/ Ag (>80 nm)/ p-HTL (Y nm)/ EBL (10 nm)/ EML (20 nm)/ HBL (10 nm) /n-ETL (X nm)/ Ag (15 nm)

The calculation was made using software called Emissive Thin Film Optics Simulator (ETFOS). In this software, a radiative species is modeled as emissive dipole. The emission is assumed to be originating from radiative dipoles embedded in a multilayer thin film stack and is solved numerically in one dimension using a transfer matrix method as a function of the viewing angle [138]. For the calculation, the photoluminescence spectrum of the green emitter Ir(ppy)₃ was used and the emission zone was assumed to be located at the center of the EML.

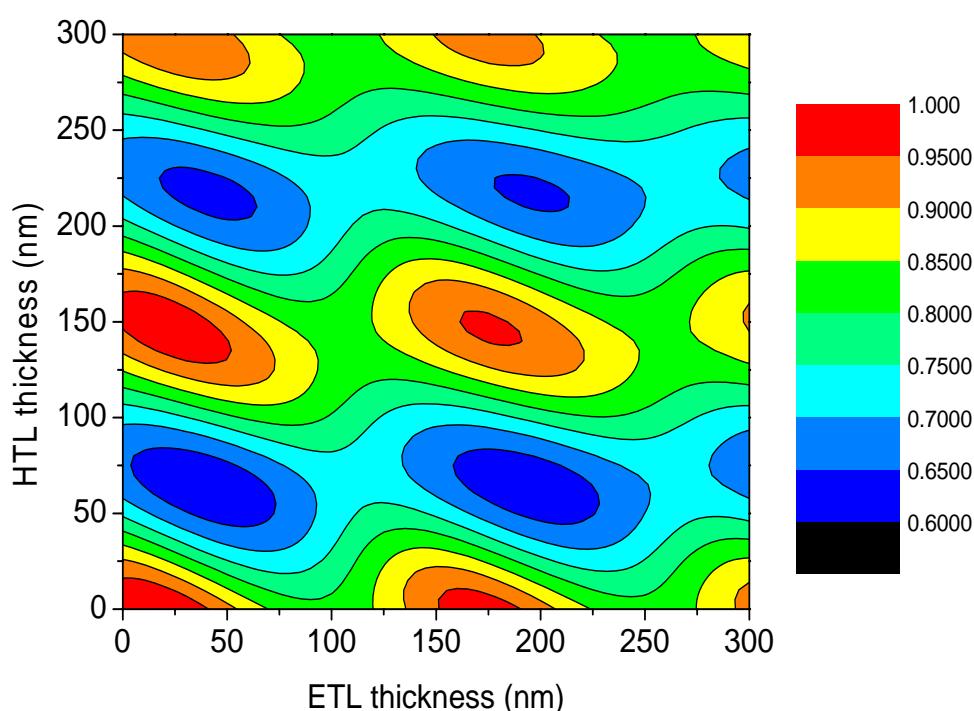


Fig. 4.8. Thin film optical simulation of the device luminescence intensity (vertical) with different HTL and ETL thickness using the software ETFOS [138], which shows a periodic dependence of luminescence on the HTL and ETL thickness of a top-emitting OLED.

4.3 Highly efficient top-emitting OLEDs

4.3.1 High efficiency top-emitting OLEDs employing Ag as both bottom and top electrodes

As demonstrated above, the electrical properties of the electrodes and the thickness of the charge carrier transport layers have little influence on the electrical properties of the devices when electrically doped p- and n-type organic layers are used as HTL and ETL. This considerably eases the optimization procedure of top-emitting OLEDs: Only the optical device structure has to be optimized to achieve optimum efficiency.

Because Ag has one of the highest reflectivities among all metals, it was used in this study as highly reflective bottom anode (details in Session 4.2.3). Furthermore, Ag is also an ideal metal for being used as top contact due to its low absorption in the visible spectral region and its highest conductivity among all metals. In this study, 15nm Ag is used as the top cathode, which is a compromise between electrical and optical properties. Fig. 4.9 shows its reflectance, transmittance, and absorbance as function of wavelength.

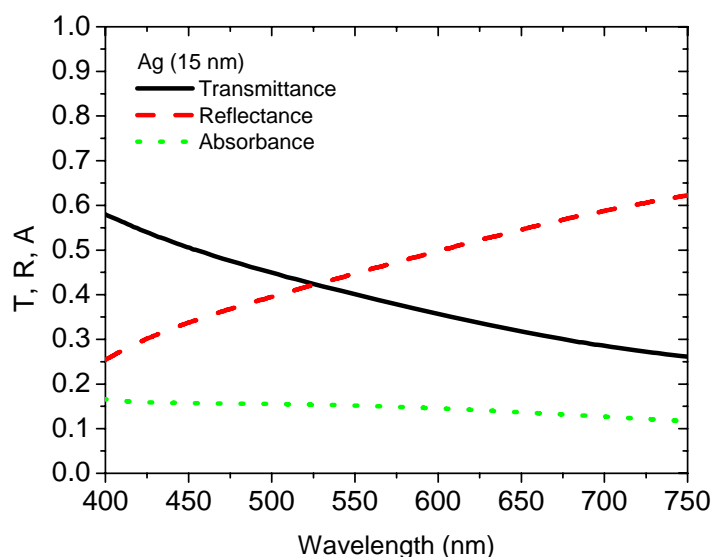


Fig. 4.9. Transmittance (T), reflectance (R), and absorbance (A) of 15 nm Ag as seen from inside the organic layer.

In the following, we will discuss a top-emitting OLED with an optimized device structure, which is modeled and compared to a series of experiments. For comparison, a corresponding bottom-emitting OLED with a similar structure as reported

previously [109] is used as reference, which has the following optimized device structure:

Cathode	Ag 15 nm	Al >100 nm
ETL	Bphen:Cs 25 nm	Bphen:Cs 25 nm
HBL	Bphen 10 nm	Bphen 10 nm
EML2	TPBI:Ir(ppy) ₃ 8 wt%, 10 nm	TPBI:Ir(ppy) ₃ 8 wt%, 10 nm
EML1	TCTA:Ir(ppy) ₃ 8 wt%, 5 nm	TCTA:Ir(ppy) ₃ 8 wt%, 5 nm
EBL	Spiro-TAD 10 nm	Spiro-TAD 10 nm
HTL	MeO-TPD:F ₄ -TCNQ 4 mol%, 45 nm	MeO-TPD:F ₄ -TCNQ 4 mol%, 125 nm
Anode	AlInD/Ag >100/30 nm	ITO 132 nm
	Glass substrate	Glass substrate

Top-emitting OLED Bottom-emitting OLED

Fig. 4.10. Device structure of an optimized (left) top-emitting and (right) bottom-emitting OLEDs.

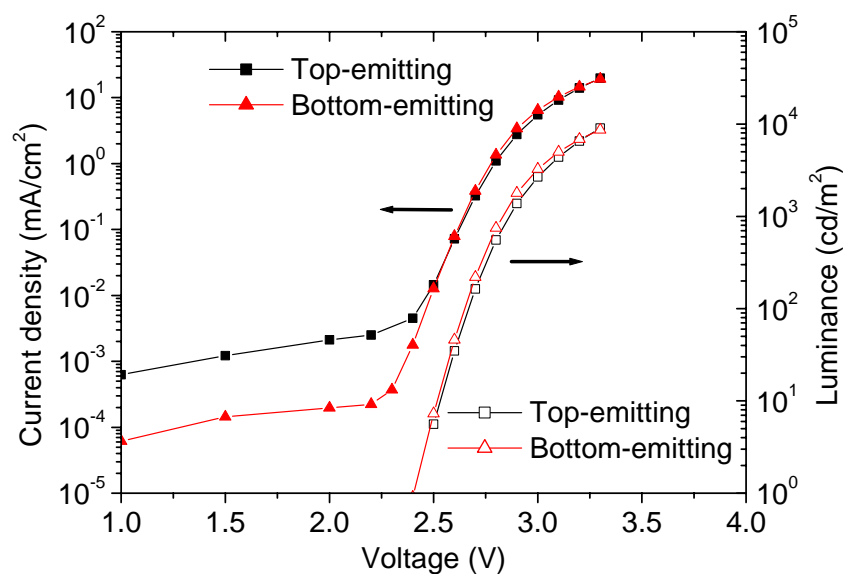


Fig. 4.11. Comparison of current density-voltage (solid) and luminance-voltage (open) characteristics of an optimized top-emitting OLED (square) and bottom-emitting OLED (triangle) with the same organic layer structure.

The J-L-V characteristics of the top- and bottom-emitting OLED are compared in Fig. 4.11. Both devices show comparable electrical properties. The J-L-V curves of the two devices show a steep increase after the onset, which indicates an efficient carrier injection from both electrodes caused by the *p-i-n* device structure. This confirms once more that the work function of the electrodes is not crucial in OLEDs

with doped transport layers since the electrodes in the top-emitting OLED have much larger energy barriers at the injecting interfaces than those of the bottom-emitting OLEDs.

Assuming Lambertian emission in both devices, the calculated external quantum efficiencies of these two devices are also comparable, which is especially true in the high brightness region, as shown in Fig. 4.12. The somewhat lower efficiency of the top-emitting OLED compared to the bottom-emitting device at low brightness is mainly due to the higher leakage current caused by the roughness of the metal bottom electrode of the top-emitting OLED. In the inset of Fig. 4.12, the electroluminescence spectra of these two devices are compared with the photoluminescence spectrum of the emitter. Due to stronger microcavity effects in the top-emitting device, the emission at the photoluminescence peak wavelength is suppressed while the emission at the wavelength of the photoluminescence shoulder is enhanced.

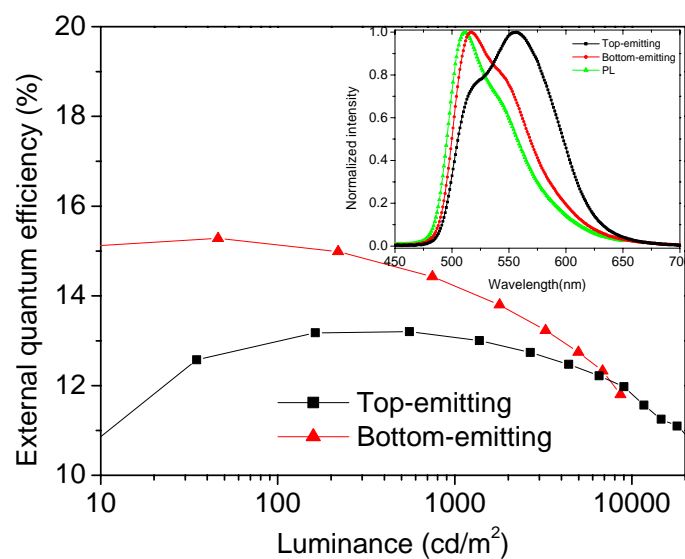


Fig. 4.12. External quantum efficiencies of the top- and bottom-emitting OLEDs. In the inset, electroluminescence spectra of the two devices and the photoluminescence (PL) spectrum of the emitter are shown.

4.3.2 Efficiency improvement by an organic capping layer

Unfortunately, a large portion of the generated light is still trapped and absorbed eventually in the device (see Fig. 2.10) because light is outcoupled out from a dense medium ($n \sim 1.7$) into a less dense medium (air). For bottom-emitting OLEDs, several different methods can be used to extract this trapped light (details in Section 2.2.3.2).

However, the outcoupling enhancement methods used in bottom-emitting OLEDs are not directly applicable to top-emitting OLEDs, as the outcoupled light is going through the top contact instead of the bottom substrate

Recently, a dielectric layer on top of the thin top metal contact has been introduced to improve the device efficiency by changing the transmittance of the top contact, an option which is known from thin film optics [19, 20]. It is shown that this transmittance-tuning effect depends not only on the layer thickness, but also on the refractive index of the dielectric layer, as demonstrated in Fig. 4.13.

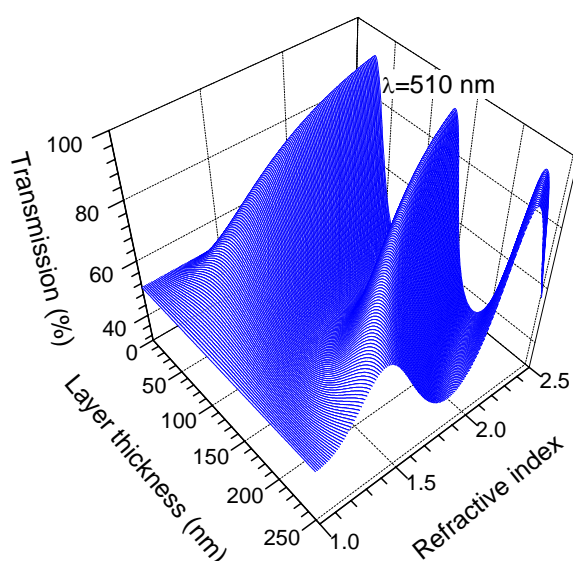


Fig. 4.13. Calculated transmittance of a top contact stack consisting of 15 nm Ag and a capping layer at the wavelength of 510 nm as functions of capping layer thickness and refractive index^j.

The method was also used in this study by introducing an additional dielectric/semiconductor layer, the so-called capping layer, on top of the cathode of top-emitting OLEDs. Instead of other high refractive index materials such as TiO₂ and ZnSe etc., an organic layer of MeO-TPD was used as capping layer, which can be easily deposited by thermal evaporation. A set of devices was investigated in detail: All diodes were prepared in the same run having an identical structure but different MeO-TPD capping layer thickness. The MeO-TPD capping layer thickness was varied from 0 to 200 nm.

^j The calculation was made by Prof. Vadim Lyssenko of the IAPP using a transfer matrix method.

4.3.2.1 Influence of the capping layer thickness on the performance of top-emitting OLEDs in perpendicular direction

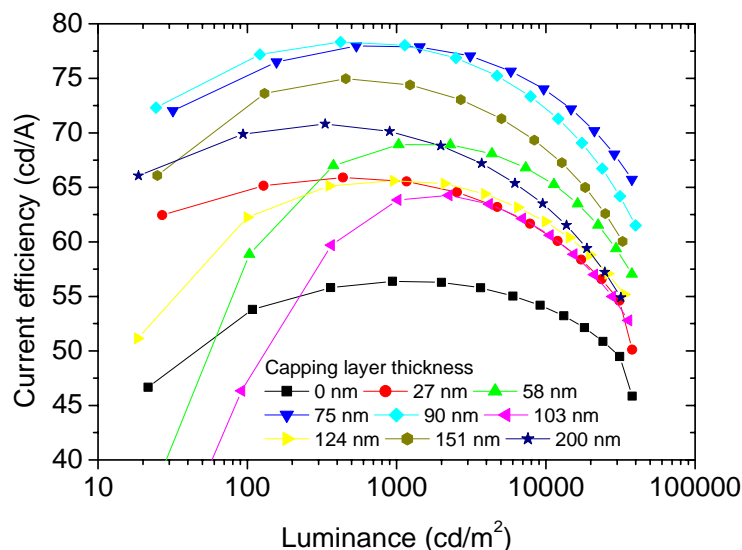


Fig. 4.14. Current efficiency vs. luminance of the top-emitting OLEDs with a capping layer thickness of 0, 27, 58, 75, 90, 103, 124, 151, and 200 nm, respectively.

Fig. 4.14 shows the current efficiencies of top-emitting OLEDs with different capping layer thickness as a function of brightness, measured in vertical direction. It is clearly seen that the capping layer has a significant influence on the efficiency of the top-emitting device. The device without capping layer has a high current efficiency of 56 cd/A at 1000 cd/m². As expected, with the capping layer applied, the current efficiencies of the devices can be improved dramatically, showing a maximum enhancement by a factor of 1.38 at a capping layer thickness between 75 nm and 90 nm, with a peak efficiency of 78 cd/A at 1000 cd/m². As demonstrated already, it can be seen from Fig. 4.15 that the performance of the devices shows no direct correlation with the transmittance of the top contact: the efficiency variation is not systematic, although the transmittance of the top contact shows an oscillatory dependence on the capping layer thickness. The latter is expected from thin film optics. It is clearly seen that the highest efficiency is achieved at thicknesses where the top contact has almost the lowest absorption, which agrees with the result from other groups although they used a completely different device structure [87, 102]. Obviously, this enhancement is not simply dependent on the transmittance of the top contact, but on the complex interference effects within the device.

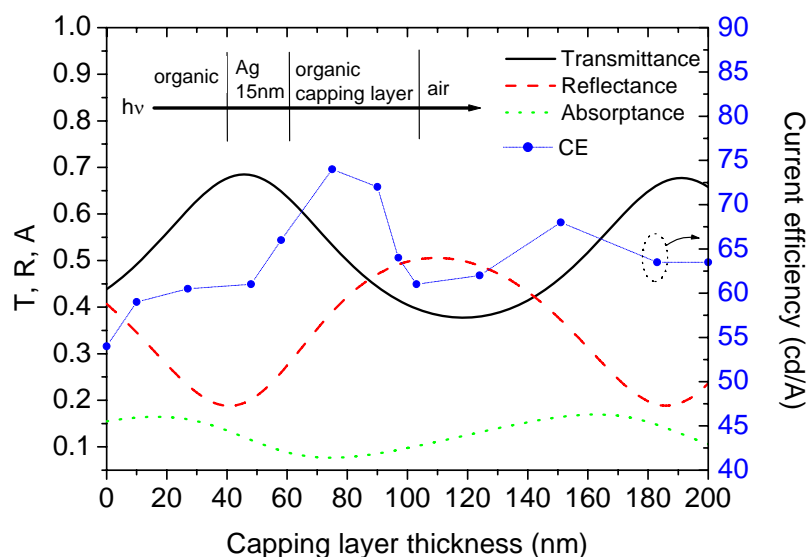


Fig. 4.15. Calculated transmittance (T), reflectance (R), and absorbance (A) of the top contact stack (shown in the inset) at a wavelength of 510 nm depending on the capping layer thickness using a transfer matrix method^k. The thickness of the organic layer is assumed to be infinite. The scattered dots represent the current efficiency of the top-emitting OLEDs at 10000 cd/m².

However, the electroluminescence spectra of these devices exhibit a strikingly large dependence on the transmittance of the top contact, as depicted in Fig. 4.15 and Fig. 4.16. The electroluminescence spectrum of the uncapped device is already changed and red-shifted compared to the photoluminescence spectrum of the emitter due to the relatively strong microcavity effect, which leads to a narrowed spectrum with enhanced light emission at the resonance wavelength. As a result, it exhibits the most enhanced light emission around 540 nm (where the photoluminescence spectrum has only a small shoulder) with suppressed emission at the photoluminescence peak wavelength. By increasing the capping layer thickness up to 200 nm, the position of the peak and shoulder remain almost unchanged (with the exception of devices with capping layer thickness of 97 and 103 nm), but the relative intensity at the shoulder changes periodically, leading to a periodic change of the full width at half maximum (FWHM) of the spectra. This coincides with the oscillatory dependence of the transmittance of the top contact with the capping layer thickness (see Fig. 4.15). This phenomenon can be explained as follows: It is known that the cavity finesse depends on the reflectivity of both contacts, indicating that the magnitude of microcavity effects in top-emitting OLEDs changes with the transmittance of the top contact, which shows a periodic dependence on the capping layer thickness. The influence of the emitter is more pronounced with the decrease of cavity finesse. Consequently, light emission at the photoluminescence peak wavelength is enhanced or reduced

^k The calculation was made by Dr. Thomas Stübinger of Novalad AG using a transfer matrix method.

periodically with increasing capping layer thickness so that the FWHM changes concomitantly. As expected, at a capping layer thickness of 200 nm, where the top contact is most transparent, indicating the least cavity finesse, the relative intensity at the position of the photoluminescence peak wavelength is the highest, leading to two nearly equivalent peaks. As a result, the electroluminescence spectrum is the broadest among all electroluminescence spectra, and it is even broader than the photoluminescence spectrum. In the opposite case, i.e. at the lowest transmittance of the top contact, corresponding to a capping layer thickness of 124 nm where the cavity finesse is the highest (as indicated by Eq. 2.15), the spectrum is the narrowest as indicated by Eq. 2.18 with a FWHM of only 34 nm.

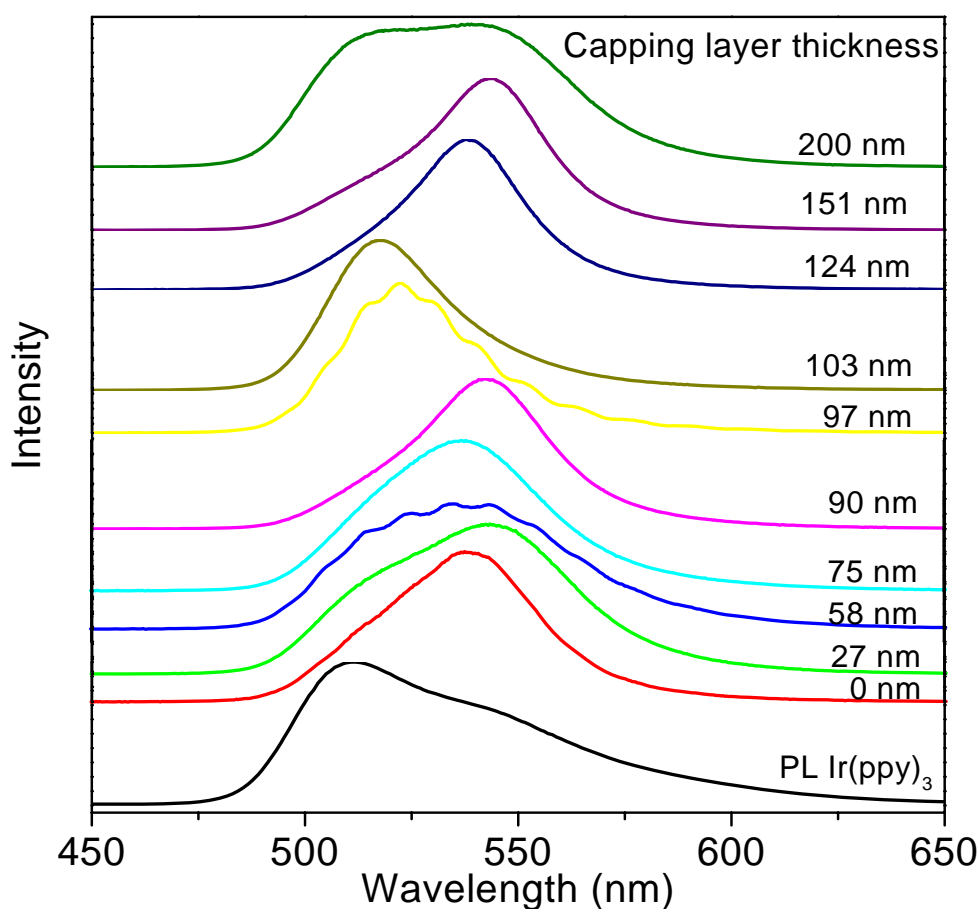


Fig.4.16. Normalized electroluminescence spectra of devices with different capping layer thickness. The photoluminescence (PL) spectrum of Ir(ppy)₃ is shown as a reference.

It is well known that the spontaneous emission from an emitter is normally altered in optical microcavities, which results in an alteration of the radiative decay time of the emitter and correspondingly in a change of the radiative decay rate. Therefore, it is possible that the efficiency enhancement of devices by the capping layer is due to the enhanced intrinsic quantum yield of the emitter because of the enhanced radiative decay of the emitter. However, for the emitter Ir(ppy)₃ with dominant radiative decay (photoluminescence quantum yield nearly 100 % when

doped into a suitable matrix) [139, 140], the intrinsic emission is almost independent of the optical device structure so that the influence of the device structure on the emitter can be neglected [94]. So, the efficiency enhancement by the capping layer could either be attributed to the redistribution of the emitted light (such that only the light emission in forward direction is enhanced with nearly no improvement on the outcoupling efficiency, as demonstrated by another group [100]), or to the improved outcoupling efficiency as a result of the modified optical structure by the capping layer. To find out which is the main reason for the efficiency enhancement, the angular dependence of emission intensity and spectral characteristics on the capping layer thickness are studied.

4.3.2.2 Influence of the capping layer on the overall performance of top-emitting OLEDs

Because of the microcavity effect in top-emitting OLEDs, the emission profile of this kind of device is usually not Lambertian. Fig. 4.17 depicts the electroluminescence intensity (radiance) of the top-emitting OLEDs discussed above, measured at a current density of 6 mA/cm^2 with selected capping layer thicknesses as a function of the viewing angle. All devices are obviously not Lambertian and there is a significant electroluminescence intensity drop at larger viewing angles.

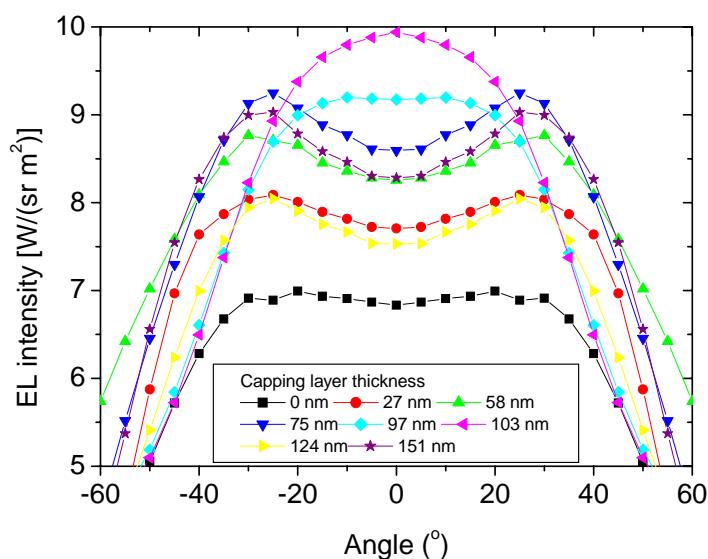


Fig. 4.17. Electroluminescence (EL) intensity (radiation) vs. the observation angle for top-emitting OLEDs with a capping layer thickness of 0, 27, 58, 75, 97, 103, 124, and 151 nm, measured at 6 mA/cm^2 .

For the device without capping layer, the emission intensity shows a slow increase with viewing angle until a maximum is reached at 30° ; then, it drops steadily. With increasing capping layer thickness, this emission increase with viewing angle is more pronounced. However, for the device with the capping layer thickness of 97 nm,

the electroluminescence intensity curve is completely different, showing an enhanced radiation within a small range of viewing angles in forward direction. The most forward-enhanced device is the one with a capping layer thickness of 103 nm, having a maximum enhancement of the radiation by a factor of 1.46 at 0° viewing angle. For devices with even thicker capping layers, the intensity curves return to the former shapes again, showing maximum intensity at a viewing angle of 30°. The spectral characteristics of devices with a typical layer thickness of 0, 75, 103, and 124 nm are presented in Fig 4.18 (a), (b), (c), and (d), respectively. For devices with a capping layer thickness of 0, 75 and 124 nm, there is a relatively strong blue shift of the peak wavelength with increasing viewing angle, exhibiting maximum emission intensity at a viewing angle of 30°, as already shown in Fig. 4.18. As a consequence, the CIE 1931 color coordinates change from (0.28, 0.68) for 0° to (0.22, 0.68) at 65°, which however is hardly detectable by the human eye. A special case is the spectral characteristics of the device with a capping layer of 103 nm, shown in Fig. 4.18 (c). The spectral distribution behaves very differently from the others as it also does in the angular distribution of electroluminescence intensity (see Fig. 4.17). The peak wavelength and the FWHM are almost independent on the viewing angle. However, the fast decrease of the electroluminescence intensity with increasing viewing angle, which has already been observed in Fig. 4.17, is clearly visible. This difference in the angular dependence of the emission profile is caused by a combined effect of the emitter spectrum and the optical structure of the devices, because Ir(ppy)₃ has a broad-band emission spectrum and the microcavity effect in the devices is not very strong. It is known that the resonance wavelength of a microcavity decreases with increasing emission angle, approximately following [141, 142]:

$$\lambda = \lambda_0 \cos(\theta_{int}), \quad (4.2)$$

where λ_0 is the resonance wavelength in the optical axis direction and θ_{int} is the internal emission angle, which is related to the external viewing angle by Snell's law. As the result, the resonance wavelength (corresponding to peak wavelength in electroluminescence spectra) suffers from a strong angular dependence, showing a blue shift with increasing viewing angle. As shown in Fig. 4.18 (a), (b), and (d), which display the angular dependence of spectral characteristics for the devices with capping layer of 0, 75, and 124 nm, the electroluminescence peaks at 0° viewing angle of these devices are roughly at 540 nm, which means almost 30 nm red shift of the resonance wavelength of the devices relative to the photoluminescence peak wavelength of Ir(ppy)₃. With increasing viewing angle, the resonance wavelength decreases and approaches the photoluminescence peak wavelength, so the peak intensity is blue shifted and increases progressively until the maximum electroluminescence intensity

is reached at a viewing angle around 30° due to the combination effect. With further increase of the observation angle, light with even shorter wavelength will be amplified because of the shortening of the cavity resonance wavelength. However, due to the asymmetric photoluminescence spectrum, the emission intensity of $\text{Ir}(\text{ppy})_3$ drops dramatically faster at wavelengths shorter than the peak wavelength, so that the out-coupled electroluminescence intensity rather decreases with larger viewing angle. For the device with a capping layer of 103 nm, the resonance wavelength at 0° is already very close to the photoluminescence peak wavelength of $\text{Ir}(\text{ppy})_3$. Consequently, the electroluminescence intensity at the photoluminescence peak wavelength is strongly enhanced, such that the maximum intensity appears in vertical direction. Although the emission at wavelengths shorter than the photoluminescence peak wavelength would be enhanced, with increasing viewing angle the emission of the emitter (see photoluminescence) is so weak that the electroluminescence intensity decreases dramatically, such that only light close to the photoluminescence peak wavelength is coupled out. Therefore, the device shows an enhanced forward emission with hardly any angular dependence of the emitted color.

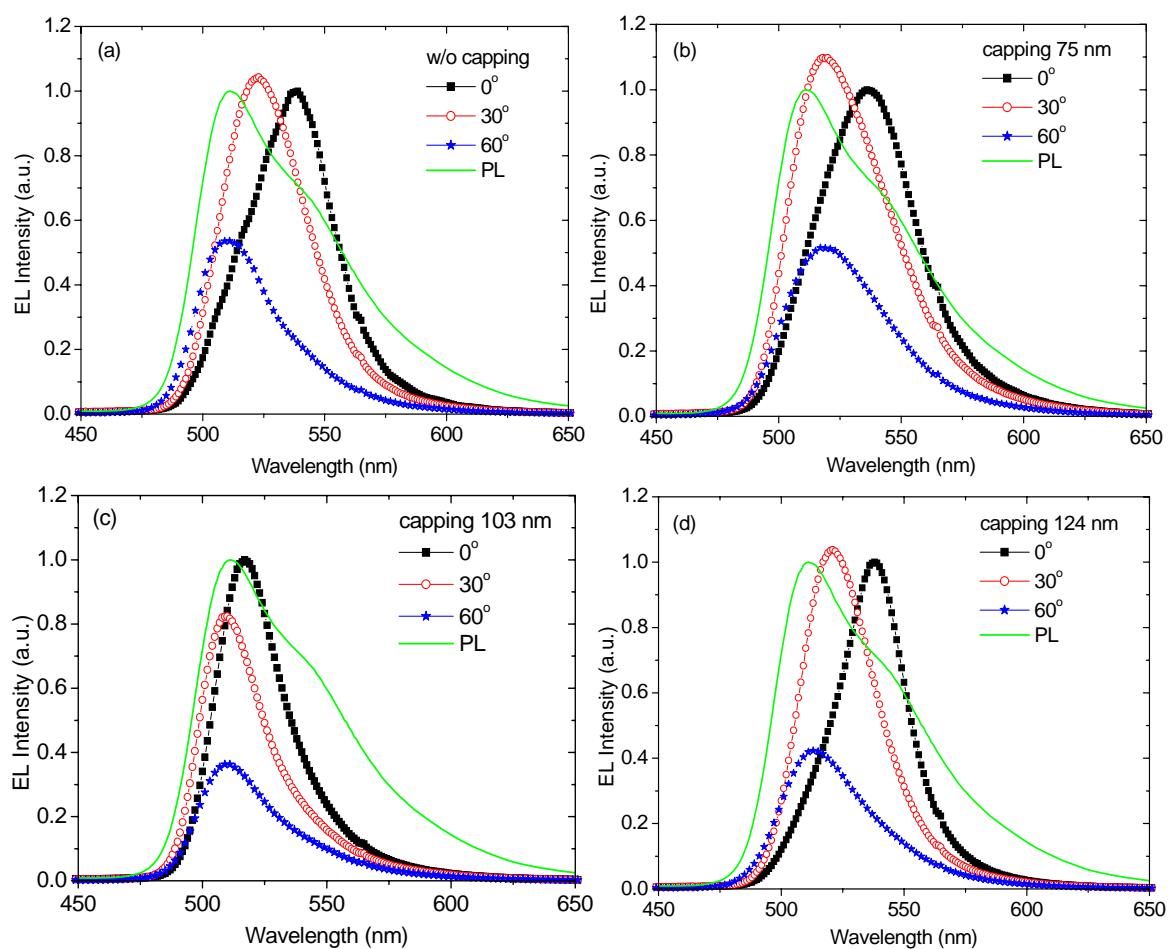


Fig. 4.18. Electroluminescence (EL) spectra at various viewing angles depending on the capping layer thickness: 0 nm (a), 75 nm (b), 103 nm (c) and 124 nm (d). Electroluminescence intensity data are normalized to the case of forward direction.

Table 2 shows the overall performance of these devices. At a capping layer thickness between 75 nm and 90 nm, both the current efficiency in forward direction and the quantum efficiency of the devices are significantly improved by 35 %, resulting in a maximum external quantum efficiency of 17.8 %. It is obvious that this efficiency enhancement can be attributed mainly to the improvement of the outcoupling efficiency due to the changed optical device structure using the capping layer, otherwise the overall performance of would not be enhanced.

Capping layer thickness (nm)	0	27	48	58	75	90	97	103	124	151
Current efficiency (cd/A) for 1000 cd/m ² at 0°	56.4	65.6	63.0	68.8	77.9	78.1	67.5	63.7	65.6	74.6
External quantum efficiency (%) at 1.6 mA/cm ²	13.1	16.1	16.4	16.5	17.7	17.8	14.4	14.9	12.4	16.0

Table 2. Performance data of the devices with selected capping layer thickness.

4.3.3 Highly efficient red, green, and blue top-emitting OLEDs

Extending the capping strategy to red and blue top-emitting OLEDs, highly efficient red and blue devices have been demonstrated as well. These devices contain capping layers of different thickness, optimized for the different wavelengths of the emitted light.

OLEDs	CIE (x, y)	Voltage (V)		CE (cd/A)		EQE (%)
		at 100 cd/m ²	at 1000 cd/m ²	at 100 cd/m ²	at 1000 cd/m ²	at 1000 cd/m ²
Red top 1 (phosphorescent)	(0.66, 0.34)	2.31	2.55	16.7	13.6	10.6
Red top 2 (phosphorescent)	(0.70, 0.30)	2.40	3.02	10.2	9.2	15.3
Red bottom (phosphorescent)	(0.68, 0.31)	2.40	3.00	7.3	6.5	11.3
Green top 1 (phosphorescent)	(0.25, 0.70)	2.64	2.95	86.1	87.7	16.9
Green top 2 (phosphorescent)	(0.33, 0.65)	2.70	3.10	78.0	77.5	20.1
Green bottom (phosphorescent)	(0.30, 0.62)	2.66	2.90	83.0	77.0	19.0
Blue top 1 (fluorescent)	(0.14, 0.11)	3.09	3.61	3.6	3.4	3.7
Blue top 2 (fluorescent)	(0.14, 0.22)	3.01	3.34	8.6	9.0	5.0
Blue bottom (fluorescent)	(0.14, 0.17)	2.90	3.50	7.3	6.8	5.2

Table 3. Overview of red, green and blue top-emitting OLEDs. Corresponding conventional bottom-emitting OLEDs from our group are shown as reference. CE-current efficiency; EQE-external quantum efficiency (EQE of the top-emitting OLEDs were measured in a calibrated integrating sphere).

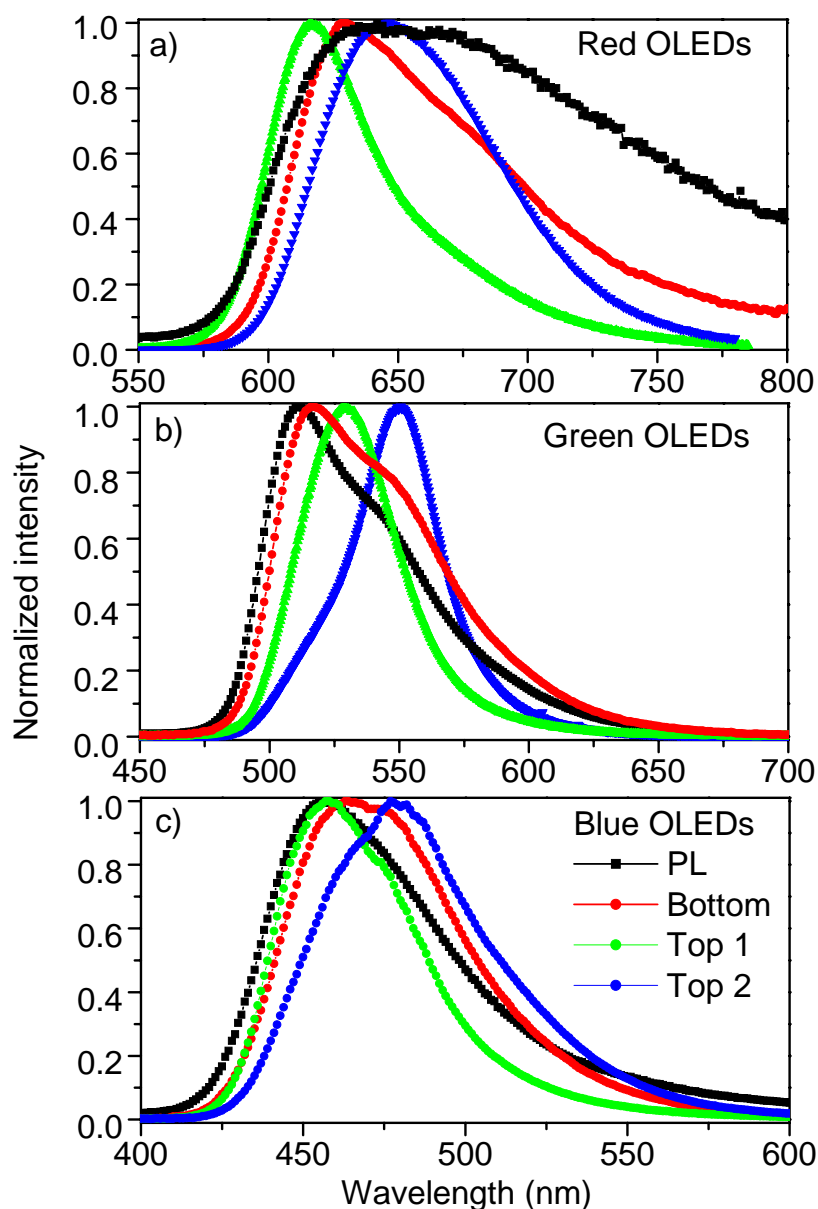


Fig. 4.19. Electroluminescence spectra of a) red, b) green, and c) blue OLEDs discussed in the Table 3. Photoluminescence (PL) spectra of all the emitters are also shown.

As already shown in Chapter 3, organic emitters used in OLEDs are normally broad-bandwidth emitters having asymmetric intrinsic emission with most part of their emission red-shifted to their peak emission (having red-shifted shoulders or tails). It is also known that top-emitting OLEDs have strong microcavity effects with their resonance wavelength blue-shifted with increasing viewing angle. Due to these two facts, the structure of a top-emitting OLED can be optimized either by setting the on-axis cavity resonance wavelength at photoluminescence peak of emitters to get most forward-directed light and hence possible highest on-axis efficiency¹ with slightest color shift or tuning it around 20 nm more to photoluminescence peak to

¹ As a photometric unit, current efficiency is also determined by the photopic response of the eye.

achieve highest external quantum efficiency, but relatively large color shift (as demonstrated in Fig. 4.17 and Fig. 4.18). Table 3 gives an overview over the performance data of red, green and blue top-emitting OLEDs using NDP2 doped NHT5 as p-type hole transport layer. Every kind of OLED has two different optimized device structures to achieve highest current efficiency and external quantum efficiency, respectively. The electroluminescence spectra of all these devices are shown in Fig. 4.19.

4.4 Quantum efficiency enhancement as a result of enhanced intrinsic quantum yield

It is obvious from Table 3 that green and blue top-emitting OLEDs have comparable external quantum efficiency to their bottom-emitting counterparts, which indicates that the outcoupling efficiency of top-emitting OLEDs is not significantly better than that of their bottom-emitting counterparts despite the missing substrate loss in top-emitting devices. This is not yet understood, but in agreement with experimental and simulated results of other groups [77, 86]. Because of this similar outcoupling efficiency of top and bottom-emitting OLEDs, it seems that the external quantum efficiency of an *optimized* top-emitting OLED can not be much higher than in a corresponding *optimized* bottom-emitting device. However, it is not the case for the red top-emitting OLED, which is shown being 35% more efficient than its corresponding bottom-emitting variant in the Table 3. The reason for this discrepancy is investigated in this Section.

4.4.1 Experiment

The well studied phosphorescent metal complexes Ir(piq)₃, Ir(ppy)₃, and FIrpic were used as red, green and blue emitters, respectively. All top-emitting OLEDs had the same structure as their corresponding bottom-emitting counterparts, but a different optimized transport layer thickness (see Table 4). In all the devices, F₄-TCNQ doped MeO-TPD with a doping concentration of 4 mol% is used as p-type HTL, Cs doped Bphen as n-type ETL and MeO-TPD as capping layer.

OLEDs	Anode	HTL	EBL	EML	HBL	ETL	Cathode
Red top	AlNd/Ag >100/30 nm	55 nm	NPD 10 nm	NPD: Ir(piq) ₃ 20 wt%, 20 nm	Bphen 10 nm	40 nm	Ag 15 nm Capping 110 nm
Red bottom	ITO 132 nm	60 nm				45 nm	Ag >100 nm
Green top	AlNd/Ag >100/30 nm	45 nm	Spiro-TAD 10 nm	TCTA: Ir(ppy) ₃ 8 wt%, 5 nm/ TPBI:Ir(ppy) ₃ 8 wt%, 10 nm	Bphen 10 nm	25 nm	Ag 15 nm Capping 90 nm
Green bottom	ITO 132 nm	125 nm				45 nm	Al >100 nm

Blue top	AlNd/Ag >100/30 nm	20 nm	Spiro-TAD 10 nm	TCTA: FIrpic 12 wt%, 20 nm	BAIq ₃ 10 nm	140 nm	Ag 15 nm Capping 60 nm
Blue bottom	ITO 132 nm	60 nm				40 nm	Al >100 nm

Table 4. Device structures of red, green and blue top- and bottom-emitting OLEDs.

External quantum efficiencies of all the devices were measured in a calibrated integrating sphere. Photoluminescence experiments were carried out to determine the triplet exciton lifetime by Sebastian Reineke and Dr. Sergey Bagnich of IAPP. The devices were excited by a short laser pulse (~ 500 ps, 337 nm) from a nitrogen laser MSG-SD (Lasertechnik Berlin GmbH). The emitted photoluminescence signals was collected with a fast PDA 55 photodiode (Thorlabs GmbH, Karlsfeld) and recorded in a multichannel oscilloscope Infinium 54815A (Hewlett Packard, Houston).

4.4.2 Results and discussion

The external quantum efficiencies of all devices measured in the integrating sphere are summarized in Table 5. With optimized structures, all the devices show high efficiency even at high current densities, comparable to the reported high efficiency OLEDs having similar structures [109, 126, 143]. Calculated External quantum efficiencies based on the assumption of a Lambertian distribution of the emission are also shown in the Table.

OLEDs	Red		Green		Blue	
	Top	Bottom	Top	Bottom	Top	Bottom
EQE(%) measured in integrating sphere	12.0	9.8	17.7	17.9	5.0	5.1
EQE(%) calculated (assuming Lambertian light distribution)	16.0	9.9	18.1	18.0	5.8	5.1

Table 5. External quantum efficiency (EQE) of the red, green and blue top- and bottom-emitting OLEDs measured in the integrating sphere at a current density of 15.7 mA/cm², 1.6 mA/cm² and 9.0 mA/cm², respectively (at these current densities, all devices have a brightness around 1000 cd/m²). For comparison, calculated external quantum efficiencies assuming Lambertian distribution of light are shown as well.

In all bottom-emitting OLEDs, the measured external quantum efficiencies closely agree with the calculated values, indicating a Lambertian distribution of all bottom-emitting OLEDs. Consistent with the result of Table 5 and simulations by other groups [78, 87] that top- and bottom-emitting OLEDs have similar outcoupling efficiency, green and blue top-emitting OLEDs show comparably high external

quantum efficiencies with corresponding bottom-emitting devices (17.7% vs 17.9% in green and 5.0% vs 5.1% in blue at current densities of 1.6 and 9.0 mA/cm², respectively). The red top-emitting OLED, however, has a much higher efficiency than the red bottom-emitting OLED (12% vs 9.8% at a current density of 15.7 mA/cm²). Based on the assumption made above that the outcoupling efficiency of a top-emitting OLED is similar to a bottom-emitting device [77, 86], the efficiency difference in the red OLEDs has to be attributed mainly to an increased internal quantum efficiency of the top-emitting device.

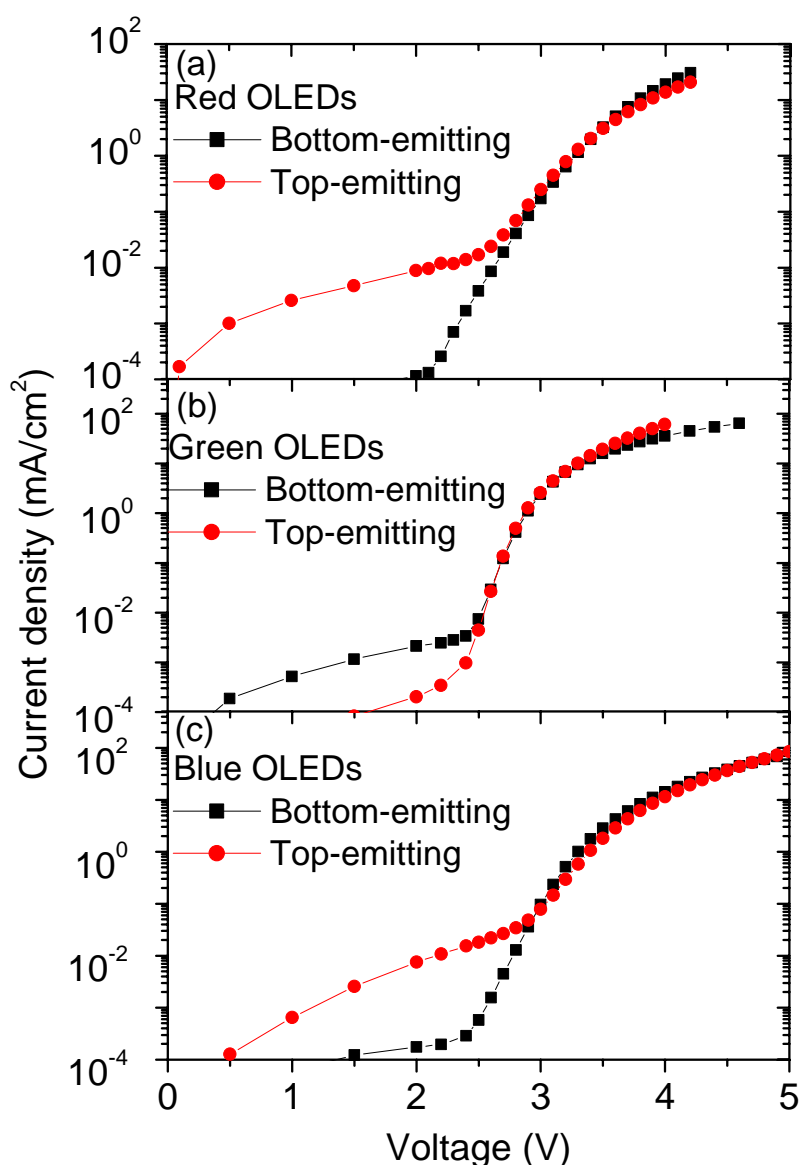


Fig. 4.20. Comparison of current density-voltage curves of (a) red, (b) green, (c) blue bottom- and top-emitting OLEDs.

It is known that the internal quantum efficiency of an OLED is determined both by the electrical properties (charge balance factor, etc.) of the device and by the

intrinsic quantum yield of the emitter. It thus might also be possible that the higher efficiency in the red top-emitting OLED is due to improved electrical properties of the device since the top-emitting OLEDs have different electrodes and different optimized HTL and ETL thickness, compared to those of the equivalent bottom-emitting devices. The current density-voltage (J-V) characteristics of the top- and bottom-emitting OLEDs in red, green and blue are compared in Fig. 4.20. Although they have slightly different electrical structures, all top-emitting OLEDs show electrical properties comparable to their corresponding bottom-emitting counterparts due to the high conductivity of the n- and p-doped charge carrier transport layers. Small deviations in the low voltage range are due to different leakage currents which may be attributed to different substrate surface roughness. Furthermore, the external quantum efficiency is only enhanced in the red, but not in the green and blue top-emitting OLEDs. We thus conclude that the efficiency enhancement in the red top-emitting OLED can be attributed exclusively to the improved intrinsic quantum yield of the emitter.

The optical structures of top and bottom-emitters are significantly different due to different optical properties of the electrodes and the different thickness of the charge carrier transport layers. As the result of the reflective bottom contact, a bottom-emitting OLED shows a weak microcavity effect. This microcavity effect is much stronger in a top-emitting OLED because of the reflective bottom and partially reflective top contact. It is well known that the spontaneous emission of an exciton is influenced by the environment in which the radiative decay of the exciton takes place, as indicated by Fermi's Golden Rule:

$$K_{i \rightarrow f} = \frac{2\pi}{\hbar} |M_{i \rightarrow f}|^2 \rho_f, \quad (4.3)$$

where the decay probability K depends on not only the coupling between the initial (i) and final (f) state of a system, but also on the density of the final states (ρ_f). Because of the different microcavity effect, the density of optical states in a top and bottom-emitting OLED is different, which leads to a modification of the exciton lifetime according to [144]

$$\frac{\tau}{\tau_0} = \frac{4\pi^2 V_m}{3Q (\lambda_c / n)^3} \times \zeta, \quad (4.4)$$

where τ_0 and τ are the exciton lifetime in free space and cavity (here: OLED), respectively. In Eq. 4.4, the first term is the well known Purcell Factor, which is only related to cavity properties: λ_c and Q are the resonance wavelength and quality factor of the cavity, respectively. V_m is the mode volume and n is the refractive index of the

cavity medium; the second (ξ) describes the spectral and spatial matching between the exciton and cavity mode, being normally smaller than 1. Eq. 4.4 predicts that the radiative lifetime of excitons can be much lower in top-emitting OLEDs than in corresponding bottom-emitting devices due to a stronger microcavity effect (larger Q factor). Fig. 4.21 shows the measured exciton decay of bulk films of the emission layer in comparison to bottom and top-emitting OLEDs. As expected, excitons in all top-emitting OLEDs show the shortest lifetimes. Since the triplet lifetime is defined as the inverse of the sum of radiative and non-radiative decay rates of an excited triplet state, the decrease of exciton lifetime corresponds to an increase of the total exciton decay rate. Considering that the enhanced spontaneous emission in a stronger cavity does not affect the non-radiative decay since the optical structure of the device should not influence non-radiative decay pathways, the increase of exciton decay rates mentioned above is mainly due to the increase of radiative decay. The internal quantum yield (η_{int}) can be expressed as [30]

$$\eta_{int} = 1 - \frac{\kappa_{nr}}{\kappa_r + \kappa_{nr}}, \quad (4.4)$$

where κ_r is the radiative decay rate and κ_{nr} the non-radiative decay rate. It is shown by Eq. 4.4 that the quantum yield can be enhanced when the radiative rate κ_r is increased. However, no enhancement is expected when the photoluminescence quantum yield of an emitter is close to unity. In this case, the non-radiative decay rate κ_{nr} is close to zero. This is consistent with the results of the blue and green devices in this study. Both the green emitter Ir(ppy)₃ and the blue emitter FIrpic have nearly 100% phosphorescence quantum efficiency in suitable host-guest films [140] and, therefore, the non-radiative decay of excitons in the emitter is negligibly small compared to the radiative decay. As the result, although the triplet lifetime in green and blue top-emitting OLEDs is reduced compared to equivalent green and blue bottom-emitting devices, as shown in Fig. 4.21, the intrinsic quantum yield of the emitters can not be improved anymore. This leads to a comparable external quantum efficiency for green as well as blue top- and bottom-emitting OLEDs. Although no precise value of the intrinsic quantum yield of the red emitter Ir(piq)₃ is available, it is estimated to be around 50% from the external quantum efficiency of red bottom-emitting OLED [143] and a comparison of quantum yield between Ir(ppy)₃ and Ir(piq)₃ in solution [145]. Therefore, according to Eq. 4.4, the radiative and non-radiative decay rates of excitons in the red emitter are comparable. As expressed in Eq. 4.4, the quantum efficiency of the red top-emitting OLED can thus be enhanced compared to the bottom-emitting counterpart. Indeed, as compared in Table 3 and Table 5, this is observed for the OLED comprising the red emitter Ir(piq)₃ where we

observe an efficiency increase of more than 20%.

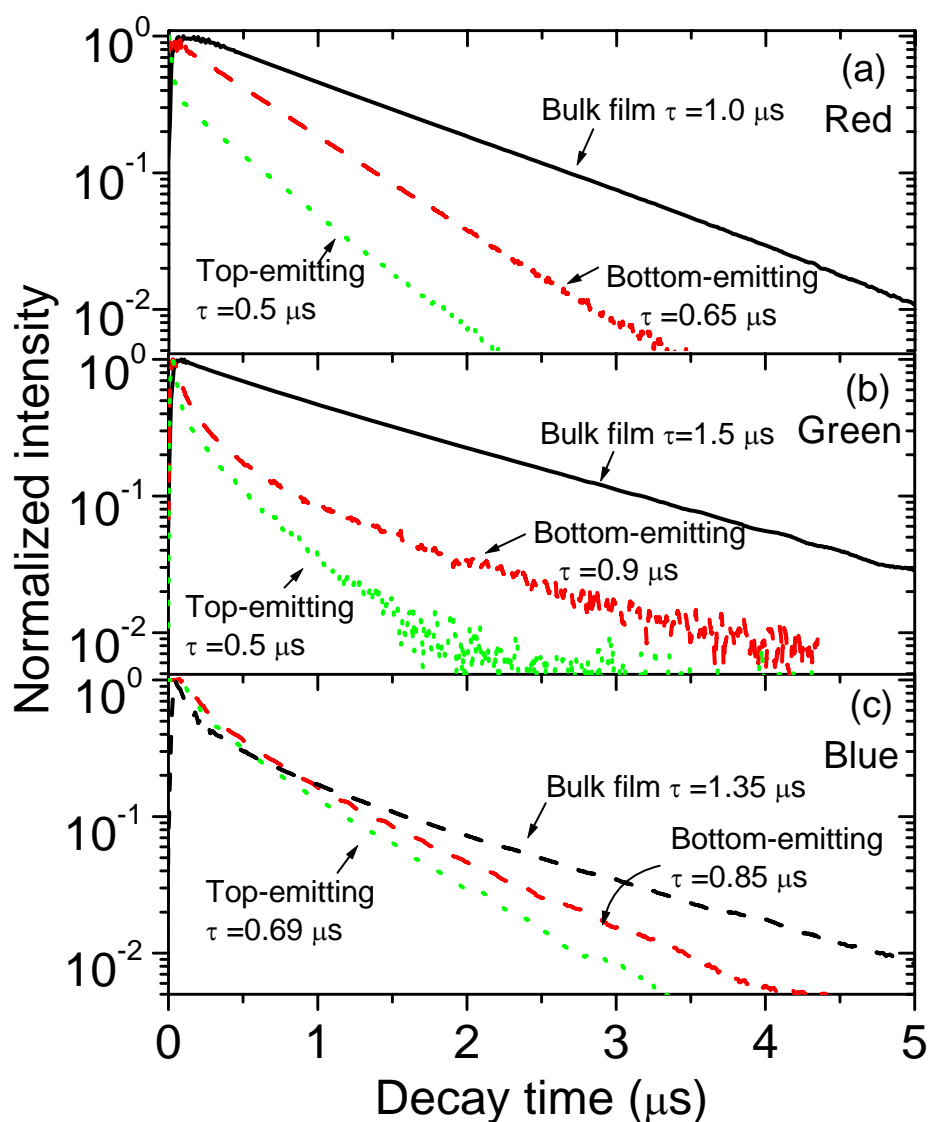


Fig. 4.21. Measured exciton decays of the bulk film of host-guest emission layers, bottom- and top-emitting OLEDs for (a) red, (b) green, and (c) blue. The exciton lifetime of every device is extracted from corresponding decay curve assuming an exponential decay.

Still, for all three colors, the enhanced emission rate can reduce bimolecular quenching processes in OLEDs occurring at high brightness. Phosphorescent OLEDs usually show the influence of quenching processes such as triplet-triplet annihilation (TTA) and triplet-polaron quenching (TPQ), resulting in a reduction of the external quantum efficiency at high current density [146-148]. The magnitude of both processes is affected by the triplet lifetime, i.e. a reduction of τ also reduces the bimolecular processes, which is clearly indicated by [148]

$$\frac{\eta(j)}{\eta_0} = \frac{ew}{\tau j} \left\{ \left[\frac{\left(\frac{1}{\tau} + K_p C j^{1/(l+1)} \right)^2 + 2K_{TT} \frac{j}{ew}}{K_{TT}^2} \right]^{1/2} - \frac{\frac{1}{\tau} + K_p C j^{1/(l+1)}}{K_{TT}} \right\}, \quad (4.5)$$

where η_0 and $\eta(j)$ are the initial quantum efficiency and quantum efficiency at the current density of j , respectively. K_{TT} and K_p are the rate constants of TTA and TPQ processes respectively, which can be determined by experiments. w is the thickness of the excitation formation zone, which can also be determined by experiments and e is the elementary charge. The parameter l ($l = E_t/KT$, E_t -depth of trap states) characterizes the spatial and energetic distribution of traps, which equals to 1 in case of trap free or shallow traps. The parameter C in the equation describes microscopic properties (the mobility, dielectric constant etc.) of a certain system, which can only be estimated from experiments. We have thus investigated the external quantum efficiency as a function of current density, using a calculated quantum efficiency based on the assumption of Lambertian distribution of light. This assumption does not influence the shape of the efficiency curves, but only the absolute value of the light emission efficiency of the OLEDs^m. The external quantum efficiency vs. current density of the green and red devices is shown in Fig. 4.22. It is clearly seen that the bottom-emitting OLEDs have a stronger efficiency roll-off compared to the corresponding top-emitting OLEDs, in particular for high current densities. Fits based on a model [148] using Eq. 4.5, which theoretically describes the quenching processes (TTA and TPQ) as a function of current density, are also shown in the figure to show the influence of the triplet lifetime on the roll-off behaviourⁿ. One can clearly see that the efficiency roll-off is reduced for the case of top-emitting OLEDs, which is attributed to reduced quenching as a consequence of a shorter triplet lifetime in the top-emitting devices.

The efficiency roll-off of the red and green top- and bottom-emitting devices with the identical emitting systems is further compared in Table 6. Although some green and red bottom-emitting OLEDs have higher external quantum efficiency than their top-emitting counterparts, they still have a more severe efficiency decrease at the same brightness range. It is clearly shown that not only all the top-emitting OLEDs, but also the bottom-emitting microcavity OLED show a less pronounced efficiency-roll off than the corresponding bottom-emitting OLEDs, which confirms that the reduced efficiency roll-off in top-emitting OLEDs is really attributed to the reduced exciton lifetime as discussed in Fig. 4.21.

^m This is true if there is little change of recombination zone with increasing current.

ⁿ The calculation was made by Sebastian Reineke of IAPP.

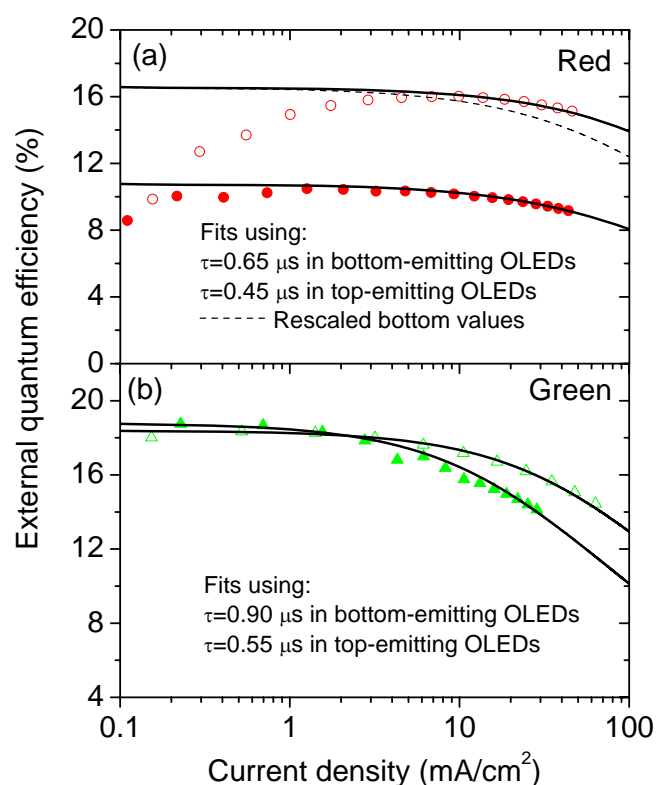


Fig. 4.22. Calculated quantum efficiency at different current density based on the assumption of Lambertian distribution of light of (a) red and (b) green bottom- (solid squares) and top-emitting OLEDs (open triangles). The solid lines are the calculated fits based on a model [148] and the dashed line in Fig. 4.22a is the fit of the red bottom-emitting OLED rescaled as a guide to eyes.

	Top-emitting	Bottom-emitting
EQE of green OLEDs at 5000/15000 cd/m ²	18.4/17.7 (7.6%)	16.4/14.1 (14.0%)
	14.5/13.4 (7.6%)	16.1/14.3 (11.2%)
	16.9/15.6 (7.6%)	14.5/12.7 (12.4%)
	18.5/17.6 (5.1%)	15.3/13.2 (13.7%)
	18.9/17.7 (6.3%)	21.2/19.1 (10%) ^M
	17.2/16.1 (6.3%)	18.7/16.7 (10.7%) ^M
	17.6/16.4 (6.8%)	18.8/16.5 (12.2%) ^M
EQE of red OLEDs at 1000/2000 cd/m ²	4.8/4.4 (8.3%)	5.1/4.5 (11.7%)
	11.6/10.8 (6.9%)	9.8/8.7 (11.1%)
	13.9/13.1 (5.7%)	10.9/9.9(9.2%)
	11.6/10.8 (6.9%) ^{MC}	

Table 6. External quantum efficiencies of green and red top- and bottom-emitting OLEDs. The values in the parentheses represent the efficiency roll-off at the corresponding brightness. MC-microcavity bottom-emitting OLEDs; M: OLEDs with microlens at the back of the glass substrate to improve light outcoupling.

4.5 Conclusions

It has been demonstrated that the use of doped transport layers allows a flexible choice of the contact metals both for cathode and anode without compromising the charge carrier injection properties. Furthermore, it has been also shown that by using doped transport layers, it is possible to vary the transport layer thickness without significantly disturbing the electrical device characteristics such as charge carrier balance etc., because of their high conductivities. As a result, doped transport layers allow optimizing the electrical and optical properties of top-emitting OLEDs at the same time. Because of its excellent electrical and optical properties (high reflection and low absorption), Ag was used as both anode and cathode material for high efficiency top-emitting OLEDs with low driving voltage.

The performance of the top-emitting devices can be further improved by an organic capping layer. This improvement can be attributed to the change of the interference effects within the devices. From a comprehensive experimental study on the influence of an organic capping layer on the performance of top-emitting OLEDs, it has been demonstrated that both the current efficiency in forward direction and the external quantum efficiency of the device can be improved significantly. This improvement can be attributed basically to the enhancement of the device outcoupling efficiency due to the modification of the optical device structure by this capping layer, which produces a microcavity enhancement effect while minimizing the absorption. After extending the capping strategy to red and blue top-emitting OLEDs, highly efficient RGB top-emitting OLEDs have been demonstrated with external quantum efficiencies reaching 15%, 20%, and 5% at a brightness of 1000 cd/m² for red, green and blue, respectively.

Finally, we have demonstrated that the efficiency of top-emitting OLEDs can be much higher than corresponding bottom-emitting OLEDs even at similar outcoupling efficiency: Due to enhanced intrinsic quantum yield as the result of shorter triplet exciton lifetime and comparable radiative and non-radiative recombination rates, red top-emitting OLEDs showed a significantly higher external quantum efficiency (more than +35%) than the red bottom-emitting OLEDs. Furthermore, it has been demonstrated that the decrease of triplet lifetime results in reduced bimolecular quenching processes, especially in the high current density range.

Chapter 5

Top-emitting OLEDs with inverted structure

In this Chapter, a study on inverted top-emitting OLEDs will be presented. It will be shown that a typical inverted top-emitting OLED has a reduced electrical performance compared to its non-inverted counterpart even when having identical layer structure (in opposite layer sequence). Then, several inverted top-emitting OLEDs with identical structure but different electrodes will be compared. It is found that the influence of the electrodes on the device electrical properties is not negligibly small despite the fact that both p- and n- doped charge transport layers are used in all cases. By simulating both hole and electron injection into the emission layer with single carrier device structures, it is found that the electrical difference between the inverted and non-inverted OLEDs are due to the different carrier injection from cathode and anode. A metal/organic interface study based on evaluation of single carrier devices suggests different effective injection barriers between interfaces of metal-on-organic and organic-on-metal.

5.1 Introduction

In current active-matrix organic light-emitting displays based on conventional top-emitting OLEDs (non-inverted), usually low-temperature p-type polycrystalline silicon (LTPS) thin film transistor (TFT) backplane technology is used. However, to compete with other flat panel display technologies, amorphous silicon TFT (α -Si TFT) backplanes would be desirable because they can be manufactured in large sizes more easily and cheaply than LTPS-TFT backplanes. Since only n-type TFT can be made on α -Si backplanes, top-emitting OLEDs having the cathode as bottom and the anode as top electrode, referred as inverted top-emitting OLEDs, are desirable. These devices have a reversed structure compared to conventional OLEDs (see Fig. 5.1).

Therefore, there is an increasing interest to develop inverted top-emitting OLED technology to adapt OLEDs to the well-developed α -Si TFT backplane technology [21-23, 149, 150].

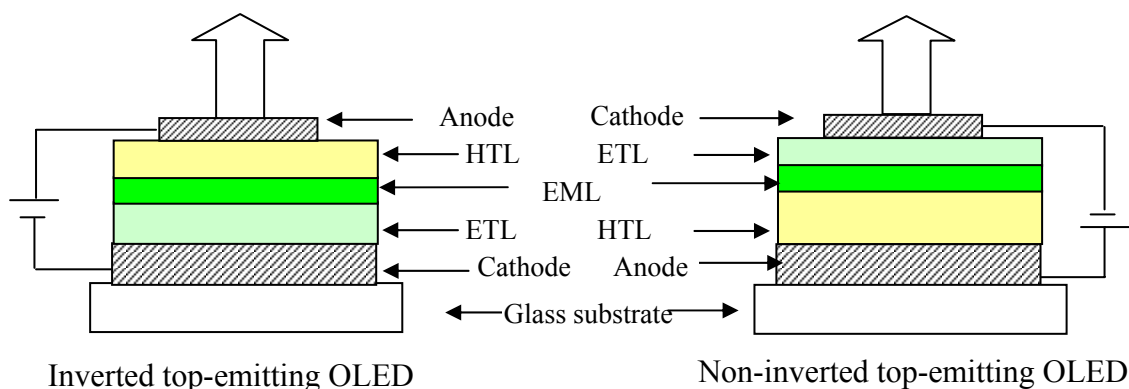


Fig. 5.1. Schematic illustration of an inverted (left) and non-inverted (right) top-emitting OLED structure.

5.2 Challenges introduced by the inverted structure

5.2.1 Inverted and non-inverted top-emitting OLEDs

It has been demonstrated experimentally in Chapter 4 that the use of doped charge carrier transport layers (both n- and p-type) allows for a flexible choice of the contact metals for both electrodes. As the result, Ag has been successfully used both as cathode and anode to achieve high performance non-inverted top-emitting OLEDs because of its excellent optical and electrical properties. Therefore, an intuitive way to design an inverted top-emitting OLED would be to replicate the basic structure of a non-inverted device in such a way that the sequence of all organic layers is reversed (see Fig 5.1), while the total layer thickness and the position of emission zone is kept unchanged. Consequently, the device structure of an inverted and a non-inverted top-emitting OLED could be as follows:

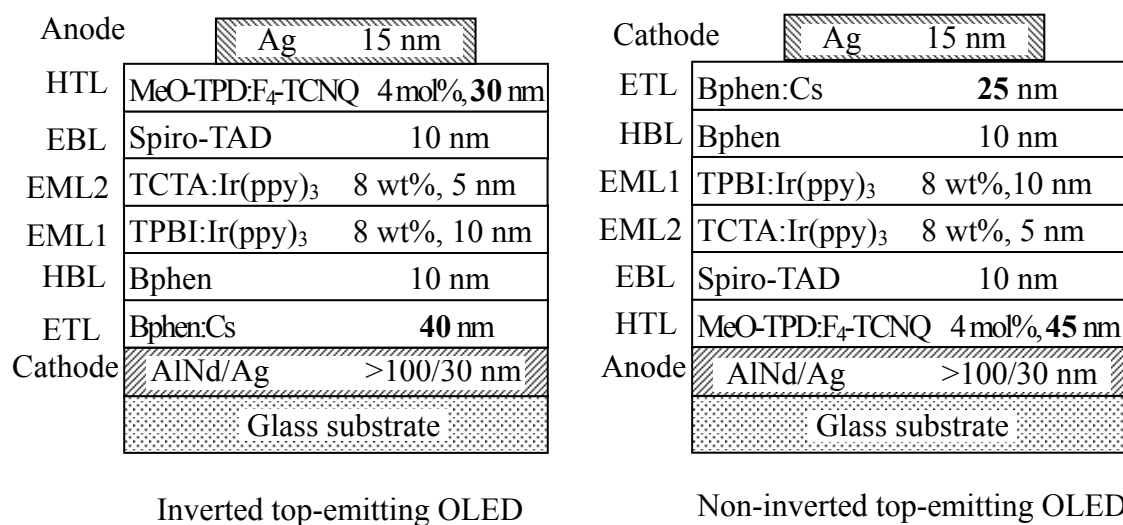


Fig. 5.2. Device structure of an optimized (left) inverted and (right) non-inverted top-emitting OLEDs.

Although hole and electron injection in the two devices occurs from Ag electrodes to the hole and electron transport layers, respectively, their J-V curves are considerably different, as shown in Fig. 5.3a: The inverted top-emitting OLED shows not only a higher onset voltage (around +0.5 V), but also a flatter J-V curve than the non-inverted device, suggesting that there are problems of charge carrier injection to the emission zone in the inverted device. Fig. 5.3b shows calculated capacitance-voltage (C-V) and resistance-voltage (R-V) spectra of the two devices from impedance spectrum measurements at a frequency of 100 Hz, where only the capacitance of the barrier (including depletion region) and undoped layers can be measured. Consistent with the J-V curves, both the C-V and R-V curves demonstrate superior electrical properties of the non-inverted OLED over the inverted device. Besides the onset voltage, there is another difference between these two C-V curves: In the inverted device, the capacitance decrease with increasing bias voltage (illustrated by a blue arrow in Fig. 5.3b) is observed right before an abrupt increase of the capacitance (from the bias voltage of 2.9-3.3 V). This indicates that additional barriers are introduced in the inverted device by just reversing the device structure. Unfortunately, a detailed understanding and analysis of these barriers can not be obtained with the methods and device structures used here.

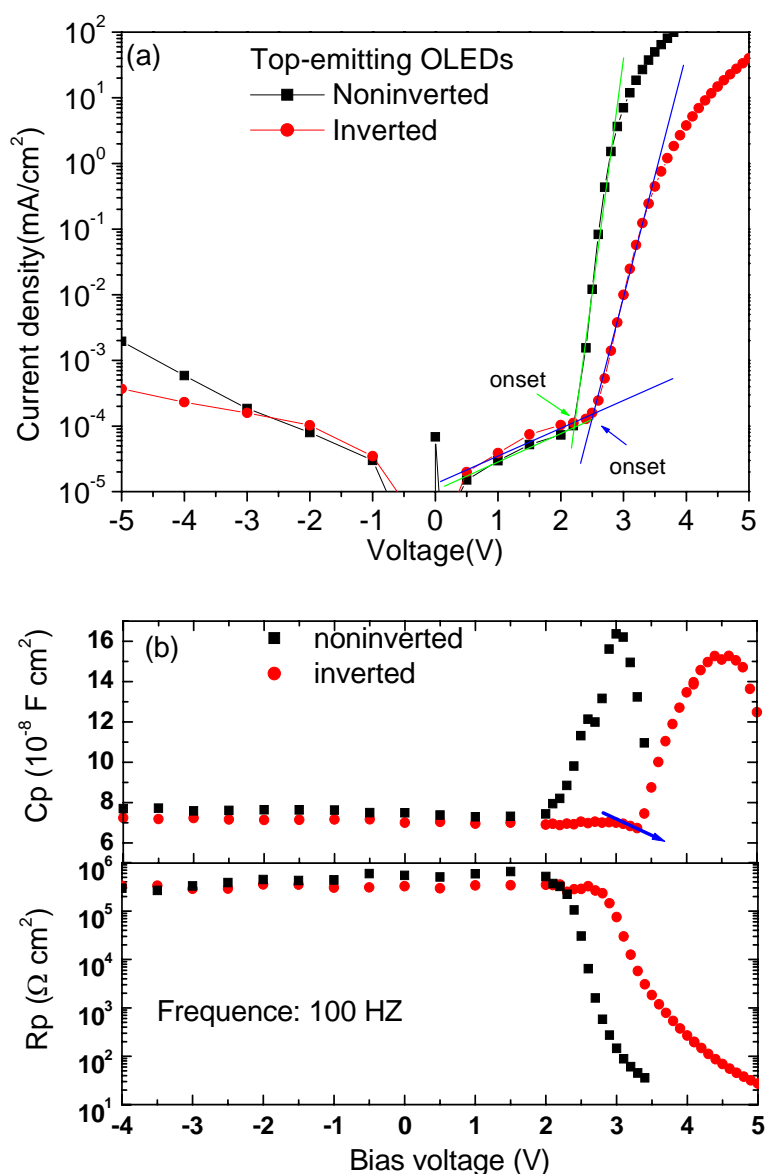


Fig. 5.3. (a) J-V characteristics and (b) C-V/R-V spectra of the inverted and non-inverted top-emitting OLEDs.

5.2.2 Inverted top-emitting OLEDs with different electrodes

Another peculiarity of inverted devices compared to non-inverted devices is that the electrode materials have a relatively large influence on the electrical properties of inverted top-emitting OLEDs, as demonstrated in Fig. 5.4, where the J-L-V characteristics of inverted devices with different electrodes are compared. All the inverted devices studied had an identical structure but different cathode and anode combination, which were Ag/Ag, Al/Ag, Ag/Au and Al/Au:

Glass substrate/ Cathode (30 nm)/ Bphen:Cs (40 nm)/ Bphen(10 nm)/ TPBI:Ir(ppy)₃ (8 wt%, 10 nm)/ TCTA:Ir(ppy)₃ (8 wt%, 5 nm)/ Spiro-TAD (10 nm)/ MeO-TPD:F₄-TCNQ (4 mol%, 30 nm)/ Anode (15 nm)

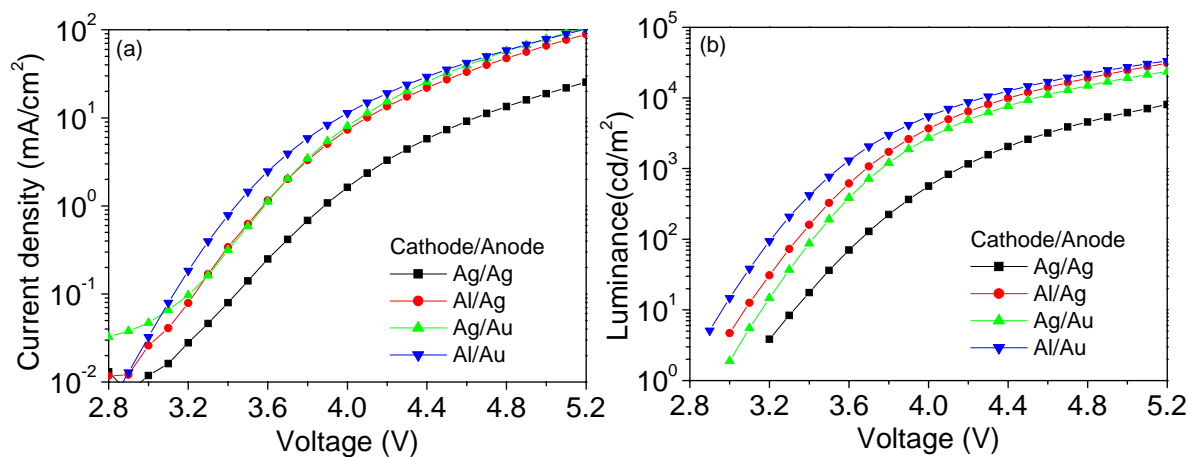


Fig. 5.4. (a) J-V and (b) L-V characteristics of inverted top-emitting OLEDs with different electrode combination.

In Fig. 5.4a, it is clearly shown that different electrode combinations lead to different electrical device properties: The device using Ag both as cathode and anode has the worst electrical performance (black curve). By replacing one electrode with Al as cathode (red curve) or Au as anode (green curve), the device improves. The best electrical properties are achieved by replacing both Ag electrodes with Al and Au as cathode and anode, respectively. Consistent with their electrical properties, the device using the Al/Au electrode combination has the lowest operating voltage while the device having Ag as both cathode and anode shows the highest driving voltage (see Fig. 5.4b). It is obvious that not only the top anode, but also the bottom cathode has large influence on the electrical device properties (their driving voltage etc.) and eventually on the device efficiency, despite the fact that both n- and p-doped transport layers are used. This is contradictory to the case of non-inverted devices where electrode materials have almost no influence on electrical device properties, as demonstrated in Section 4.2.1. Moreover, although the inverted top-emitting OLED using Al and Au as bottom cathode and top anode, respectively, has the best electrical properties among all four inverted devices (see Fig. 5.4b), its operating voltage is still higher than that of corresponding non-inverted devices (both top- and bottom-emitting OLEDs). At a brightness of 100 cd/m² and 1000 cd/m², the driving voltages are around 3.2 V and 3.6 V, which is about 0.5 V and 0.7 V higher than for the corresponding non-inverted devices.

5.2.3 Charge carrier injection

The inferior electrical properties of the inverted top-emitting OLEDs compared to non-inverted devices are most likely due to their bad carrier injection. Thus, single carrier devices (hole and electron only) were used to simulate and compare charge carrier injection in inverted- and non-inverted OLEDs (see Fig. 5.5). Fig 5.5a is the J-V curve of a hole-only device with Ag as both top (as in the case of the inverted devices) and bottom contact (as in the case of the non-inverted devices). It is clearly shown that the J-V curve is asymmetric with a slightly better hole injection from the bottom contact (non-inverted case), although the device structure is nominally symmetric. The asymmetry of the J-V curve is even more pronounced in the electron-only device which, in contrast to the hole only device, demonstrates the significantly better electron injection from the top (non-inverted case). Therefore, it can be concluded that the higher operation voltage in inverted top-emitting OLEDs is due to injection problems of both holes and electrons from the bottom cathode and top anode, respectively. Moreover, compared to the problem of hole injection, it is obvious that the problem of electron injection is more severe in inverted OLEDs.

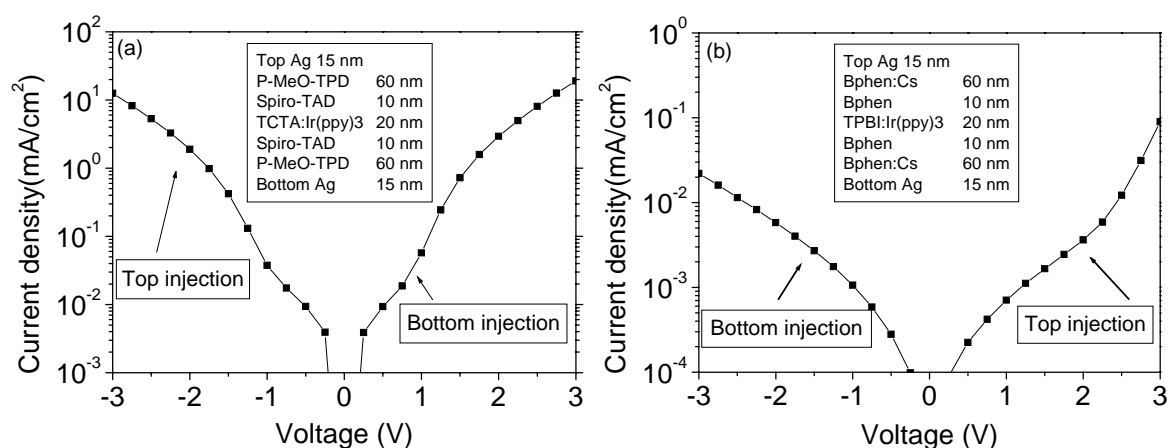


Fig. 5.5. J-V curves of (a) the hole-only device and (b) the electron-only device. Their device structures are shown in the inset.

5.2.4 Surface conditions of contacts

There is a possibility that the different charge carrier injection to the emission layer as discussed above is mainly due to the different surface conditions (mainly oxidation) of the bottom cathode in inverted OLEDs compared to the top cathode in non-inverted devices [151]: In the case of inverted devices, it is the bottom cathode (Al or Ag) that is deposited before n-doped ETL is deposited. The procedure could induce an oxidation of the Al or Ag bottom cathode, which might lead to the

problem of charge injection and eventually to high driving voltages in inverted top-emitting OLEDs. However, it is observed that Al oxide also exists in the non-inverted device as shown in Fig. 5.6. This is attributed to a reaction of Al with residual oxygen in the deposition chamber during the evaporation of the Al top cathode. Fig 5.6a shows the element profile extracted from dynamic XPS spectra of a conventional OLED using Al and ITO as top cathode and bottom anode, respectively. It is clearly shown that around 10% of oxygen exists at the Al/organic (n doped Bphen) interface, which is attributed to native Al oxide grown during metal deposition. This is further confirmed in Fig 5.6b, where the dynamic XPS profile of a sample consisting of Al (100 nm) deposited on Bphen (100 nm) is shown. From the change of Al 2p line at a binding energy around 73 eV (belongs to Al) to around 76 eV (belongs to Al_2O_3) with sputtering time, we conclude an oxidization of Al in the form of Al_2O_3 at the organic/Al interface. Moreover, it has been reported by other groups that Al oxide improves the electron injection [152]. Therefore, an oxidization of the Al or Ag bottom cathode in the inverted devices is not the reason for their higher operating voltage.

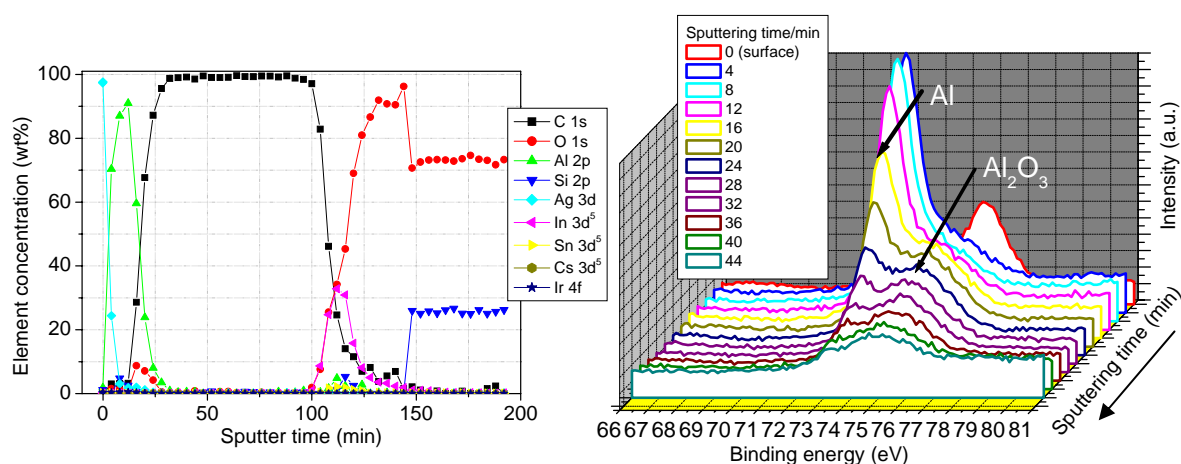


Fig. 5.6. (left) Element profile extracted from dynamic XPS spectra of a conventional bottom-emitting OLED and (right) Dynamic XPS spectra of Al 2p of an Al-on-organic sample [153].

5.3 Metal/organic interface study

As demonstrated above, the major difference between inverted and non-inverted top-emitting OLEDs using Ag electrodes is their device structures with opposite organic layer sequence. This would lead to different metal/organic and organic/organic (O/O) heterojunction, as illustrated in Fig 5.7. It is expected that there is little difference between two O/O interfaces with opposite layer sequence because there is rarely interdiffusion and reaction at the interfaces [43]. Therefore, the inferior electrical performance of inverted top-emitting OLEDs compared to corresponding

non-inverted devices is most likely due to the different metal/organic interfaces.

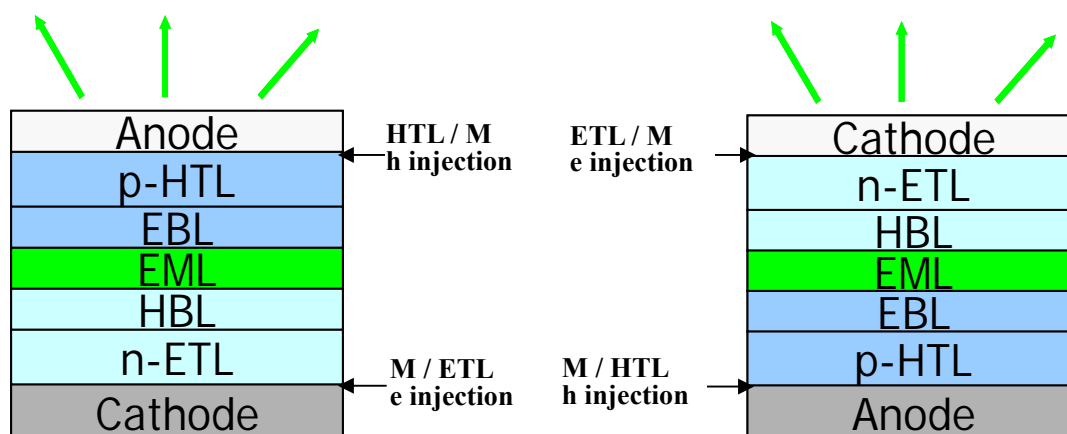


Fig. 5.7. Schematic illustration of (left) an inverted top-emitting OLED and (right) a non-inverted top-emitting OLED.

It is known from literature that a metal-organic pair may give different interfaces when the metal is deposited on the organic (O/M) and the organic is deposited on the metal (M/O) due to metal diffusion or reaction at the O/M interface [154-156]. It is thus necessary to investigate the difference of these interfaces and their effects on the device performance.

5.3.1 Interfaces of metal on Bphen (ETL) and Bphen on metal

The electron-only device structure was used to investigate interfaces of metals (Al or Ag) deposited on Bphen (undoped and doped) and Bphen deposited on the metals. Single carrier devices with only undoped ETL or n doped ETL were studied with the following structures:

MiM

Metal substrate/ Al (15 nm)/ Bphen (100 nm)/ Al (30 nm)

nin

Metal substrate/ Al (15 nm)/ Bphen:Cs (15 nm)/ Bphen (130 nm)/ Bphen:Cs (15 nm)/ Al (30 nm)

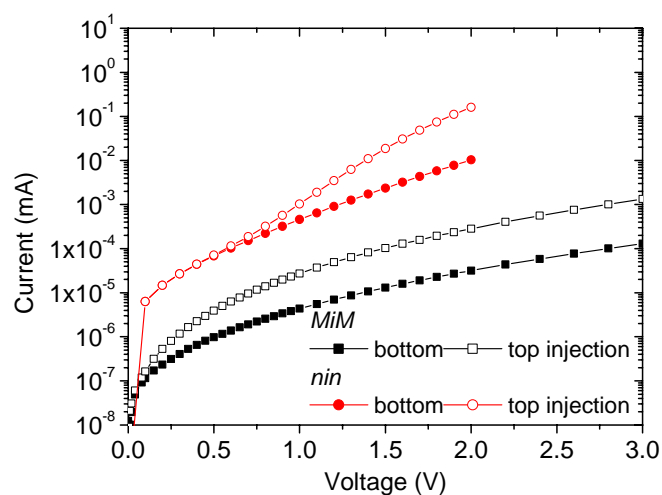


Fig. 5.8. I-V characteristics of the *MiM* (black) and *nin* (red) electron only devices.

The I-V characteristics of the two devices are shown in Fig. 5.8. One can easily see that in the *MiM* device, electron injection from the top contact is much better than it is from the bottom contact. Due to additional n-doped Bphen layers at both bottom and top contact side, the *nin* device shows expectably much higher biased currents than those in the *MiM* device. However, electron injection from the top contact is still much better than from the bottom contact, especially at high bias voltage. The difference is not so pronounced at bias voltages below 0.4 V. C-f spectra of the *MiM* device with different bias voltage are shown in Fig. 5.9a. As expected, the C-f spectrum of the *MiM* device at the zero bias is almost independent on the frequency, which means that there is no carrier injection and only intrinsic charge carriers respond to the a.c. stimulus (20 mV). Similar to the C-f spectra at zero bias, the C-f curve at the bias of -6 V (bottom electrode negatively biased) still shows weak dependence on the frequency, suggesting that the charge injection is less efficient so that there is little space charges even at -6 V. In contrast, already at the bias of 4 V (top electrode negatively biased), the capacitance shows a steep increase towards lower frequency below a threshold frequency, which means that additional space charges respond to the a.c. stimulus and contribute to the capacitance. All these data indicate a lower effective electron injection barrier at the top compared to the bottom electrode and suggest better electron injection from the top contact, which agrees well with the I-V spectra shown in Fig. 5.8.

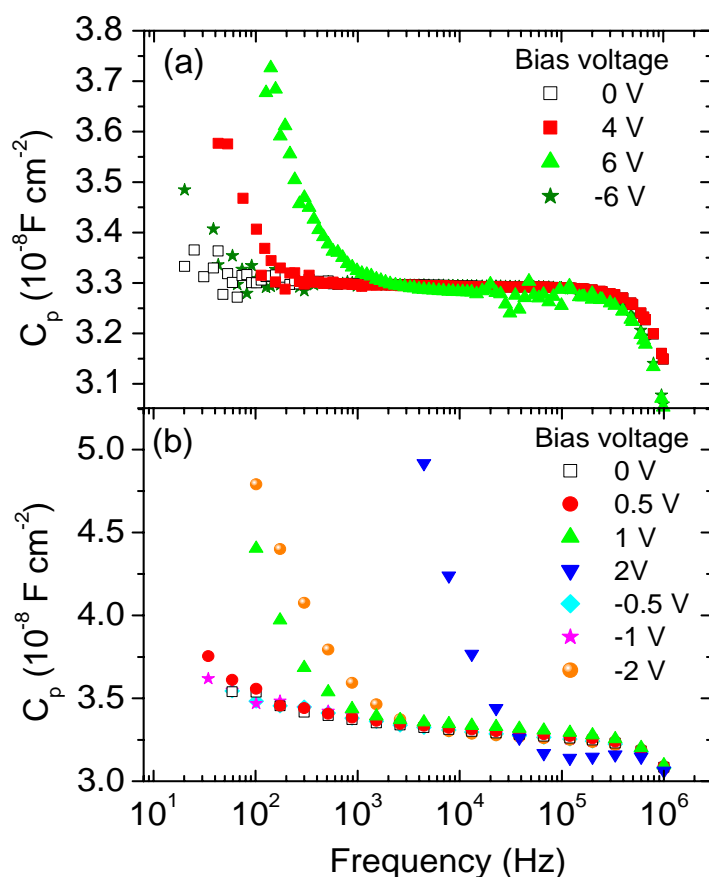


Fig. 5.9. Frequency dependent capacitance (C - f) of the (a) *MiM* and (b) *nin* electron only devices at different bias voltages.

Fig. 5.9b shows the C - f spectra of the *nin* device at different bias voltages. The spectrum at a bias of -0.5 V is very similar to that at 0 V, showing almost no space charge, indicating inefficient electron injection. However, at a bias of 0.5 V, the spectrum is obviously different, showing a steep capacitance increase with decreasing frequency, suggesting the formation of space charges. With further increase of bias voltage, the difference is even more pronounced with expected shifting of the threshold (f_{th}) to higher frequency. Combined with the I - V characteristics of the two devices, one can easily conclude that although the device structure is symmetric, the *MiM* device has a smaller effective electron injection barrier from the top than from the bottom contact. By introducing doped transport layers at both sides (the *nin* device), as expected, the barrier heights at both sides are reduced effectively, but the electron injection is still better from the top contact. This is further confirmed by the C - V spectra of these two devices at a frequency of 100 Hz in Fig. 5.10: The n -doped layer can reduce the electron injection barrier at both bottom and top sides drastically,

but the effective electron injection barrier from the top is still lower than from the bottom.

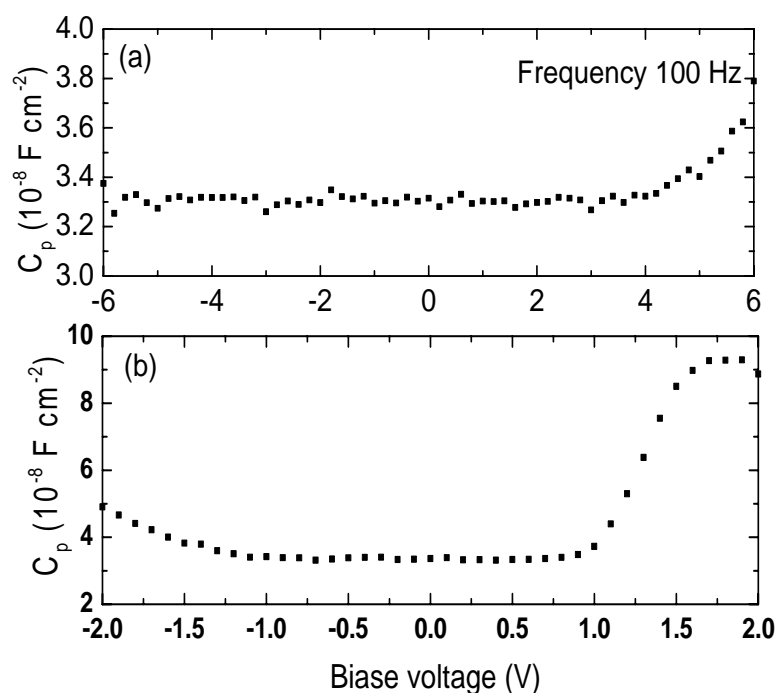


Fig. 5.10. Capacitance as the function of bias voltage (C-V) of the (a) *MiM* and (b) *nin* electron only devices at the frequency of 100 Hz.

It is known from literature that during metal deposition on organics (in the case of metal-on-organic), hot metal atoms bombard the underlying organic film with a condensation energy high enough to destroy the weakly bound van der Waals solid and thus leading to metal penetration and/or reactions at the organic/metal interface [154-156]. In contrast, when an organic is deposited on metals, the strongly bound metal surface is stable for the low-energy organic molecule, forming a sharp interface as shown schematically in Fig. 5.11.



Fig. 5.11. Schematic diagrams of (left) an organic/metal interface and (right) a metal/organic interface.

The reaction of the metal with the underlying organics at the metal-on-organic interface is confirmed by laser desorption/ionization-time of flight-mass spectrometry (LDI-TOF-MS) experiments carried out by Sebastian Scholz on the following two samples:

Metal-on-organic:

Fe target/ Bphen 20 nm/Al 15 nm

Organic-on-metal

Fe target/ Al 15 nm/Bphen 20 nm

Mass spectra of these two samples are compared in Fig. 5.12. For the metal-on-organic sample, several other compounds are found in addition to the Bphen proton adduct (m/z 333), including $[\text{Bphen}+\text{Al}]^+$ (m/z 360), $[\text{Bphen}+\text{AlO}]^+$ (m/z 376) etc. It clearly indicates that hot Al atoms react with underlying Bphen during Al evaporation. In contrast, for the organic-on-metal sample, only the Bphen proton adduct can be found in the spectrum, which means that no reaction of Bphen with the underlying metal occurs.

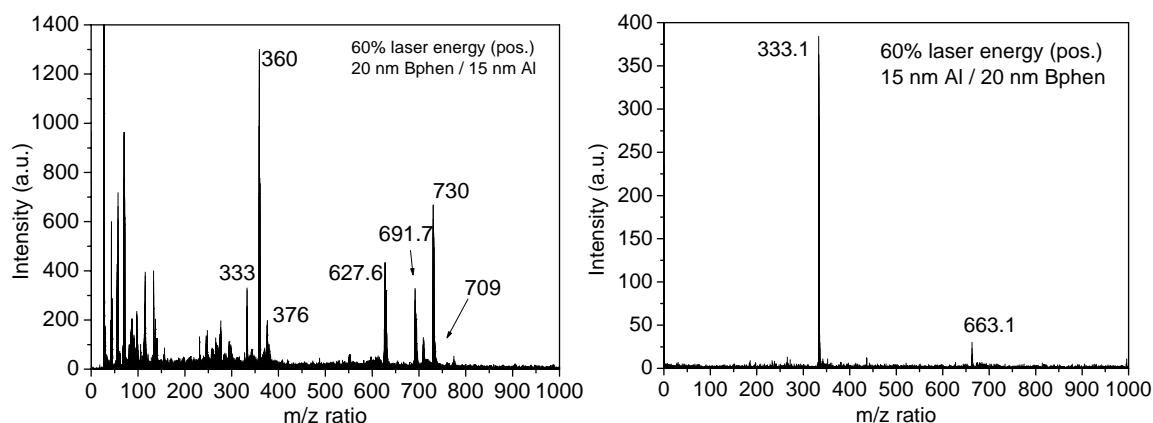


Fig. 5.12. LDI-TOF-MS of the samples (left) with 15 nm Al evaporated on 20 nm Bphen and (right) with 20 nm Bphen evaporated on 15 nm Al [157].

It has been reported that the reaction of hot metal with underneath electron conductive organic layers introduces additional gap states [158, 159]. In our case, when Al or Ag is evaporated on Bphen, formation of gap states is also expected as a result of the reaction. These gap states obviously facilitate electron injection even when the injection barrier is very low, as in the case of doped ETL [158, 159]. The same effect is also found when NET5 (Novaled electron transport material) and NDN1 (Novaled molecular n-type dopant) are used instead of Bphen and Cs.

The electrical difference between the inverted top-emitting OLEDs using Al and Ag as bottom cathode (Al is better as bottom cathode, see Fig. 5.4) is clearly reflected by Fig. 5.13. Due to the doped ETL and gap states, which are advantageous for electron injection, the two devices show almost identical top electron injection, which

agrees with the conclusion that the device performance is almost independent of the work function of metals in non-inverted top-emitting OLEDs. However, the electron only device using Al as contacts has better bottom electron injection than the one using Ag. This is tentatively attributed to different morphologies formed between Bphen deposited on Al and Ag.

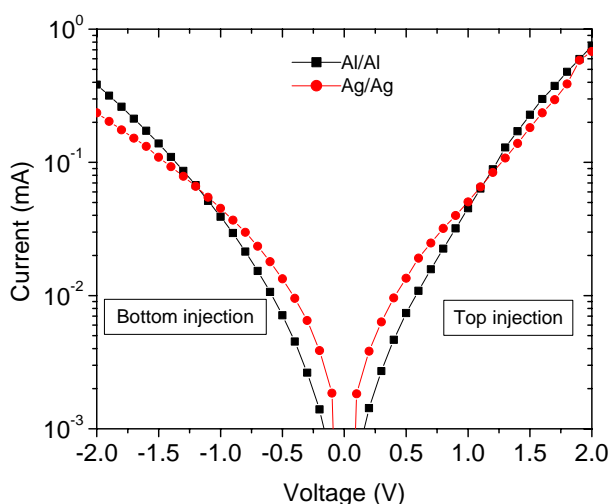


Fig. 5.13. I-V characteristics of electron only devices using Al (black) and Ag (red) as electrodes.

5.3.2 Interfaces of metal/HTL and HTL/metal

It has already been shown in Fig. 5.5 that there is also a slightly different hole injection capability between interfaces from metal on HTL (p-doped) and HTL (p-doped) on metal. The single carrier device structure was also used to investigate interfaces of metals (Ag or Au) deposited on HTLs (undoped and doped) and the HTLs deposited on the metals. Since MeO-TPD easily crystallizes, which leads to a high leakage current, NHT5 was used instead as HTL in the hole only devices^o. To have as few as possible heterojunctions involved, single carrier devices with only undoped HTL were studied at first. Nevertheless, because of possible energetic barriers at the metal/organic interfaces in the *MiM* devices, which are due to the mismatch between the work function of the electrode and the ionization potential of the HTL, further analysis of the devices is difficult. Thus, it is desirable to have at least one ohmic/quasi-ohmic contact in a single carrier device. This can be fulfilled by introducing p-type doping: As demonstrated by the energy diagram derived from UPS/XPS data (Fig. 5.14), p-type doping leads to a reduced energy barrier of 0.4 eV

^o NHT5 has a significantly higher glass transition temperature than MeO-TPD.

at the Ag/p-MeO-TPD interface, which is low enough to ensure an ohmic contact between Au/Ag and the doped HTL [59].

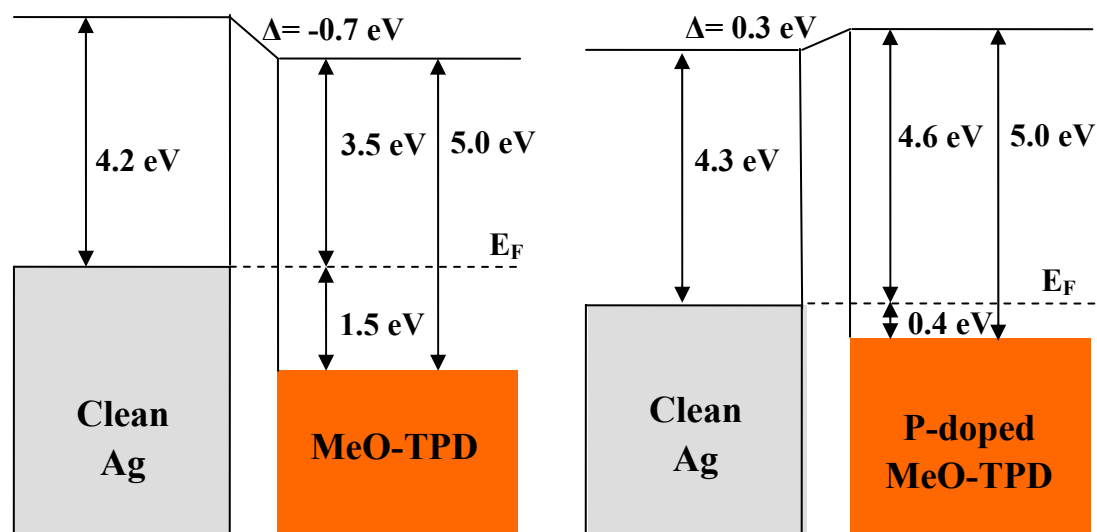


Fig. 5.14. Energy diagram as derived from UPS spectroscopy for the organic semiconductor MeO-TPD on Ag. Left side: undoped MeO-TPD on Ag; right side: MeO-TPD doped with F_4 -TCNQ^P.

Four kinds of hole only devices are compared, which have the following device structures:

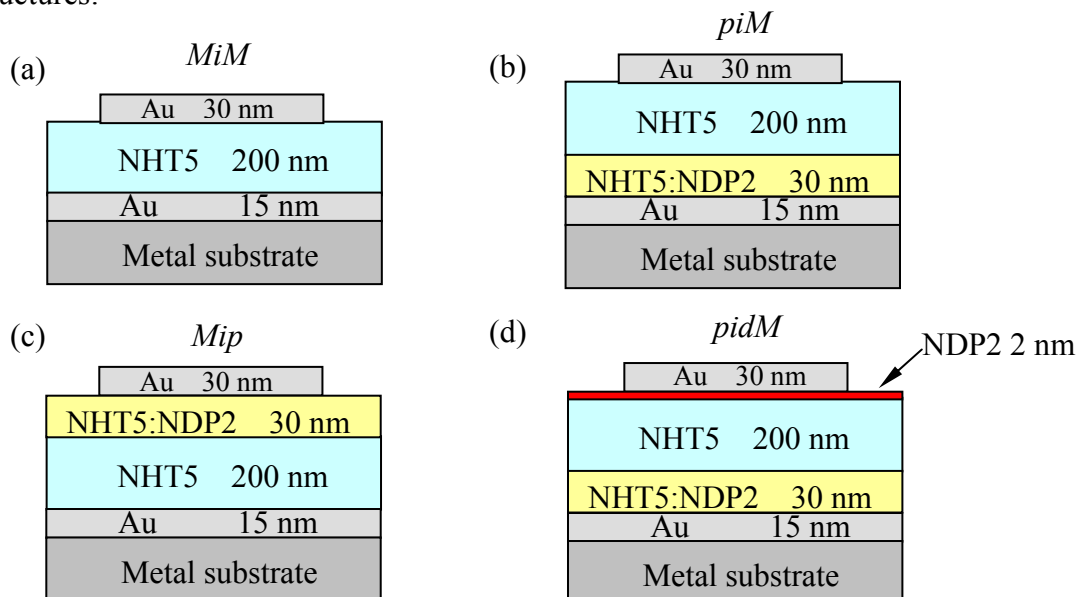


Fig. 5.15. Device structure of the (a) *MiM*, (b) *piM*, (c) *Mip*, and (d) *pidM* hole only devices.

The I-V characteristics of the four devices are shown in Fig 5.16:

1. Fig. 5.16a shows the I-V characteristics of the *MiM* device. The device has better

^P UPS measurements were conducted by Mandy Grobosch of IFW Dresden.

hole injection from the bottom than from the top contact, although both the top and bottom-biased current are very low: Around 10^{-7} and 10^{-5} mA at 4 V, respectively.

2. Fig. 5.16b shows the I-V characteristics of the *piM* device. As expected, with an additional p-HTL at the bottom side, the bottom-biased current is improved by more than three orders of magnitude compared to the *MiM* device, reaching 4×10^{-2} mA at 4 V. This improvement is attributed to the quasi-ohmic bottom contact.

3. Fig. 5.16c shows the I-V characteristics of the *Mip* device. As expected, due to the p-HTL at the top side, the device shows much better hole injection from the top than from the bottom contact. However, if one compares the *piM* and *Mip* devices, the *piM* device shows surprisingly much lower bottom-biased current (less than 10^{-5} mA at 2 V) than top-biased current (around 1 mA at 2V) in the *Mip* device, although a p-HTL is used in both cases (at bottom and top side *in piM* and *Mip* devices, respectively).

4. Fig. 5.16d shows the I-V characteristics of the *pidM* device. With additional 2 nm pure NDP2, the *pidM* device shows a high bottom-biased current (around 1 mA at 2 V), which is more than five orders of magnitude higher than its *piM* counterpart (less than 10^{-5} mA at 2 V).

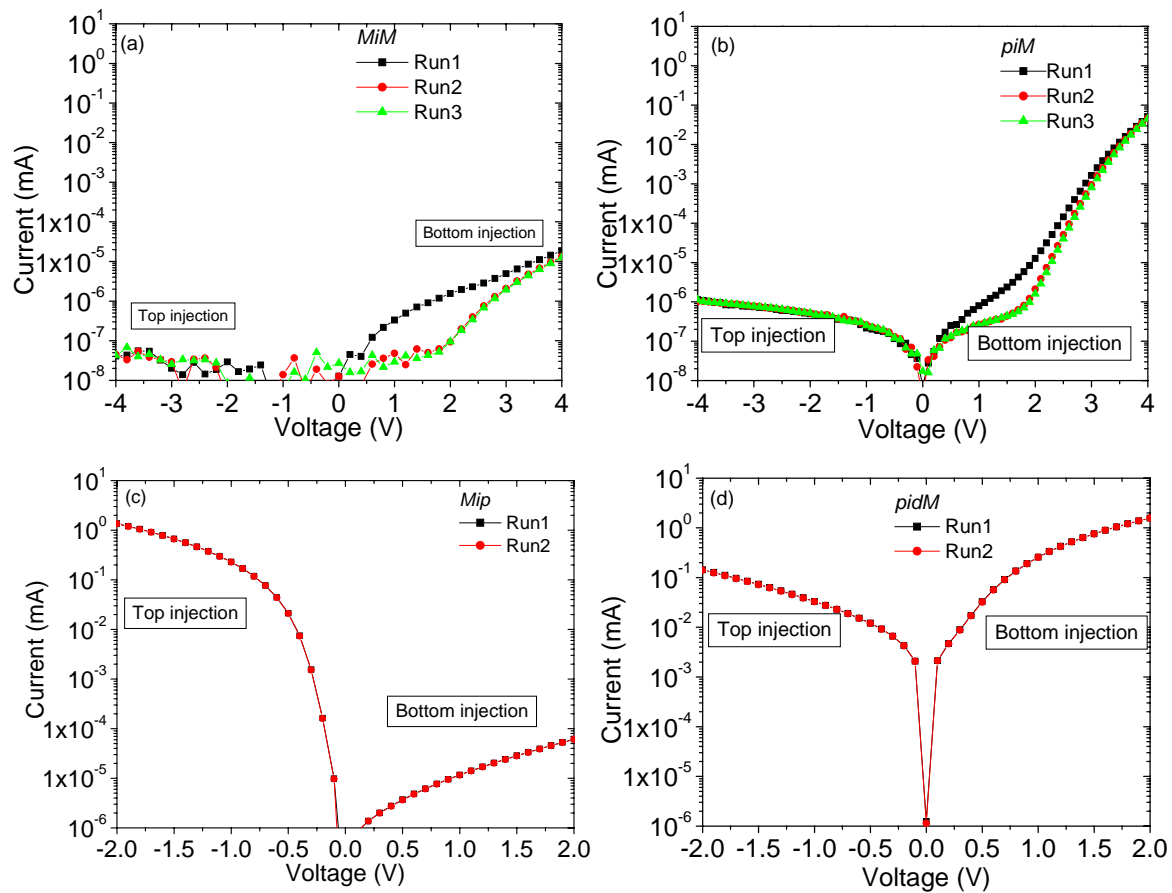


Fig. 5.16. I-V characteristics of the (a) *MiM*, (b) *piM*, (c) *Mip*, and (d) *pidM* hole only devices.

Since the bottom contact is quasi-ohmic in the *piM* device, which means efficient hole injection at the bottom, the lower current in the *piM* device compared with those in the *pidM* and *Mip* devices must be due to the difficulties of the hole extraction to the top contact. From the study of the metal/Bphen interfaces in Section 5.3.1, it is known that when a metal is deposited on an organic, the underlying organic may react/be modified by the hot metal atoms. Thus, it is expected that when Au or Ag is evaporated onto NHT 5 or MeO-TPD, the HTL at the interface may also be modified. However, in contrast to the electron case where electron injection is improved, it is obvious that the modified HTL film blocks the hole injection and transport, acting as an insulator at the metal-on-organic interface. This insulator layer concept well explains the much more efficient bottom injection than top injection in the *MiM* device. In the *piM* device, the bottom-biased injection is determined by the quasi-ohmic contact. However, the insulating layer at the top side causes an accumulation of holes at the top interface, forming an internal electric field opposite to the external biased field and thus counteracting it, which further limits hole injection. From the efficient top hole injection in the *Mip* device, it suggested that p-type doping can compensate this damage somehow. This indicates that either the p-dopant does not react with metal atoms at all or there is maybe some kind of destruction/reaction which is at least not bad for hole injection. The latter assumption is actually confirmed by the *pidM* device, which shows much higher bottom positively biased current than that of *piM* device, indicating no accumulation of holes at the top interface and, thus, no insulator layer is formed. This suggests that only 2 nm of p-dopant (NDP2) are already enough to protect the underlying NHT5 layer from damage by metal. Therefore, it is expected that some robust hole transport materials such as ZnPc, CuPc etc. can also work as protective layer. This is actually confirmed in Fig. 5.17, where two hole only devices are compared with the following structures:

piM

ITO/TNATA: F₄-TCNQ (4 mol%, 30 nm)/TNATA (200 nm)/Au (30nm)

pibM

ITO/TNATA: F₄-TCNQ (4 mol%, 30 nm)/TNATA (200 nm)/ZnPc (2 nm)/Au (30nm)

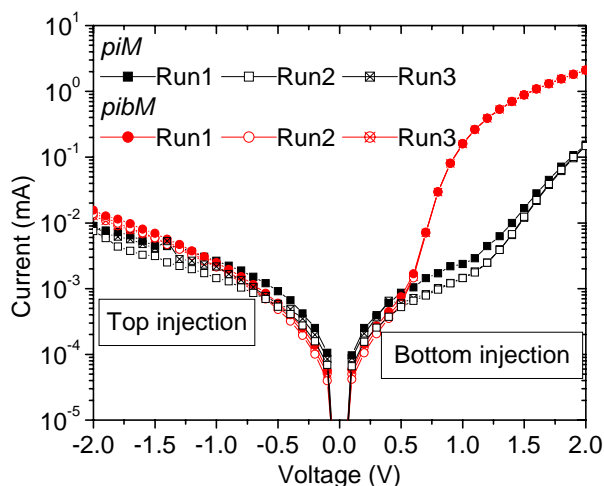


Fig. 5.17. I-V characteristics of the *piM* and *pibM* single carrier devices.

The device with 2 nm ZnPc as buffer layer (*pibM* device) shows a much higher bottom positively biased current than the device without ZnPc, which is attributed to a reduced damage of the HTL by ZnPc at the top interface.

Although the evaporation of Au and Ag onto the HTL may cause damage at the organic/metal interface, the extent of damage is clearly different for the different metals as indicated in Fig. 5.18a. In Fig 5.18a, the I-V characteristics of two *MiM* devices using Au and Ag as top electrode are compared, which have the following device structures: ITO/ NHT5 (100 nm)/Au or Ag (30 nm). Same as in the *MiM* device in Fig. 5.16a, hole injection from the bottom electrode is much better than from the top electrode because of the formation of insulating layers at the top interfaces in both devices. However, the device using Au as the top electrode has much higher bottom positively biased current than the device based on Ag, which suggests less damage of HTL introduced by Au than by Ag. As discussed above, this damage can only partly be overcome by using a doped HTL, which leads to still better top injection in the *Mip* devices using Au than using Ag as top electrode (see Fig. 5.18b). This explains why inverted top-emitting OLEDs using Au as the top electrode have better electrical properties than devices using Ag (cf. Section 5.2.2).

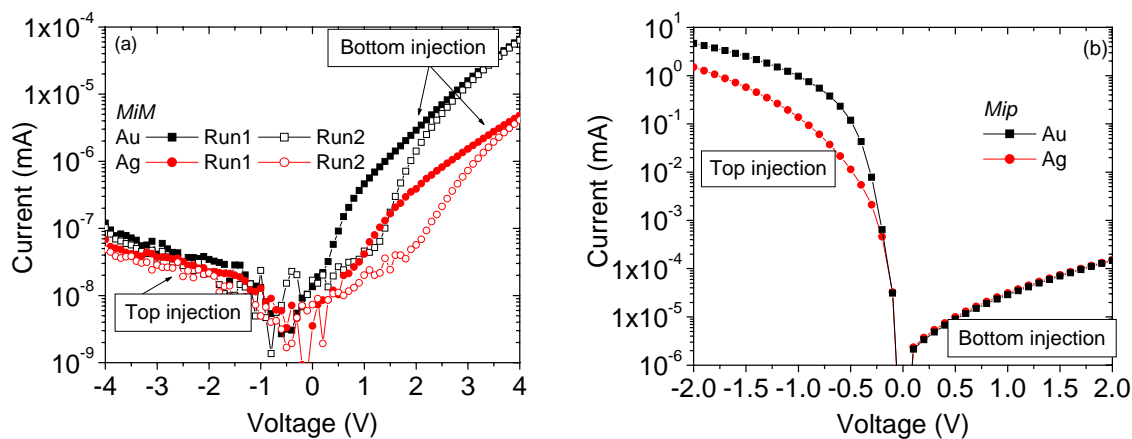


Fig. 5.18. I-V characteristics of the (a) *MiM* and (b) *Mip* devices using Au (black) and Ag (red) as the top electrode.

5.4 High efficiency inverted top-emitting OLEDs

5.4.1 Inverted devices with electron injection layers

From the above organic/metal interface study, it is clear that both electron and hole injection in non-inverted top-emitting devices are better than they are in inverted top-emitting OLEDs because:

1. When a top contact is deposited on an ETL, the ETL is modified by metal deposition, leading to the formation of gap states facilitating electron injection.
2. During top contact deposition on a HTL, the HTL is modified as well. However, in this case, the modified layer acts as insulator for hole injection and transport.

It is also shown that the modification of the HTL can be reduced somewhat by using p-type doping at the metal/HTL interface. Therefore, the less efficient electron injection from the bottom contact is the major bottleneck for the inferior electrical performance of inverted devices as compared to corresponding non-inverted OLEDs. To improve electron injection from the bottom contact into an inverted device, additional gap states have to exist like in the case of a non-inverted device. Several attempts were made for intentionally introducing gap states at the bottom interfaces by using very thin layers (called injection layer) such as *Bphen:Cs (1 nm)/Al (1 nm)* and *Alq3 (0.2 nm) LiF (0.3 nm) Al (0.4 nm)*. The device structures of these devices with and without injection layers were as follows:

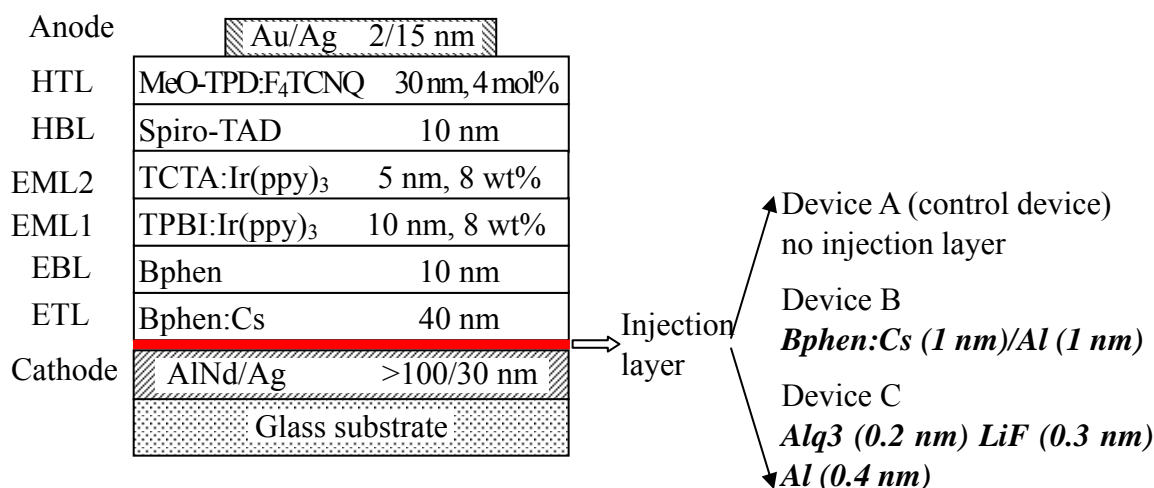


Fig. 5.19. Device structures of inverted top-emitting OLEDs with and without injection layers.

The electrical properties of these three inverted devices are compared in Fig. 5.20. It is clearly shown that the devices with injection layers (device B and C) have slightly better electrical properties than the device without the injection layer (control device A). However, at a brightness of 100 cd/m², the best operating voltage of them is still around 0.5 V higher than the non-inverted device. This suggests that the

injection layer can improve electron injection from the bottom contact, but can not completely overcome the injection problem.

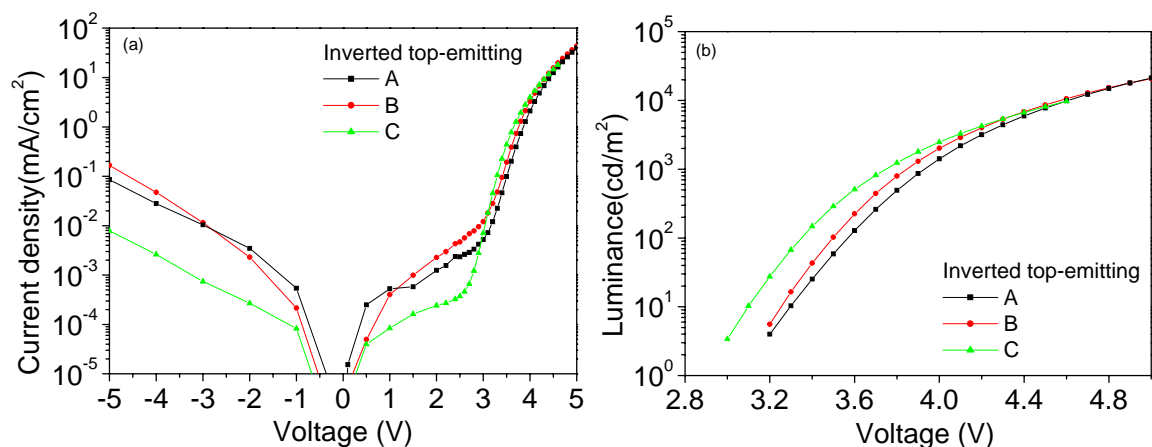


Fig. 5.20. (a) J-V and (b) L-V characteristics of inverted top-emitting OLEDs with and without injection layers.

5.4.2 High efficiency inverted top-emitting OLEDs

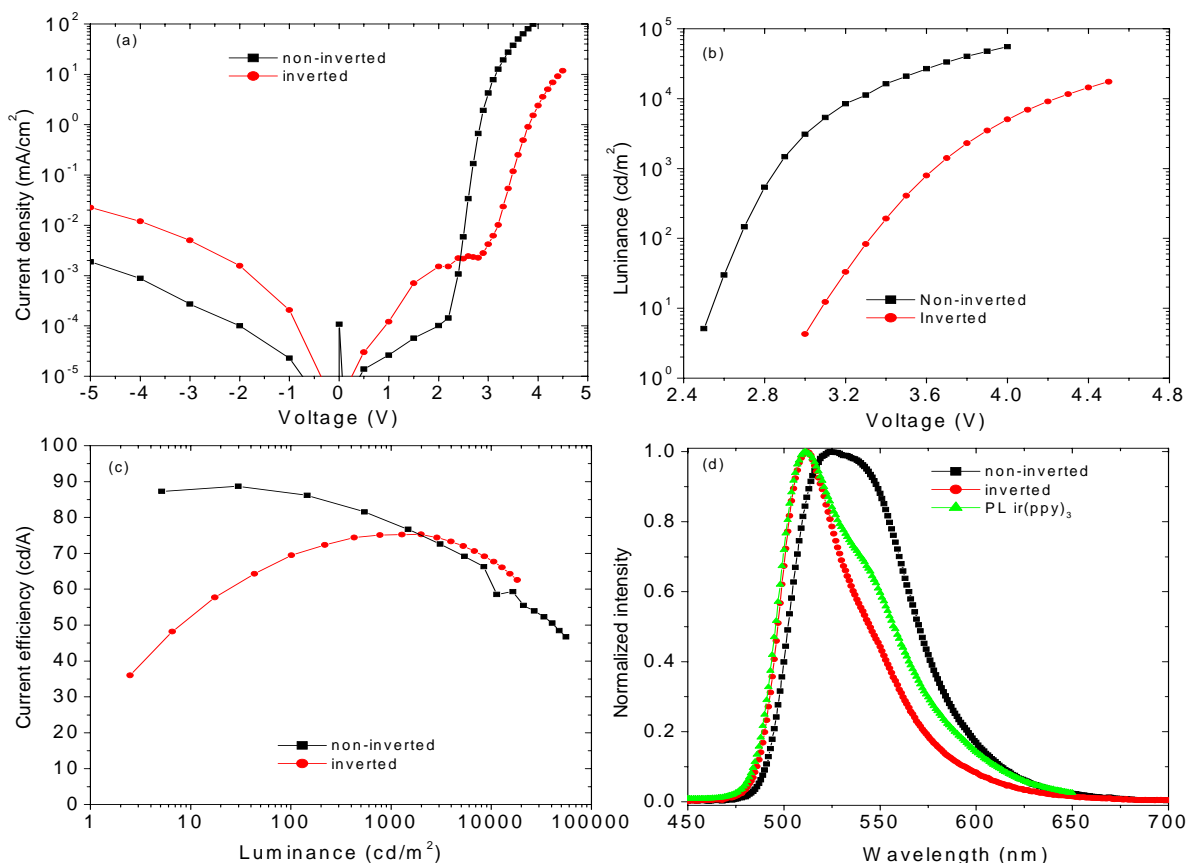


Fig. 5.21. (a) J-V, (b) L-V, (c) current efficiency, and (d) electroluminescence spectra of one of the best inverted top-emitting OLED. Characteristics of the non-inverted OLED reported in Chapter 4 is also shown for comparison.

Although the electron injection problem in inverted devices is not completely overcome, which leads to higher operating voltage compared with non-inverted devices and, thus, lower power efficiency, high performance inverted top-emitting OLED regarding current and quantum efficiency can still be achieved based on the above study. As shown in Fig. 5.21, high efficiency inverted top-emitting were fabricated with comparable current efficiency with a highly efficient non-inverted device, which is the best inverted devices reported in literature.

5.5 Conclusions

It has been shown that inverted top-emitting OLEDs have inferior electrical properties than their non-inverted counterparts. In contrast to the case of non-inverted OLEDs, the influence of contact materials on the electrical properties of inverted devices can not be neglected. By investigating hole and electron injection by single carrier device structures, it is found that the higher operating voltage of inverted OLEDs compared to non-inverted devices is mainly due to injection problems of both holes and electrons from respective electrodes in inverted devices. As demonstrated by dynamic XPS and LDI-TOF-MS data analysis, the injection problem is not due to the oxidation or contamination of the bottom cathode, but rather due to differences between interfaces of metal/organic and organic/metal. Using the single carrier device approach and confirmed by C-f and C-V studies, it is demonstrated that when a top contact is deposited onto an electron transport layer, the underlying layer is modified leading to the formation of gap states, which *facilitate* electron injection. Top contact deposition onto a hole transport layer modifies the underlying layer as well. However, in this case, the modified layer acts as *insulator* for hole injection and transport.

Based on interface studies, very thin injection layers have been used to improve electron injection by trying to intentionally introduce gap states at bottom cathode. The injection layer concept works to a certain extent, but can not overcome the problem completely. Nevertheless, a high efficiency inverted top-emitting OLED is still demonstrated which shows comparable current efficiency as one of the best non-inverted devices, while still having relatively inferior electrical properties.

Chapter 6

Stability study of top-emitting OLEDs

In this Chapter, the influence of the device structure on the operational stability of non-inverted top-emitting OLEDs at room temperature will be investigated. Stability studies will be first carried out on top-emitting OLEDs with different anode and cathode metals to investigate influences of the electrode material on device lifetime. Then, stabilities of devices with different top cathode (Ag) thickness will be compared and studied. Finally, extremely stable red top-emitting OLEDs having comparable stability to corresponding bottom-emitting devices will be demonstrated.

6.1 Introduction

Similar to the device efficiency, the stability of OLEDs is one of the most important parameters for display and lighting applications. There exist two kinds of stability, namely operational stability (device lifetime) and storage stability (shelf lifetime). It has been already established that the storage instability of an OLED is mainly attributed to the formation and growth of non-emissive sites or dark spots due to pinholes on the top contact, which create pathways for diffusion-controlled moisture and/or oxygen penetration [114, 160]. However, the understanding of OLED degradation under operation (operational stability) is still limited. Especially for top-emitting devices, more research work is needed to investigate the degradation mechanisms and eventually to achieve high device stability.

In addition to the significant influence of moisture and oxygen on device stability which can be overcome by appropriate encapsulation, the intrinsic material properties of the organic layers are crucial for operational lifetime of bottom-emitting OLEDs. This includes material stability against charge carriers and/or excitons [161], thermal stability (morphology stability) of the organic layers against thermal stress, and the

stability of organic/organic and organic/metal interfaces [162] etc. These limiting factors are also valid for top-emitting devices. However, the structural peculiarity of top-emitting OLEDs, which possess thick metal bottom and thin metal top contacts instead of ITO and thick metal top contacts in bottom-emitting devices, is expected to introduce additional limiting factors on the device stability. To date, the lifetime of bottom-emitting OLEDs has been extensively investigated and ultra-stable devices have been reported with lifetimes well above 100,000 h for red and green at an initial luminance of 500 cd/m² and 10000 h for blue at an initial luminance of 200 cd/m² [4, 143]^q. In contrast, the stability of top-emitting OLEDs has remained largely unexplored.

Since all top-emitting devices to be discussed have similar electrical properties, it makes more sense to compare the device stabilities under the same current density than to compare their absolute lifetime values: Due to different optical device structures, the devices have different outcoupling efficiencies, leading to different brightness at the same current density and finally different absolute lifetime although they may have the same device stability. Therefore, all devices were driven at the same current density and the initial luminance of all the devices was normalized to 1. Device stabilities were thus compared without considering their absolute initial luminance. Moreover, the device lifetime was defined as time needed for the normalized luminance to decay to 50% of its initial value (normalized to 1) at a constant current density. For those measurements that did not reach 50% of their initial luminance, a linear extrapolation was used^r.

All lifetime measurements were conducted in air at room temperature. Before lifetime measurements, all samples were encapsulated in a glove box attached to the vacuum system by covering the active device area with cavity glasses and sealing the edges with a two-component epoxy glue.

6.2 Influence of electrode materials on device lifetime

6.2.1 Influence of anode materials

The influence of the anode materials on device lifetime was investigated without considering their impact on the optical device structure and, thus, on the device

^q These are lifetime data of phosphorescent OLEDs. Lifetimes of fluorescent OLEDs are expected to be even longer, especially for blue fluorescent devices.

^r To calculate the absolute lifetime of a device, an exponential extrapolation with a stretched exponential decay function (SED) is preferred. However, the calculation needs a series of data to define parameters experimentally. Readers are referred to Ref. 143 and 163 for details.

efficiency. Blue top-emitting OLEDs using Spiro-Anthracene as emitter were compared. Since Spiro-Anthracene is not a stable material^s, only rough effects of anode on device lifetime can be studied here. All the devices had the following device structure:

Glass substrate/ Anode/ NHT5:NDP2 (4 mol%, 40 nm)/ Spiro-TAD (10 nm)/ Spiro-Anthracene (20 nm)/ Bphen (10 nm)/ Bphen:Cs (30 nm)/ Al (1nm) Au (12 nm)

In the experiment, top-emitting OLEDs based on four different anodes were compared, which were ITO (precoated), Cr (precoated), Cr (as-deposited), and Au (as-deposited).

The electrical properties of the four devices are compared in Fig. 6.1. As already demonstrated in Chapter 4, all devices show comparable J-V characteristics in the OLED operation range because of the doped hole transport layer used. The different leakage currents are mainly due to the roughness of the bottom contacts. However, the device stabilities are considerably different, as shown in Fig. 6.2.

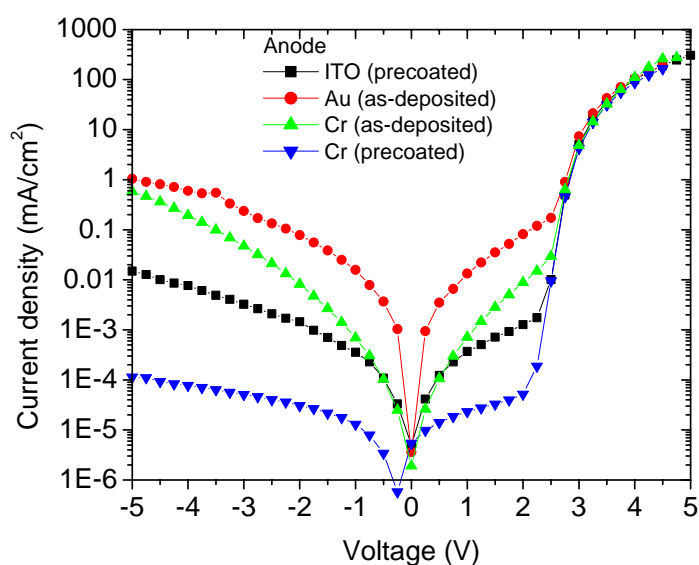


Fig. 6.1. J-V characteristics of top-emitting OLEDs with different anodes.

Fig. 6.2 shows clearly that the devices using ITO and Au as anode have the highest stability, reaching half initial luminance after 48 h, while the device using precoated Cr shows the least stability with a lifetime below 20 h. Consistent with its electroluminescence degradation behavior, the device using precoated Cr shows the most pronounced operation voltage increase. The device based on as-deposited Cr has a better stability (30 h from linear extrapolation) than the precoated Cr device, but its

^s The lifetime of a standard bottom-emitting OLED using Spiro-Anthracene is less than 300 h at an initial luminance of 100 cd/m².

lifetime is still shorter than devices using ITO and Au. In a lifetime study of bottom-emitting OLEDs, it has been reported that mobile ionic impurities initiated by metal diffusion are responsible for device degradation and voltage increase [164, 165]. However, the degradation mechanism by ionic impurities is unlikely in the top-emitting OLEDs discussed here, since Cr has been even used as buffer layer to retard noble metal diffusion in organics [166]. As a reactive metal [167], it is found that Cr always reacts and forms bonds to organics [168]. Thus, the reaction of bottom Cr anode with the hole transport layer is also expected in our devices, which is most likely responsible for the bad stabilities of the devices based on Cr (both precoated and as-deposited Cr).

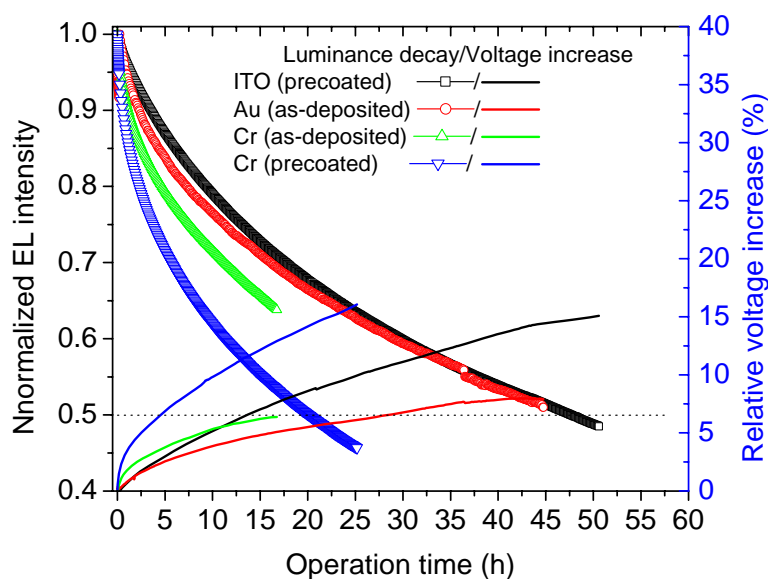


Fig. 6.2. Electroluminescence (EL) degradation (line + symbol, left axis) and corresponding operating voltage increase (line, right axis) of the devices under constant current density of 40 mA/cm^2 .

Since the blue emitter (Spiro-Anthracene) used above is unstable itself, which could also dominate luminance decay, it is desirable to check the influence of the Cr bottom anode on devices using more stable emitters. The red phosphorescent emitter system TMM004:TER004 was thus used [169], with which a standard bottom-emitting OLED showed a lifetime well above 10000 h at an initial luminance of 100 cd/m^2 . Stabilities of two red top-emitting OLEDs were compared, which had the identical device structure but different anode/HTL interfaces with the following device structures:

OLEDs	Anode	HTL	EBL	EML	HBL	ETL	Cathode
Device A	Cr >100 nm	NHT5: NDP2	Spiro-TAD 10 nm	TMM004: TER004 25 wt%, 20 nm	Bphen 10 nm	Bphen: Cs 50 nm	A1/Au 1/12 nm
Device B	Cr/Au >100/2 nm	85 nm					

Table 1. Device structure of two red top-emitting OLEDs with different anode.

Precoated Cr substrates were used in both the devices, having different anode/HTL interfaces: In device A, the HTL is directly contacted with Cr while for device B, additional 2 nm Au were introduced in between Cr and the HTL. Fig. 6.3 shows clearly that with additional 2 nm Au, device B has a much better stability than device A: At the current density of 60 mA/cm^2 , the Cr device (device A) reaches half initial luminance after 178 h, while the CrAu (device B) device has a much better stability reaching half initial luminance after 482 h[†]. The results confirm the conclusion made above that the anode material has a large influence on the device stability and that the reaction of the bottom Cr anode with the HTL leads to a reduced device stability.

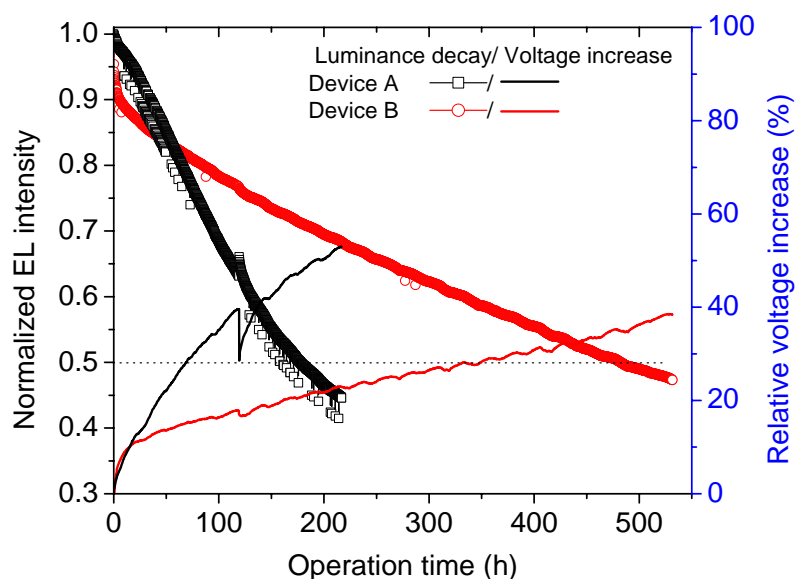


Fig. 6.3. Electroluminescence degradation (line + symbol, left axis) and corresponding operating voltage increase (line, right axis) of the devices under constant current density of 60 mA/cm^2 . Device A: without Au interlayer; Device B: with Au interlayer.

[†] At an initial luminance of 100 cd/m^2 , the estimated absolute lifetime (linearly extrapolation) of the OLEDs on Cr and CrAu are 2775 h and 8778 h, respectively.

6.2.2 Influence of cathode materials

It is expected that the choice of top cathodes will also have large influence on the device stability since the evaporation of metal onto organic layers may lead to metal diffusion into the organics or reactions with the underlying layers. Red top-emitting OLEDs using TMM004:TER004 as emitter system were compared to study the influence of the cathode material, which had the following device structure:

Glass substrate/ Cr (precoated)/ NHT5:NDP2 (4 mol%, 85 nm)/ Spiro-TAD (10 nm)/ TMM004:TER004 (20 wt%, 20 nm)/ Bphen (10 nm)/ Bphen:Cs (50 nm)/ Cathode

Different cathodes were used, including Ag 15 nm (Ag), Al 1 nm Ag 10 nm (AlAg), Al 1 nm Au 10 nm (AlAu) and Au 10 nm (Au). The electrical properties of these four devices are compared in Fig. 6.4.

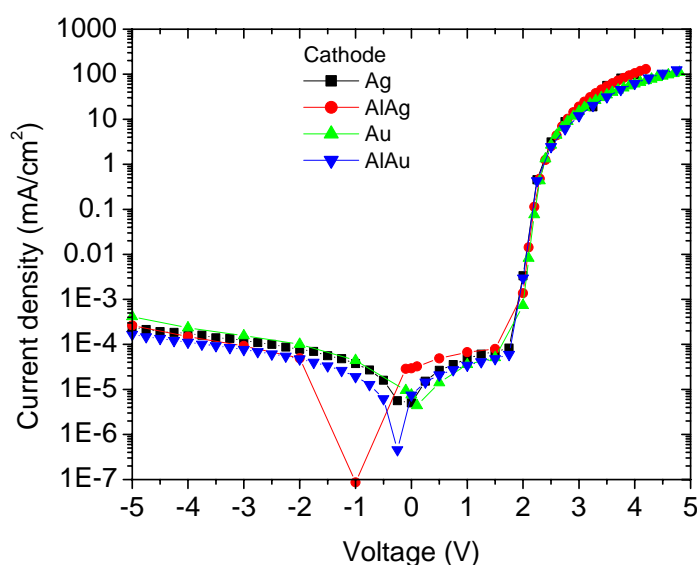


Fig. 6.4. J-V characteristics of top-emitting OLEDs with different cathodes.

All devices show comparable J-V characteristics, even the device using high work function Au as cathode, which is due to the n doped ETL. However, these devices show different stability (see Fig. 6.5). The Ag device shows the least stability with a lifetime of only 84.5 h. Consistent with the fastest degradation, the Ag device has the most pronounced increase of driving voltage with lifetime measurement. By introducing 1 nm Al at the Ag/n-ETL interface, the device lifetime (AlAg) is improved significantly by almost a factor of two, reaching 150 h with small voltage increase. On the other hand, the device using Au as top cathode shows similar stability as the AlAg device. Upon insertion of additional 1 nm Al (AlAu), the stability of the device remains unchanged (125 h). All this indicates that a direct contact of Ag with the ETL causes problems regarding device stability, which are believed to be due to

diffusion of Ag into the organic stack [166, 170]. It is also suggested that a very thin Al film (around 1 nm) can retard this diffusion effectively, which agrees with the research results of other groups on noble metal diffusion in organics [166]. It is known that 1 nm of Al does not form closed layer on any organic material. Thus, the retardation of Ag diffusion may be explained differently: Al is a very reactive metal and is expected to react with organics at the metal/organic interface. The reaction results in a very fine dispersion of Al atoms at the interface, which act as effective traps to Ag atoms arriving followed by self-aggregation of Ag atoms at the interface. As a result, there is no isolated Ag atom in the ETL and, thus, no Ag atom diffusion under external electric field during lifetime measurement [166].

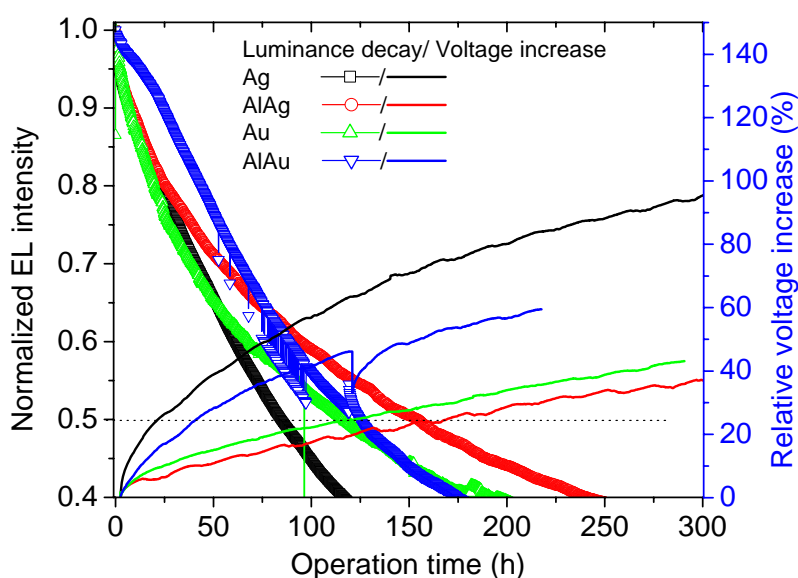


Fig. 6.5. Electroluminescence degradation (line + symbol, left axis) and corresponding operation voltage increase (line, right axis) of the devices with different cathodes under constant current density of 50 mA/cm^2 .

6.3 Influence of Ag top contact thickness on device stability

To achieve maximum light outcoupling from the top contact, usually very thin metal layers (around 15 nm) are used as top contact in a top-emitting OLED. Such thin metals layer may cause stability problems in top-emitting OLEDs. Therefore, the stability of four OLEDs with different Ag top contact thickness was studied. In order to have light coupled out from all samples (even from such samples with very thick metal top contact), all devices were built on ITO instead of metal substrates with the following structure:

Glass substrate/ ITO (90 nm)/ NHT5:NDP2 (1.5 mol%, 55 nm)/ NPD (10 nm)/ NPD: Ir(piq)₃ (20 wt%, 20 nm)/ BAlq (10 nm)/ Bphen:Cs (40 nm)/ Ag (thickness variation)

Four different top cathode thicknesses were tested, which were 15 nm, 30 nm, 60 nm, and 90 nm. The luminance degradation of all samples was measured in bottom emission. Fig 6.6 shows the luminance degradation and the relative operating voltage increase of all four devices. The device using a 15 nm Ag top contact exhibits a very short lifetime, reaching half luminance after 400 h. By increasing the thickness of the top contact to 30 nm, the device lifetime is increased dramatically by a factor of 5, reaching a lifetime of 2000 h. By further increasing the top contact thickness, however, the device lifetime cannot be improved anymore. Although there is no direct evidence, the device stability improvement by increasing the top contact thickness from 15 nm to 30 nm can be explained tentatively as follows: Because Ag normally forms large clusters with low cluster density at the organic/metal interface [171], it is expected that 15 nm Ag on organic is not a densely packed film, which leads to residual moisture and oxygen penetration. With the increase of Ag thickness (for example to 30 nm), a closed layer is formed so that moisture and oxygen penetration can be inhibited and, hence, the device stability is improved [172]. There is no substantial increase of device stability by a further increase of Ag thickness.

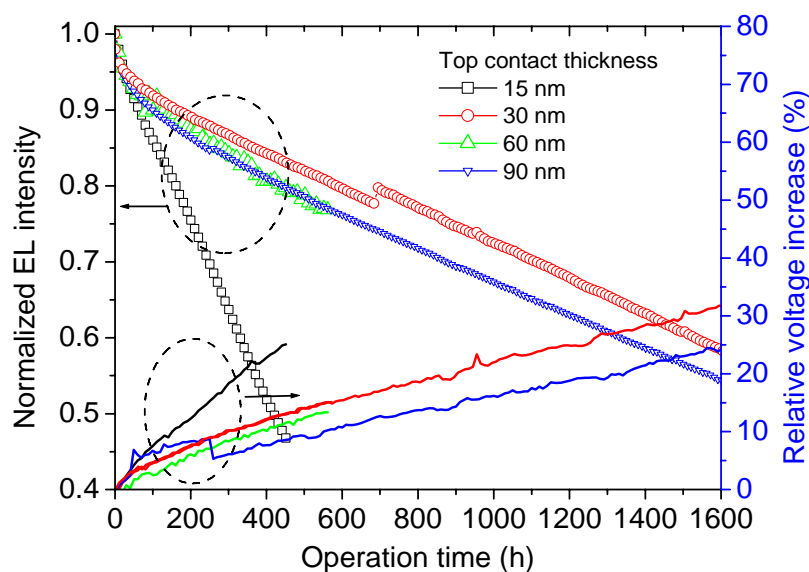


Fig. 6.6. Electroluminescence degradation (line + symbol, left axis) and corresponding operation voltage increase (line, right axis) of the devices with different cathode thickness under constant current density of 30 mA/cm^2 .

6.4 Ultra-stable red top-emitting OLEDs

Unfortunately, it is impossible to improve the stability of a top-emitting OLED by increasing its top contact thickness. If a metal such as Ag is used as top contact, a thick metal layer would compromise the device efficiency due to its large absorption

loss. On the other hand, if a transparent conductive oxide such as ITO is used as top contact, the absorption loss can be reduced, but since it needs sputtering deposition, this would deteriorate the electrical device properties and, eventually, the device efficiency.

In Section 6.2.2, it was demonstrated that 1 nm Al can effectively retard Ag diffusion into the device due to trapping of Ag atoms by finely dispersed Al atoms. The trapping of Ag is expected to result in smaller Ag clusters with a high cluster density and, thus, forming a densely packed Ag film even at low thickness. Therefore, it is expected that the introduction of a thin Al buffer layer can not only retard the Ag diffusion, but also inhibit moisture and oxygen diffusion. The mechanism is indirectly confirmed by comparing device lifetimes of three kinds of top-emitting OLEDs to the stability of an ultra-stable bottom-emitting OLED reported by our group, which showed a long lifetime around 1.5×10^6 h at 500 cd/m^2 [143]. All top-emitting devices had an identical structure, but different Al buffer layer thickness:

Glass substrate/ ITO (90 nm)/ Ag (50 nm)/ NHT5:NDP2 (1.5 mol%, 55 nm)/ NPD (10 nm)/ NPD: Ir(piq)₃ (20 wt%, 20 nm)/ BALq (10 nm)/ Bphen:Cs (40 nm)/ Al (0-3 nm)/ Ag (15 nm)

The thickness of the Al buffer layer was 0, 1, and 3 nm, respectively. The stability of these devices is compared in Fig. 6.7 with the stability of a standard bottom-emitting OLED as reference.

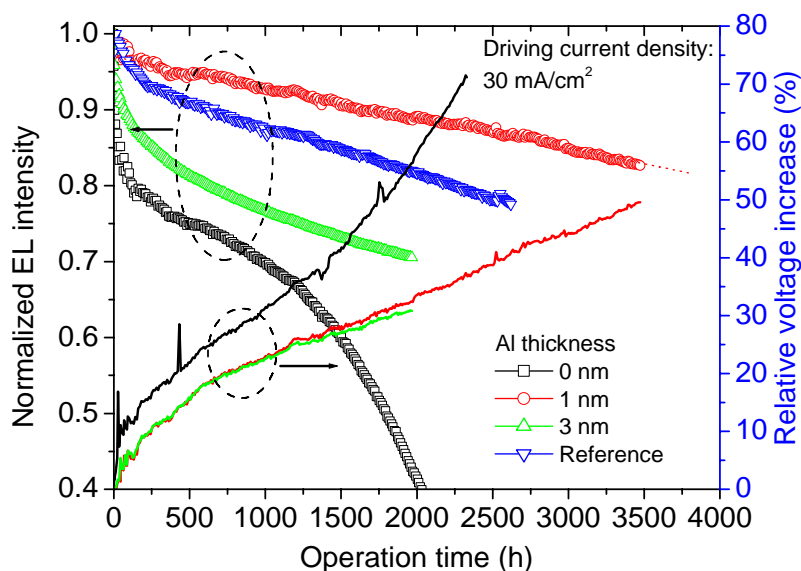


Fig. 6.7. Electroluminescence degradation (line + symbol, left axis) and corresponding operation voltage increase (line, right axis) of the devices with different Al buffer layer thickness under constant current density of 30 mA/cm^2 .

As shown in Fig. 6.7, the device without Al buffer layer (black curve) shows a

drastic luminance drop within the first 150 h, which is assumed to be mainly due to Ag diffusion. Then, a slow degradation is found, which is assigned to annihilation of the emissive centers [163]. After 1200 h, another luminance drop begins with a faster increase of operation voltage, which indicates that device degradation is mainly due to moisture and oxygen diffusion. As expected, the device having additional 1 nm Al (red curve) has much better stability showing no obvious luminance drop, which is completely different from that without Al layer. It is clearly seen that the device stability is even slightly better than the reference bottom OLED having ITO and Al (>100 nm) as bottom and top contact, respectively [143]. By further increasing the Al thickness to 3 nm, there is no improvement of device lifetime (green curve) but rather a decrease. The comparison of stability in Fig. 6.7 suggests that a 1 nm Al buffer layer is already thick enough to obtain very stable top-emitting OLEDs, although the total top contact thickness is as thin as 16 nm.

It is clearly shown in the figure that the top-emitting OLED with 1 nm Al buffer layer has even better stability than the reference bottom device that has a reported lifetime around 1.5×10^6 h at 500 cd/m^2 [143]. Therefore, it is expected that a top-emitting OLED can also have an absolute lifetime above 1 million hours. However, since the top-emitting OLED studied here has a current efficiency of only 2 cd/A at a current density of 30 mA/cm^2 due to its deep red emission (electroluminescence peak wavelength at 690 nm), the absolute device lifetime is much lower than its bottom-emitting counterpart. Nevertheless, the top-emitting device still shows a very long lifetime around 14 000 h when extrapolated linearly at an initial luminance of 500 cd/m^2 .

6.5 Conclusions

It has been shown that both the bottom and the top contact of a top-emitting OLED may have a large influence on the device stability: A top-emitting device using Cr as bottom contact shows much shorter operational lifetime than devices based on other conductors (ITO, Au, and Ag). This reduction of lifetime is tentatively attributed to the reaction of Cr with the HTL. On the other hand, a top-emitting OLED using Ag directly as top contact shows also a bad stability, which is assumed to be due to Ag diffusion as well as to residual moisture and oxygen penetration through the thin top contact. Moreover, it has been demonstrated that an Al buffer layer as thin as 1 nm can be used to significantly improve the device lifetime, which is explained as follows: Deposited Al atoms act as trap for subsequent Ag atoms leading to a densely packed Ag film even at low thickness. As a consequence, Ag diffusion in the HTL is effectively retarded and moisture and oxygen penetration is inhibited.

All the explanations given above are tentatively only. To have direct evidence of the assumed metal diffusion, reaction, and moisture and oxygen penetration during lifetime measurements, other technologies for interface study and surface analysis, and element diffusions have to be used. Nevertheless, an ultra-stable top-emitting OLED with Al buffer layer has been demonstrated which has an even better stability than a corresponding bottom-emitting device.

Chapter 7

Summary and outlook

7.1 Summary

In this work, high efficiency top-emitting OLEDs have been achieved with external quantum efficiencies reaching 15% (phosphorescent red), 20% (phosphorescent green), and 5% (fluorescent blue) at a luminance of 1000 cd/m², which are comparable or even better than corresponding bottom-emitting devices and represent the world best results yet reported. The excellent performance of the devices is mainly attributed to the following two factors:

1. Doped transport layers

In addition to reducing device operation voltage reported before, the use of doped transport layers allows optimizing the electrical and optical properties of top-emitting OLEDs simultaneously.

2. Outcoupling enhancement by a capping layer

It has been demonstrated that both the current efficiency in forward direction and the external quantum efficiency of the device can be improved significantly by an additional capping layer. This improvement is attributed basically to the enhancement of the device outcoupling efficiency due to the modification of the optical device structure by this capping layer, which produces a microcavity enhancement effect while minimizing the absorption.

In addition, we have demonstrated that the efficiency of top-emitting OLEDs can be much higher than corresponding bottom-emitting OLEDs even at similar outcoupling efficiency: Due to enhanced intrinsic quantum yield as the result of shorter triplet exciton lifetime and comparable radiative and non-radiative recombination rates, red top-emitting OLEDs showed a significantly higher external quantum efficiency (more than +35%) than the red bottom-emitting OLEDs. It was

also demonstrated that the decrease of triplet lifetime results in reduced bimolecular quenching processes, especially in the high current density range.

Inverted top-emitting OLEDs were also studied in the work. It has been shown that inverted top-emitting OLEDs have relatively poor electrical properties compared to their non-inverted counterparts, which is mainly attributed to the rather poor injection of both holes and electrons from respective electrodes in inverted devices. Using the single carrier device approach and confirmed by C-f and C-V studies, it has been demonstrated that, when a top contact is deposited onto an electron transport layer, the underlying electron transport layer is modified, leading to the formation of gap states, which *facilitate* electron injection. It was found that top contact deposition onto a hole transport layer modifies the underlying HTL as well. However, in this case, the damaged layer acts as *insulator* for hole injection and transport. A high efficiency inverted top-emitting OLED was still demonstrated which shows comparable current efficiency as one of the best non-inverted devices, while still having inferior electrical properties.

Finally, stabilities of top-emitting OLEDs were studied. It has been shown that both the bottom and top contact of a top-emitting OLED have a large influence on the device stability, which is tentatively attributed to reaction of the metal contact with the adjacent organic layer or metal diffusion in the device. Moreover, it has been demonstrated that an Al buffer layer as thin as 1 nm can be used to significantly improve the device lifetime, which was explained as follow: Deposited Al atoms act as trap for subsequent Ag atoms. As a consequence, Ag diffusion in the HTL is effectively retarded and moisture and oxygen penetration is inhibited. Based on these studies, an ultra stable top-emitting OLED with Al buffer layer was demonstrated which has an even better stability than a corresponding bottom-emitting device.

7.2 Outlook

From the single carrier device approach, it was demonstrated that there is a large difference of charge carrier injection capability between a metal-on-organic and an organic-on-metal contact. The difference was attributed to modification of underlying organics during hot metal atom deposition, which was confirmed by LDI-TOF-MS experiment. However, for a deeper understanding of these metal/organic interfaces, it is obvious that further detailed interface studies such as UPS and XPS are helpful.

In addition, C-V and C-f measurements were used in this work to study charge carrier injection in single carrier devices. It is also possible to obtain the thickness of modified region in single carrier devices if more extensive C-V and C-f measurements are carried out.

In the lifetime study of top-emitting OLEDs, the influence of both anode and cathode as well as top contact thickness on device stability was explained based on metal diffusion, reaction, or residual moisture and oxygen penetration. Although ultrastable top-emitting OLEDs have been achieved based on these studies, all explanations given above are tentatively only without direct evidences. Therefore, other technologies regarding interface study, surface analysis, and element diffusions have to be used. Moreover, it was found that the luminance intensity of some top-emitting OLEDs increased with aging, which is an abnormal phenomenon rarely found in corresponding bottom-emitting OLEDs. It is obvious that the peculiar structure of top-emitting over bottom-emitting OLEDs leads to such a phenomenon. To explain this, more extensive studies on lifetime of top-emitting OLEDs are necessary.

Bibliography

- [1] C. W. Tang and S. A. Van Slyke, *Appl. Phys. Lett.* **51**, 913 (1987).
- [2] R. M. A. Dawson, Z. Shen, D. A. Furst, S. Connor, J. Hsu, M. G. Kane, R. G. Stewart, A. Ipri, C. S. King, P. J. Green, R. T. Flegal, S. Pearson, W. A. Barrow, E. Dickey, K. Ping, C. W. Tang, S. A. VanSlyke, F. Chen, J. Shi, J. C. Sturm, and M. H. Lu, 1998 Society for Information Display (SID) International Symposium, *Digest of Technical Papers*, p. 11 (Anaheim, CA, 1998).
- [3] J. Y. Lee, J. H. Kwon, and H. K. Chung, *Org. Electron.* **4**, 143 (2003).
- [4] www.universaldisplay.com.
- [5] S. A. Van Slyke, C. H. Chen, and C. W. Tang, *Appl. Phys. Lett.* **69**, 2160 (1996).
- [6] G. W. Jones, 2001 Society for Information Display (SID) International Symposium, *Digest of Technical Papers*, p. 134 (San Jose, CA, 2001).
- [7] V. Bulović, G. Gu, P. E. Burrows, S. R. Forrest, and M. E. Thompson, *Nature* **380**, 29 (1996).
- [8] G. Gu, V. Bulovic, P. E. Burrows, S. R. Forrest, and M. E. Thompson, *Appl. Phys. Lett.* **68**, 2606 (1996).
- [9] G. Parthasarathy, P. E. Burrows, V. Khalfin, V. G. Kozlov, and S. R. Forrest, *Appl. Phys. Lett.* **72**, 2138 (1998).
- [10] L. S. Hung and C. W. Tang, *Appl. Phys. Lett.* **74**, 3209 (1999).
- [11] G. Parthasarathy, C. Adachi, P. E. Burrows, and S. R. Forrest, *Appl. Phys. Lett.* **76**, 2128 (2000).
- [12] A. Yamamori, S. Hayashi, T. Koyama, and Y. Taniguchi, *Appl. Phys. Lett.* **78**, 3343 (2001).
- [13] T. Oyamada, H. Yoshizaki, H. Sasabe, and C. Adachi, *Chem. Lett.* **33**, 1034 (2004).
- [14] L. S. Hung and J. Madathil, *Thin Solid Films* **410**, 101 (2002).
- [15] C. H. Chung, Y. W. Ko, Y. H. Kim, C. Y. Sohn, H. Y. Chu, and J. H. Lee, *Appl. Phys. Lett.* **86**, 093504 (2005).
- [16] H. K. Kim, D. G. Kim, K. S. Lee, M. S. Huh, S. H. Jeong, K. I. Kim, and T. Y. Seong, *Appl. Phys. Lett.* **86**, 183503 (2005).
- [17] M. H. Lu, M. S. Weaver, T. X. Zhou, M. Rothman, R. C. Kwong, M. Hack, and J. J. Brown, *Appl. Phys. Lett.* **81**, 3921 (2002).
- [18] T. Tsutsui, M. J. Yang, M. Yahiro, K. Nakamura, T. Watanabe, T. Tsuji, Y. Fukuda, T. Wakimoto, and S. Miyaguchi, *Jpn. J. Appl. Phys.* **38**, L1502 (1999).
- [19] L. S. Hung, C. W. Tang, M. G. Mason, P. Raychaudhuri, and J. Madathil, *Appl. Phys. Lett.* **78**, 544 (2001).

- [20] H. Riel, S. Karg, T. Beierlein, B. Ruhstaller, and W. Rieß, *Appl. Phys. Lett.* **82**, 466 (2003).
- [21] V. Bulović, P. Tian, P. E. Burrows, M. R. Gokhale, S. R. Forrest, and M. E. Thompson, *Appl. Phys. Lett.* **70**, 2954 (1997).
- [22] X. Zhou, M. Pfeiffer, J. S. Huang, J. Blochwitz-Nimoth, D. S. Qin, A. Werner, J. Drechsel, B. Maennig, and K. Leo, *Appl. Phys. Lett.* **81**, 922 (2002).
- [23] H. W. Choi, S. Y. Kim, W. K. Kim, and J. L. Lee, *Appl. Phys. Lett.* **87**, 082102 (2005).
- [24] M. Pope and C. E. Swenberg, *Electronic Processes in Organic Crystals and Polymers*, 2nd Ed., Oxford University Press, New York 1999.
- [25] R. Farchioni and G. Grosso (Eds.), *Organic Electronic Materials*, Springer, Heidelberg 2001.
- [26] <http://library.thinkquest.org/3659/structures/delocalizedorbitals.html>
- [27] P. Peumans, *Organic thin-film photodiodes*, PhD thesis, Princeton University 2004.
- [28] W. Brütting, *Physics of Organic Semiconductors*, Wiley-VCH, Berlin 2005.
- [29] C. Adachi, M. A. Baldo, M. E. Thompson, and S. R. Forrest, *J. Appl. Phys.* **90**, 5048 (2001).
- [30] M. A. Baldo, M. E. Thompson, and S. R. Forrest, *Nature* **403**, 750 (2000).
- [31] E. A. Silinsh, *Organic molecular crystals, their electronic states*, *Solid-State Science 16*, Springer, Heidelberg 1980.
- [32] M. Pfeiffer, *Controlled doping of organic vacuum deposited dye layers: basics and applications*, PhD thesis, Technische Universität Dresden 1999.
- [33] N. Karl, *Synth. Met.* **133-134**, 649 (2003).
- [34] N. Karl, J. Marktanner, R. Stehle, and W. Warta, *Synth. Met.* **42**, 2473 (1991).
- [35] H. Bässler, *Phys. Status Solidi B* **175**, 15 (1993).
- [36] J. Staudigel, M. Stöbel, F. Steuber, and J. Simmerer, *J. Appl. Phys.* **86**, 3895 (1999).
- [37] W. Brütting, S. Berleb, and A. G. Mückl, *Synth. Met.* **122**, 99 (2001).
- [38] A. Ioannidis, E. Forsythe, Y. L. Gao, M. W. Wu, and E. M. Conwell, *Appl. Phys. Lett.* **72**, 3038 (1998).
- [39] U. Wolf, H. Bässler, P. M. Borsenberger, and W. T. Gruenbaum, *Chem. Phys.* **222**, 259 (1997).
- [40] V. I. Arkhipov, P. Heremans, E. V. Emelianova, G. J. Adriaenssens, and H. Bässler, *Appl. Phys. Lett.* **82**, 3245 (2003).
- [41] M. C. J. M. Vissenberg and M. Matters, *Phys. Rev. B* **57**, 12964 (1998).
- [42] B. Maennig, M. Pfeiffer, A. Nollau, X. Zhou, P. Simon, and K. Leo, *Phys. Rev. B* **64**, 195208 (2001).

- [43] A. Kahn, W. Zhao, W. Y. Gao, H. Vázquez, and F. Flores, *Chem. Phys.* **325**, 129 (2006).
- [44] G. G. Malliaras and J. C. Scott, *J. Appl. Phys.* **83**, 5399 (1998).
- [45] S. A. Carter, M. Angelopoulos, S. Karg, P. J. Brock, and J. C. Scott, *Appl. Phys. Lett.* **70**, 2067 (1997).
- [46] W. R. Salaneck, K. Seki, A. Kahn, and J. J. Pireaux (Eds.), *Conjugated Polymer and Molecular Interfaces*, Marcel Dekker, New York 2001.
- [47] C. Shen and A. Kahn, *Org. Electron.* **2**, 89 (2001).
- [48] I. G. Hill, J. Schwartz, and A. Kahn, *Org. Electron.* **1**, 5 (2000).
- [49] P. S. Bagus, V. Staemmler, and C. Wöll, *Phys. Rev. Lett.* **89**, 096104 (2002).
- [50] H. Vazquez, F. Flores, R. Oszwaldowski, J. Ortega, R. Perez, and A. Kahn, *Appl. Surf. Sci.* **234**, 107 (2004).
- [51] S. M. Sze, *Physics of Semiconductor Devices*, 2nd Ed. Wiley, New York 1981.
- [52] M. Abkowitz, J. S. Facci, and J. Rehm, *J. Appl. Phys.* **83**, 2670 (1998).
- [53] V. E. Choong, M. G. Mason, C. W. Tang, and Y. L. Gao, *Appl. Phys. Lett.* **72**, 2689 (1998).
- [54] H. Ishii, K. Sugiyama, E. Ito, and K. Seki, *Adv. Mater.* **11**, 605 (1999).
- [55] L. Y. Shen, M. W. Klein, D. B. Jacobs, J. C. Scott, and G. G. Malliaras, *Phys. Rev. Lett.* **86**, 3867 (2001).
- [56] M. Abkowitz, H. A. Mizes, and J.S. Facci, *Appl. Phys. Lett.* **66**, 1288 (1995).
- [57] U. Wolf and H. Bässler, *Appl. Phys. Lett.* **74**, 3848 (1999).
- [58] F. Kozłowski, *Numerical simulation and optimisation of organic light emitting diodes and photovoltaic cells*, PhD thesis, Technische Universität Dresden 2005.
- [59] G. G. Malliaras and J. C. Scott, *J. Appl. Phys.*, **85**, 7426 (1999).
- [60] M. A. Lambert and P. Mark, *Current Injection in Solids*, New York: Academic, 1970.
- [61] K. C. Kao and W. Hwang, *Electrical Transport in Solids*, Pergamon press, Oxford 1981.
- [62] P. E. Burrows, Z. Shen, V. Bulovic, D. M. McCarty, S. R. Forrest, J. A. Cronin, and M. E. Thompson, *J. Appl. Phys.* **79**, 7991 (1996).
- [63] M. Segal, M. A. Baldo, R. J. Holmes, S. R. Forrest, and Z. G. Soos, *Phys. Rev. B* **68**, 075211 (2003).
- [64] W. Helfrich, *Physic and Chemistry of the Organic Solid State*, Wiley-Interscience, New York 1967.
- [65] M. K. Lee, M. Segal, Z. G. Soos, J. Shinar, and M. A. Baldo, *Phys. Rev. Lett.* **94**, 137403 (2005).
- [66] K. Okumoto, H. Kanno, Y. Hamaa, H. Takahashi, and K. Shibata, *Appl. Phys. Lett.* **89**, 063504 (2006).

- [67] Y. Cao, I. D. Parker, G. Yu, C. Zhang, and A. J. Heeger, *Nature* **397**, 414 (1999).
- [68] M. Wohlgenannt, K. Tandon, S. Mazumdar, S. Ramasesha, and Z.V. Vardeny, *Nature* **409**, 494 (2001).
- [69] J. S. Wilson, A. S. Dhoot, A. J. A. B. Seeley, M. S. Khan, A. Köhler, and R. H. Friend, *Nature* **413**, 828 (2001).
- [70] Y. Wu, Y. C. Zhou, H. R. Wu, Y. Q. Zhan, J. Zhou, S. T. Zhang, J. M. Zhao, Z. J. Wang, X. M. Ding, and X. Y. Hou, *Appl. Phys. Lett.* **87**, 044104 (2005).
- [71] M. A. Baldo and S. R. Forrest, *Phys. Rev. B* **62**, 10958 (2000).
- [72] P. Andrew and W. L. Barnes, *Science* **290**, 785 (2000).
- [73] C. W. Tang, S. A. VanSlyke, and C. H. Chen, *J. Appl. Phys.* **65**, 3610 (1989).
- [74] J. M. Shi and C. W. Tang, *Appl. Phys. Lett.* **70**, 1665 (1997).
- [75] J. S. Kim, P. K. H. Ho, N. C. Greenham, and R. H. Friend, *J. Appl. Phys.* **88**, 1073 (2000).
- [76] M. H. Lu and J. C. Sturm, *J. Appl. Phys.* **91**, 595 (2002).
- [77] L. H. Smith, J. A. E. Wasey, and W. L. Barnes, *Appl. Phys. Lett.* **84**, 2986 (2004).
- [78] R. H. Jordan, L. J. Rothberg, A. Dodabalapur, and R. E. Slusher, *Appl. Phys. Lett.* **69**, 1997 (1996).
- [79] A. Dodabalapur, L. J. Rothberg, R. H. Jordan, T. M. Miller, R. E. Slusher, and J. M. Philips, *J. Appl. Phys.* **80**, 6954 (1996).
- [80] T. Tsutsui, M. Yahiro, H. Yokogawa, K. Kawano, and M. Yokoyama, *Adv. Mater.* **13**, 1149 (2001).
- [81] H. J. Peng, Y. L. Ho, X. J. Xu, and H. S. Kwok, *J. Appl. Phys.* **96**, 1649 (2004).
- [82] G. Gu, D. Z. Garbuzov, P. E. Burrows, S. Venkatesh, S. R. Forrest, and M. E. Thompson, *Opt. Lett.* **22**, 396 (1997).
- [83] C. F. Madigan, M. H. Lu, and J. C. Sturm, *Appl. Phys. Lett.* **76**, 1650 (2000).
- [84] S. Möller and S. R. Forrest, *J. Appl. Phys.* **91**, 3324 (2002).
- [85] J. J. Shiang, T. J. Faircloth, and A. R. Duggal, *J. Appl. Phys.* **95**, 2889 (2004).
- [86] C. C. Wu, C. L. Lin, P. Y. Hsieh, and H. H. Chiang, *Appl. Phys. Lett.* **84**, 3966 (2004).
- [87] C. L. Lin, H. W. Lin, and C. C. Wu, *Appl. Phys. Lett.* **87**, 021101 (2005).
- [88] S. R. Forrest, D. D. C. Bradley, and M. E. Thompson, *Adv. Mater.* **15**, 1043 (2003).
- [89] I. Tanaka and S. Tokito, *Jpn. J. Appl. Phys.* **43**, 7733 (2004).
- [90] S. Okamoto, K. Tanaka, Y. Izumi, H. Adachi, T. Yamaji, and T. Suzuki, *Jpn. J. Appl. Phys.* **40**, L783 (2001).
- [91] H. J. Peng, *Design and fabrication of high efficiency organic light emitting diodes*, PhD thesis, Hong Kong University of Science and Technology 2005.

- [92] V. Bulović, V. B. Khalfin, G. Gu, P. E. Burrows, D. Z. Garbuzov, and S. R. Forrest, *Phys. Rev. B* **58**, 3730 (1998).
- [93] S. K. So, W. K. Choi, L. M. Leung, and K. Neyts, *Appl. Phys. Lett.* **74**, 1939 (1999).
- [94] K. Neyts, P. De Visschere, D. K. Fork, and G. B. Anderson, *J. Opt. Soc. Am. B* **17**, 114 (2000).
- [95] A. Yariv, *Quantum Electronics*, 2nd Ed., Wiley, New York 1975.
- [96] A. Chin and T. Y. Chang, *J. Lightwave Technol.* **9**, 321 (1991).
- [97] E. F. Schubert, N. E. J. Hunt, M. Micovic, R. J. Malik, D. L. Sivco, A. Y. Cho, and G. J. Zydzik, *Science* **265**, 943 (1994).
- [98] C. W. Chen, P. Y. Hsieh, H. H. Chiang, C. L. Lin, H. M. Wu, and C. C. Wu, *Appl. Phys. Lett.* **83**, 5127 (2003).
- [99] G. G. Qin, A. G. Xu, G. L. Ma, G. Z. Ran, Y. P. Qiao, B. R. Zhang, W. X. Chen, and S. K. Wu, *Appl. Phys. Lett.* **85**, 5406 (2004).
- [100] H. Riel, S. Karg, T. Beierlein, W. Rieß, and K. Neyts, *J. Appl. Phys.* **94**, 5290 (2003).
- [101] C. C. Wu, C. L. Lin, P. Y. Hsieh, and H. H. Chiang, *Appl. Phys. Lett.* **84**, 3966 (2004).
- [102] P. K. Raychaudhuri, J. K. Madathil, J. D. Shore, and S. A. Van Slyke, *Journal of the Society for Information Display* **12/3**, 315 (2004).
- [103] Y. Q. Li, J. X. Tang, Z. Y. Xie, L. S. Hung, and S. S. Lau, *Chem. Phys. Lett.* **386**, 128 (2004).
- [104] C. F. Qiu, H. J. Peng, H. Y. Chen, Z. L. Xie, M. Wong, and H. S. Kwok, *IEEE T. Electron. Dev.* **51**, 1207 (2004).
- [105] J. Blochwitz, T. Fritz, M. Pfeiffer, and K. Leo, *Org. Electron.* **2**, 97 (2001).
- [106] J. S. Huang, M. Pfeiffer, A. Werner, J. Blochwitz, S. Y. Liu, and K. Leo, *Appl. Phys. Lett.* **80**, 139 (2002).
- [107] M. Pfeiffer, S. R. Forrest, K. Leo, and M. E. Thompson, *Adv. Mater.* **14**, 1633 (2002).
- [108] X. Zhou, M. Pfeiffer, J. S. Huang, J. Blochwitz-Nimoth, D. S. Qin, A. Werner, J. Drechsel, B. Maennig, and K. Leo, *Appl. Phys. Lett.* **81**, 922 (2002).
- [109] G. F. He, M. Pfeiffer, K. Leo, M. Hofmann, J. Birnstock, R. Pudzich, and J. Salbeck, *Appl. Phys. Lett.* **85**, 3911 (2004).
- [110] D. Gebeyehu, K. Walzer, G. F. He, M. Pfeiffer, K. Leo, J. Brandt, A. Gerhard, P. Stöbel, and H. Vestweber, *Synth. Met.* **148**, 205 (2005).
- [111] S. A. Van Slyke and C. W. Tang, *US patent* 5,061,569 (1991).
- [112] L. S. Hung and C. H. Chen, *Mater. Sci. Eng.* **R39**, 143 (2002).
- [113] Y. Wang, N. Herron, V. V. Grushin, D. LeCloux, and V. Petrov, *Appl. Phys. Lett.*

- 79**, 449 (2001).
- [114] S. Naka, H. Okada, H. Onnagawa, and T. Tsutsui, *Appl. Phys. Lett.* **76**, 197 (2000).
- [115] B. W. D'Andrade, S. R. Forrest, and A. B. Chwang, *Appl. Phys. Lett.* **83**, 3858 (2003).
- [116] R. C. Kwong, M. R. Nugent, L. Michalski, T. Ngo, K. Rajan, Y. J. Tung, M. S. Weaver, T. X. Zhou, M. Hack, M. E. Thompson, S. R. Forrest, and J. J. Brown, *Appl. Phys. Lett.* **81**, 162 (2002).
- [117] Y. Kuwabara, H. Ogawa, and Y. Shirota, *Adv. Mater.* **6**, 677 (1994).
- [118] M. Ikai, S. Tokito, Y. Sakamoto, T. Suzuki, and Y. Taga, *Appl. Phys. Lett.* **79**, 156 (2001).
- [119] Y. T. Tao, E. Balasubramaniam, A. Danel, and P. Tomasik, *Appl. Phys. Lett.* **77**, 933 (2000).
- [120] Y. T. Tao, E. Balasubramaniam, A. Danel, B. Jarosz, and P. Tomasik, *Appl. Phys. Lett.* **77**, 1575 (2000).
- [121] Z. Q. Gao, C. S. Lee, I. Bello, S. T. Lee, R. M. Chen, T. Y. Luh, J. Shi, and C. W. Tang, *Appl. Phys. Lett.* **74**, 865 (1999).
- [122] H. Spreitzer, H. Schenk, J. Salbeck, F. Weissörtel, H. Riel, and W. Rieß, *SPIE Proc.* **3797**, 316 (1999).
- [123] B. Ruhstaller, T. A. Beierlein, H. Riel, S. Karg, J. C. Scott, and W. Rieß, *IEEE J. Sel. Top. Quant.* **9**, 723 (2003).
- [124] www.adsdyes.com.
- [125] M. A. Baldo, S. Lamansky, P. E. Burrows, M. E. Thompson, and S. R. Forrest, *Appl. Phys. Lett.* **75**, 4 (1999).
- [126] C. Adachi, R. C. Kwong, P. Djurovich, V. Adamovich, M. A. Baldo, M. E. Thompson, and S. R. Forrest, *Appl. Phys. Lett.* **79**, 2082 (2001).
- [127] J. Birnstock, M. Hofmann, S. Murano, M. Vehse, J. Blochwitz-Nimoth, Q. Huang, G. F. He, M. Pfeiffer, and K. Leo, 2005 Society for Information Display (SID) International Symposium, *Digest of Technical Papers* **36**, p. 40 (Boston, MA, USA, 2005).
- [128] F. H. Li, *Novel dopants for n-type doping of electron transport materials: Cathionic dye and their bases*, PhD thesis, Technische Universität Dresden 2005.
- [129] J. Drechsel, A. Petrich, M. Koch, S. Pfützner, R. Meerheim, S. Scholz, K. Walzer, M. Pfeiffer, and K. Leo, 2005 Society for Information Display (SID) International Symposium, *Digest of Technical Papers* **37**, p. 1692 (San Francisco, CA, USA, 2005).
- [130] J. R. Macdonald (Eds.), *Impedance Spectroscopy, Emphasizing Solid Materials and Systems*, Wiley, New York 1987.

- [131] J. Drechsel, M. Pfeiffer, X. Zhou, A. Nollau, and K. Leo, *Synth. Met.* **127**, 201 (2002).
- [132] J. Drechsel, B. Männig, D. Gebeyehu, M. Pfeiffer, K. Leo, and H. Hoppe, *Org. Electron.* **5**, 175 (2004).
- [133] S. Berleb and W. Brütting, *Phys. Rev. Lett.* **89**, 286601-1 (2002).
- [134] H. Ishii and K. Seki, *IEEE T. Electron. Dev.* **44**, 1295 (1997).
- [135] J. Blochwitz, *Organic light-emitting diodes with doped charge transport layers*, PhD thesis, Technische Universität Dresden 2001.
- [136] D. J. Milliron, I. G. Hill, C. Shen, A. Kahn, and J. Schwartz, *J. Applied Phys.* **87**, 572 (1999).
- [137] K. B. Kim, Y. H. Tak, Y. S. Han, K. H. Baik, M. H. Yoon, and M. H. Lee, *Jpn. J. Appl. Phys.* **42**, L438 (2003).
- [138] Calculated using emissive thin film optics simulation (ETFOS) software, designed by CCP of Zurich University of Applied Sciences, Winterthur (ZHW).
- [139] C. Adachi, M. A. Baldo, S. R. Forrest, and M. E. Thompson, *Appl. Phys. Lett.* **77**, 904 (2000).
- [140] Y. Kawamura, K. Goushi, J. Brooks, J. J. Brown, H. Sasabe, and C. Adachi, *Appl. Phys. Lett.* **86**, 071104 (2005).
- [141] E. F. Schubert, A. M. Vredenberg, N. E. J. Hunt, Y. H. Wong, P. C. Becker, J. M. Poate, D. C. Jacobson, L. C. Feldman, and G. J. Zydzik, *Appl. Phys. Lett.* **61**, 1381 (1992).
- [142] N. Tessler, S. Burns, H. Becker, and R. H. Friend, *Appl. Phys. Lett.* **70**, 556 (1997).
- [143] R. Meerheim, K. Walzer, M. Pfeiffer, and K. Leo, *Appl. Phys. Lett.* **89**, 061111 (2006).
- [144] J. M. Gérard and B. Gayral, *J. Lightwave Technol.* **17**, 2089 (1999).
- [145] A. Tsuboyama, H. Iwawaki, M. Furugori, T. Mukaide, J. Kamatani, S. Igawa, T. Moriyama, S. Miura, T. Takiguchi, S. Okada, M. Hoshino, and K. Ueno, *J. Am. Chem. Soc.* **125**, 12971 (2003).
- [146] M. A. Baldo, C. Adachi, and S. R. Forrest, *Phys. Rev. B* **62**, 10967 (2000).
- [147] J. Kalinowski, W. Stampor, J. Mezyk, M. Cocchi, D. Virgili, V. Fattori, and P. Di Marco, *Phys. Rev. B* **66**, 235321 (2002).
- [148] S. Reineke, K. Walzer, and K. Leo, *Phys. Rev. B* **75**, 125328 (2007).
- [149] S. Cinà, D. Vaufrey, C. Fery, B. Racine, H. Doyeux, A. Bettinelli, and J. -C. Martinez, 2005 Society for Information Display (SID) International Symposium, *Digest of Technical Papers*, p. 819 (Boston, MA, 2005).
- [150] D. Vaufrey, C. Frey, S. Cinà, C. Prat, J. C. Martinez, and H. Doyeux, Eurodisplay 2005, p. 20 (Edinburgh, Scotland, 2005).

- [151] C. F. Shen, I. G. Hill, and A. Kahn, *Adv. Mater.* **11**, 1523 (1999).
- [152] F. Li, H. Tang, J. Anderegg, and J. Shinar, *Appl. Phys. Lett.* **70**, 1233 (1997).
- [153] S. Scholz, *unpublished*, Institute of Applied photophysics (IAPP), Technische Universität Dresden.
- [154] Y. Hirose, A. Kahn, V. Aristov, P. Soukiassian, V. Bulović and S. R. Forrest, *Phys. Rev. B* **54**, 13748 (1996).
- [155] I. G. Hill, A. Rajagopal, and A. Kahn, *J. Appl. Phys.* **84**, 3236 (1998).
- [156] A. Rajagopal and A. Kahn, *J. Appl. Phys.* **84**, 355 (1998).
- [157] S. Scholz, *unpublished*, Institute of Applied photophysics (IAPP), Technische Universität Dresden.
- [158] B. P. Rand, J. Li, J. G. Xue, R. J. Holmes, M. E. Thompson, and S. R. Forrest, *Adv. Mater.* **17**, 2714 (2005).
- [159] P. Peumans, A. Yakimov, and S. R. Forrest, *J. Appl. Phys.* **93**, 3693 (2003).
- [160] S. F. Lim, W. Wang, and S. J. Chua, *Adv. Funct. Mater.* **12**, 513 (2002).
- [161] G. Sakamoto, C. Adachi, T. Koyama, Y. Taniguchi, C. D. Merritt, H. Murata, Z. H. Kafafi, *Appl. Phys. Lett.* **75**, 766 (1999).
- [162] F. Steuber, J. Staudigel, M. Stössel, J. Simmerer, A. Winnacker, H. Spreitzer, F. Weissörtel, and J. Salbeck, *Adv. Mater.* **12**, 130 (2000).
- [163] C. Féry, B. Racine, D. Vaufrey, H. Doyeux, and S. Cinà, *Appl. Phys. Lett.* **87**, 213502 (2005).
- [164] Y. Hirose, A. Kahn, V. Aristov, and P. Soukiassian, *Appl. Phys. Lett.* **68**, 217 (1996).
- [165] S. T. Lee, Z. Q. Gao, and L. S. Hung, *Appl. Phys. Lett.* **75**, 1404 (1999).
- [166] A. Thran, T. Strunskus, V. Zaporozhchenko, and F. Faupel, *Appl. Phys. Lett.* **81**, 244 (2002).
- [167] H. Shimizu, E. Omori, and M. Ikeda, *Jpn. J. Appl. Phys.* **45**, 4982 (2006).
- [168] T. Strunskus, M. Grunze, G. Kochendoerfer, and Ch. Wöll, *Langmuir* **12**, 2712 (1996).
- [169] H. Becker, H. Vestweber, A. Gerhard, P. Stoessel, and R. Fortte, 2004 Society for Information Display (SID) International Symposium, *Digest of Technical Papers*, p. 796 (Seattle, WA, 2004).
- [170] W. J. Song, S. K. So, J. Moulder, Y. Qiu, Y. F. Zhu, and L. L. Cao, *Surf. Interface Anal.* **32**, 70 (2001).
- [171] F. Faupel, R. Willecke, and A. Thran, *Mater. Sci. Eng. R* **22**, 1 (1998).
- [172] S. M. Jeong, W. H. Koo, S. H. Choi, S. J. Jo, H. K. Baik, S. J. Lee, and K. M. Song, *Appl. Phys. Lett.* **85**, 1051 (2004).

List of symbols

β	Electric field activation parameter of the mobility
δ_B	Barrier height
κ_r	Radiative decay rate
κ_{nr}	Non-radiative decay rate
μ_0	Charge carrier mobility without field
φ_B	Phase shift at the bottom contact
φ_T	Phase shift at the top contact
Ψ	Wavefunction
λ	Wavelength
η_{out}	Outcoupling efficiency
η_{ext}	External quantum efficiency
η_p	Power efficiency
η_C	Current efficiency
η_{int}	Intrinsic quantum yield
τ	Exciton lifetime
ω	Frequency
Φ_0	Total light flux
A	Absorbance
A^*	Richardson constant
c	Velocity of light in vacuum
C_p	Capacitance
D_e	Exciton diffusion constant
E	Energy level
F	Electric field
$g(\lambda)$	Spectral shape function
H	Hamiltonian
h	Planck's constant
J	Current density
k_B	Boltzmann constant
K_{TT}	Rate constant of triplet-triplet annihilation
K_P	Rate constant of triplet-polaron quenching
n_i	Refractive index
$L(\lambda)$	Spectral luminous flux
R	Reflectance
R_p	Resistance
S_1	Lowest singlet excited state
$S(T)$	Seebeck coefficient
T_1	Lowest triplet excited state
T	Absolute temperature
T_g	Glass transition temperature
$V(\lambda)$	Spectral luminous efficiency function
V_m	Mode volume

List of abbreviations

α -Si	Amorphous silicon
AM	Active matrix
CPEs	Constant phase elements
CT	Charge-transfer
DOS	Density of states
EBL	Electron blocking layer
EIL	Electron injection layer
EL	Electroluminescence
EML	Emission layer
EQE	External quantum efficiency
ET	Energy transfer
ETL	Electron transport layer
FPDs	Flat panel displays
FWHM	Full width at half maximum
HBEC	High binding energy cutoff
HBL	Hole blocking layer
HIL	Hole injection layer
HOMO	Highest occupied molecular orbitals
HTL	Hole transport layer
IC	Internal conversion
IDIS	Induced density of interface states
IP	Ionization potential
ISC	Intersystem crossing
LACO	linear combination of atomic orbitals
LDI-TOF-MS	Laser desorption/ionization-time of flight-mass spectrometry
LTPS	Low-temperature polycrystalline silicon
LUMO	Lowest unoccupied molecular orbitals
OLEDs	Organic light-emitting diodes
PL	Photoluminescence
PM	Passive matrix
SCLC	Space charge limited current
TTA	Triplet-triplet annihilation
TPQ	Triplet-polaron quenching
TFT	Thin film transistor
TCLC	Trap charge limited current
UPS	Ultraviolet photoelectron spectroscopy
XPS	X-ray photoelectron spectroscopy

List of compounds

α -NPD	N, N'-di(naphthalen-2-yl)-N, N'-diphenyl-benzidine
BAIq	bis(2-methyl-8-quinolinolato)-(para-phenylphenolato)-aluminium(III)
Bphen	4,7-diphenyl-1,10-phenanthroline
FIrpic	iridium(III) bis[(4,6-difluorophenyl)-pyridinato-N,C2]picolinate
F ₄ -TCNQ	2,3,5,6-tetrafluoro-7,7,8,8-tetracyano-quinodimethane
Ir(piq) ₃	tris(1-phenylisoquinoline)iridium
Ir(ppy) ₃	tris(2-phenylpyridine) iridium
ITO	indium tin oxide
MeO-TPD	N,N,N',N'-tetrakis(4-methoxyphenyl)-benzidine
Spiro-Anthracene	9,10-Bis(9,9'-spirobi[9H-fluorene]-2-yl)anthracene
Spiro-DPVBi	2,2',7,7'-tetrakis(2,2-diphenylvinyl)spiro-9,9'-bifluorene
Spiro-TAD	2,2',7,7'-tetrakis-(N,N-diphenylamino)-9,9'-spirobifluorene
TCTA	4,4',4''-tris(N-carbazolyl)-triphenylamine
TPBI	2,2',2''-(1,3,5-benzenetriyl)tris[1-phenyl-1H-benzimidazole]
ZnPc	zinc-phthalocyanine

Acknowledgements

First of all, I am greatly indebted to my supervisor, Prof. Karl Leo, for providing me the opportunity to do this interesting and challenging work in the Institute für Angewandte Photophysik (IAPP) and giving me constant help and encouragement all the time. His guidance and insight in the field of organic semiconductor and device were essential for my doctoral work.

I am considerably indebted to our former group leader, Dr. Martin Pfeiffer, who is an admirable physicist. Thanks to his guidance, I had the best start I could imagine in my research work. Due to his broad knowledge and deep understanding on organic semiconductor, discussions with him were always intriguing and his ideas, comments and advices were very useful and helpful. I am also indebted to our current group leader Dr. Karsten Walzer for his constant support and help with both scientific and technical problems. His careful reading and corrections of the thesis and other manuscripts are greatly appreciated.

It has been a great pleasure to work with all other members of the OLED group of IAPP, who are talented experimentalists with remarkable experimental and analytical skills: Karsten Feshe, Sebastian Scholz, Rico Meerheim, Gregor Schwartz, Sebastian Reineke, Frank Lindner, Thomas Rosenow, Selina Olthof et al. It is you who made the UFOII lab attractive and discussions during group meetings helpful. In addition, I would like to thank all the members of the OSOL group. It was a great fun to do outdoor activities with you all.

I would also like to thank all other people from IAPP, in particular Maik Koch for the purification of all materials used in this study, Christian Kolberg for technology support in UFOII, Eva Schmidt for her kind help, Kai Schmidt for solving computer problems.

It has been a pleasure to carry out projects together with those from Novald AG: Michael Hofmann, Dr. Thomas Stübinger, Dr. Martin Vehse, Dr. Jan Birnstock, and Dr. Jan Bolchwitz-Nimoth. Thank you for your good cooperation. Two other person from Novald to whom I am also indebted: Philip Wellman and Dr. Gufeng He. Thank you very much Philip and Gufeng. You guys helped me a lot especially during my first several months in Dresden and helped me to get familiar with Germany, IAPP and UFOII.

In addition, all my friends who are still in and have already left Dresden deserve my appreciation. Because of you, the life in Dresden is fantastic.

Of course, without what my parents have done for me, without supports and love from my brothers and sisters, everything I have achieved is not possible. I hope my

PhD work worth all their efforts.

Finally, the thesis is dedicated to my wife Yan, who have given more meaning to my life. Thank you for your endless love and support.

Diese Arbeit wurde unter der Betreuung von Prof. Karl Leo am *Institut für Angewandte Photophysik (IAPP)* der *Technischen Universität Dresden (TU Dresden)* angefertigt.

Versicherung

Hiermit versichere ich, dass ich die vorliegende Arbeit ohne die unzulässige Hilfe Dritter und ohne Benutzung anderer als der angegebenen Hilfsmittel angefertigt habe; die aus fremden Quellen direkt oder indirekt übernommenen Gedanken sind als solche kenntlich gemacht. Die Arbeit wurde bisher weder im Inland noch im Ausland in gleicher oder ähnlicher Form einer anderen Prüfungsbehörde vorgelegt.

Dresden, 2007

Qiang Huang